# FINITE ELEMENT MODELING OF BOND-ZONE BEHAVIOR IN REINFORCED CONCRETE

by

Seungwook Seok

A Dissertation

Submitted to the Faculty of Purdue University

In Partial Fulfillment of the Requirements for the degree of

Doctor of Philosophy
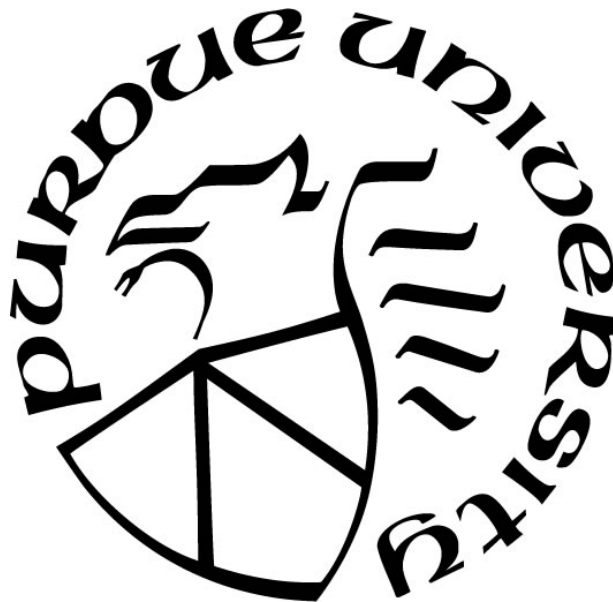
Lyles School of Civil Engineering

West Lafayette, Indiana

December 2019

THE PURDUE UNIVERSITY GRADUATE SCHOOL
STATEMENT OF COMMITTEE APPROVAL

Dr. Ghadir Haikal, Co-Chair

      Lyles School of Civil Engineering

Dr. Julio A. Ramirez, Co-Chair

      Lyles School of Civil Engineering

Dr. Laura N. Lowes

      Civil & Environmental Engineering, University of Washington

Dr. Pablo D. Zavattieri

      Lyles School of Civil Engineering

Approved by:

      Dr. Dulcy M. Abraham

      Head of the Graduate Program

To my wife, Haeree, and my son, Wooree.
Truly thankful for having them in my life.

ACKNOWLEDGMENTS

I would like to express my sincere gratitude to my advisors, Dr. Julio A. Ramirez and Dr. Ghadir Haikal, who have been a constant source of inspiration, guidance, and encouragement during my graduate study at Purdue. I would also like to thank Dr. Laura N. Lowes at University of Washington for serving on my dissertation committee and providing invaluable guidance and assistance for me to complete the study.

TABLE OF CONTENTS

LIST OF TABLES

LIST OF FIGURES

NOMENCLATURE

a_0	aggregate shape factor
a_r	top rib width
A_{max}	maximum aggregate size
A_s	parameter determined from the softening response under uniaxial compression
A_g, B_g	parameters derived from assumptions on the plastic flow in uniaxial tension and compression in the post-peak regime
A_h, B_h, C_h, D_h	parameters calibrated from the strain values at peak stress under uniaxial tension, uniaxial compression, and triaxial compression
b_r	base rib width
B	specimen width
CM, TM	compressive meridian and tensile meridian
d_b	bar diameter
D_f	Ratio of the inelastic lateral strain to the inelastic axial strain
D_{FEA}	displacement at peak load obtained from finite element analysis
D_{Test}	displacement at peak load obtained from test
e	eccentricity in concrete damage-plasticity model (CDPM2)
E	elastic modulus of concrete
$\boldsymbol{E}$	elastic stiffness tensor
E_s	elastic modulus of steel
E_h, F_h	Parameters determined to ensure the smooth transition between two parts of Eq. (3.27)
f_{bc}	concrete biaxial compressive strength
f_c	concrete (uniaxial) compressive strength

f_p	yield function for concrete
f_t	concrete (uniaxial) tensile strength
f_u	steel reinforcement ultimate strength
f_y	steel reinforcement yield strength
g_p	plastic potential function for concrete
G_f	concrete fracture energy
G_{fc}	concrete crushing energy
h_r	rib height
H	specimen height
H_p	artificial hardening modulus
I_1	first invariant of the volumetric stress tensor
J_2	second invariant of the deviatoric stress tensor
J_3	third invariant of the deviatoric stress tensor
K_c	ratio of the second deviatoric stress invariant on the tensile meridian to that on the compressive meridian
L_e	characteristic length of the finite element mesh
$\boldsymbol{m}$	derivative of the plastic potential function with respect to the effective stress tensor
m_g	variable that controls the ratio of volumetric and deviatoric plastic flow
m_0	frictional strength
P_{FEA}	peak load obtained from finite element analysis
P_{Test}	peak load obtained from test
q_{h1}, q_{h2}	variables that control the evolution of the yield function
R_r	relative rib area

R_h	dimensionless parameter that indicates the volumetric stress level
s_r	center-to-center rib spacing
$\bar{\mathbf{s}}$	deviatoric effective stress tensor
$\bar{s}_1, \bar{s}_2, \bar{s}_3$	principal components of deviatoric effective stress tensor $(\bar{s}_1 \geq \bar{s}_2 \geq \bar{s}_3)$
U_1, U_2, U_3	directions in the global coordinates
w_f, w_{f1}	displacement thresholds
w/c	concrete water-cement ratio
x_h	hardening ductility measure
x_s	softening ductility measure
$\hat{x}$	principal component of the tensor
$\langle x \rangle_+$	positive operator, defined as $\langle x \rangle_+ = \max(0, x)$
$\langle x \rangle_-$	negative operator, defined as $\langle x \rangle_- = \min(0, x)$

Greek symbols

α_c	dimensionless parameter that takes the portion of compressive stress with respect to the given effective stress tensor
$\alpha_1, \alpha_2, \alpha_3$	parameters in yield function of concrete damaged-plasticity model
β_c	parameter introduced to provide a smooth transition from pure damage to damage-plasticity softening process
r	function that controls the shape of yield function on the deviatoric plane
$\boldsymbol{\delta}$	Kronecker delta tensor
ε	total strain
$\boldsymbol{\varepsilon}$	total strain tensor
ε_f	strain threshold at which the uniaxial tensile stress is equal to zero

ε_{f1}	strain threshold at which the uniaxial tensile stress is equal to σ_1 shown in Figure 3.5
ε_{fc}	inelastic strain threshold determining the initial inclination of the compressive softening curve
ε_i	inelastic strain
ε_p	plastic strain
$\boldsymbol{\varepsilon}_p$	plastic strain tensor
ε_0	strain corresponding to the concrete uniaxial tensile strength
ε_{20}	residual strain corresponding to the 20% peak stress at descending branch of concrete compressive stress-strain curve
$\dot{\boldsymbol{\varepsilon}}_p$	rate of plastic strain tensor
$\tilde{\varepsilon}$	equivalent strain
$\tilde{\boldsymbol{\varepsilon}}_p$	equivalent plastic strain tensor, $\tilde{\boldsymbol{\varepsilon}}_p = \{\tilde{\varepsilon}_{pt} \quad \tilde{\varepsilon}_{pc}\}^T$
$\tilde{\varepsilon}_{pc}$	equivalent compressive plastic strain
$\tilde{\varepsilon}_{pt}$	equivalent tensile plastic strain
ϵ	eccentricity in concrete damaged-plasticity (CDP) model
$\bar{\theta}$	load angle
$\kappa_{dc}, \kappa_{dc1}, \kappa_{dc2}$	history variables for compression
$\kappa_{dt}, \kappa_{dt1}, \kappa_{dt2}$	history variables for tension
κ_p	hardening variable (cumulative plastic strain)
$\dot{\kappa}_p$	rate of hardening variable
λ	plastic multiplier
$\dot{\lambda}$	rate of plastic multiplier
μ	tangential friction coefficient at the concrete-reinforcement interface
$\bar{\rho}$	deviatoric effective stress

$\boldsymbol{\sigma}$	nominal stress tensor
$\bar{\boldsymbol{\sigma}}$	effective stress tensor
$\bar{\sigma}_c$	effective compressive cohesion stress
$\bar{\boldsymbol{\sigma}}_c$	negative part of the effective stress tensor
$\bar{\boldsymbol{\sigma}}_p$	principal effective stress tensor
$\bar{\sigma}_t$	effective tensile cohesion stress
$\bar{\boldsymbol{\sigma}}_t$	positive part of the effective stress tensor
$\bar{\sigma}_{pt,i}, \bar{\sigma}_{pc,i}$	tensile and compressive stress components of the principal effective stresses, respectively
$\bar{\sigma}_1, \bar{\sigma}_2, \bar{\sigma}_3$	principal components of effective stress ($\bar{\sigma}_1 \geq \bar{\sigma}_2 \geq \bar{\sigma}_3$)
$\bar{\sigma}_V$	volumetric effective stress
$\hat{\bar{\sigma}}_1$	maximum principal component of the effective stress tensor
ψ	dilation angle
ω	damage variable
ω_c	compressive damage variable
ω_t	tensile damage variable

ABSTRACT

Author: Seok, Seungwook. Ph.D.
Institution: Purdue University
Degree Received: December 2019
Title: Finite Element Modeling of Bond-Zone Behavior in Reinforced Concrete
Committee Chair: Ghadir Haikal and Julio A. Ramirez

In reinforced concrete (RC) structures, adequate bond between the reinforcement and concrete is required to achieve a true composite system, in which reinforcing steel carries tensile stress, once concrete cracks, and concrete and reinforcing steel carry compression. Determining bond strength and required development length for shear transfer between concrete and reinforcement is an ongoing research subject in the field of reinforced concrete with advances in the concrete and reinforcement materials requiring continuous experimental efforts. Finite element analysis (FEA) provides opportunities to explore structural behavior of RC structures beyond the limitations of experimental testing. However, there is a paucity of research studies employing FEA to investigate the reinforcement-concrete bond-zone behavior and related failure mechanism. Instead, most FEA-based research associated with RC bond has centered on developing a bond (or interface) constitutive model for use in FEA that, by itself, can characterize bond-zone behavior, typically represented by the bond stress-slip displacement relationship. This class of bond models is useful for simulating the global behavior of RC structures but is limited in its ability to simulate local bond resistance for geometries and material properties that differ substantially from those used to calibrate the model. To fill this gap in research, this study proposes a finite element (FE) modeling approach that can simulate local bond-zone behavior in reinforced concrete. The proposed FE model is developed in a physics-based way such that it represents the detailed geometry of the bond-zone, including ribs on the deformed reinforcement, and force transfer mechanisms at the concrete-reinforcement interface. The explicit representation of the bond-zone enables simulation of the local concrete compression due to bearing of ribs against concrete and subsequent hoop tension in the concrete. This causes bond failure either due to local concrete crushing (leading to reinforcement pullout) or global concrete splitting. Accordingly, special attention is given to the selection and calibration of a concrete model to reproduce robust nonlinear response. The power of the proposed modeling approach is its ability to predict bond failure and damage patterns, based

only on the physical and material properties of the bond area. Thus, the successful implementation and application of this approach enables the use of FEA simulation to support the development of new design specifications for bond zones that include new and improved materials.

CHAPTER 1.   INTRODUCTION

1.1   Motivation

The acceptable performance of a reinforced concrete (RC) structure requires the transfer of forces between concrete and reinforcing steel via bond. Adequate *bond* in regions where bars are anchored or spliced is particularly critical to structural performance. The characterization and prediction of bond-zone behavior are challenging due to the complexity of stress and strain fields in the bond-zone, the development of localized inelasticity, and the dependence of these on a variety of parameters including concrete strength, and reinforcement configuration and coating.

Numerous experimental tests have addressed bond-zone behavior and the factors that affect it (e.g., Abrams, 1913; Azizinamini et al., 1993; Eligehausen et al., 1983; Marques & Jirsa, 1975; Minor & Jirsa, 1975; Ramirez & Russell, 2008; Sperry et al., 2015). Data from these tests supported the development of present-day specifications for design and detailing of bond-zones including tension splices and bars anchorage. Because bond-zone behavior is complex, many individual tests are required to develop and validate design specifications. With the recent advent of ultra-high strength concrete and high-strength steel (Tai, El-Tawil, & Chung, 2016; Wille & Naaman, 2013; Yoo & Yoon, 2015), it is necessary to revisit current specifications for bond-zone, and many new laboratory tests are required to develop and/or validate current design requirements for bond-zone that include these new high-strength materials.

Numerical analysis can provide data to support development of new design specifications at less cost that is required for laboratory testing. Numerical analysis also provides much richer data sets characterizing bond-zone behavior. Using numerical simulation, high-fidelity bond-zone stress, strain, and damage fields are immediately available, while experimental data typically include only global load-displacement response and steel, and possibly concrete, strains at relatively a few locations. The research presented here seeks to develop and validate a numerical modeling approach for RC bond-zones, with the expectation that this modeling approach can be used to supplement experimental testing and provide additional data required to develop advanced design requirements for RC bond-zones, including those comprising high strength concrete and/or steel.

1.2   Experimental Efforts to Understand Bond-Zone Behavior

Reinforcement-concrete bond comprises chemical adhesion, friction, and mechanical interaction (Abrams, 1913; Lutz & Gergely, 1967). Many material properties and geometric design characteristics affect these bond mechanisms, including bar size (i.e. diameter), rib configuration (e.g., height, angle, spacing, etc.), presence of coating on the bar, concrete strength, bar strength, confining pressure provided by transverse reinforcement, and the length of the anchorage or splice zone. Previous experimental research studies by many research groups provide an understanding of bond-zone behavior and the impact of various design parameters on this behavior; those studies that have had the greatest impact on the current understanding of bond-zone behavior are discussed as below.

- Abrams (1913) tested numerous pullout and beam specimens with a wide range of material properties and design configurations. Findings from this study provided a basic understanding of bond-zone response.

- Goto (1971) investigated internal crack initiation and propagation in tension bond-zone by injecting ink into the bond region of pullout specimens. The author observed differences in crack formation and propagation between specimens with smooth and deformed bars as well as between specimens with different bar deformation patterns (lateral ribs, diagonal ribs, and wavy ribs).

- Eligehausen et al. (1983) examined local bond behavior using test specimens that represent beams with bar embedded in RC beam-column joint. Multiple parameters including external confining pressure and concrete compressive strength were considered in this investigation. The study showed that bond strength increases with higher confining pressure but remains constant once confining pressure exceeds a certain level, and bond strength is proportional to the square root of concrete compressive strength.

- Tholen & Darwin (1996) investigated the impact on *bond* of the deformation properties of deformed bars, using pull-out type specimens with and without confinement. The main investigation parameters were bar size, relative rib area (discussed later and quantified by Eq. (1)), and the ratio of rib width to rib spacing. Based on dozens of experimental tests, the authors concluded that bond strength for confined specimens increases with higher bar size and with higher relative rib area. However, the variation in the relative rib area did not affect bond strength for bars anchored in unconfined concrete.

- Zuo & Darwin (2000) tested beam-splice specimens to investigate the bond strengths of uncoated and epoxy-coated bars having a high relative rib area. The researchers confirmed the same observations on the relationship between relative rib area and bond strength in beam-splice specimens as those observed in pull-out specimens in the work of Tholen and Darwin (Tholen & Darwin, 1996).

- Murcia-Delso et al. (2013)conducted pull-out tests of large-diameter (#11 (36 mm), #14 (43 mm), and #18 (57 mm)) bars embedded in well-confined concrete. This study concluded that bond strength tends to increase slightly with bar size and remarkably with concrete compressive strength.

1.3   Numerical Approach to Simulate Bond-Zone Behavior

Despite all the above experimental efforts, there is still an increasing need for study on bond behavior due to the continuing improvement of concrete and reinforcement materials and design configurations (Sperry et al., 2015). Finite element analysis (FEA) can serve as a supportive tool to explore alternative bond configurations without the prohibitive cost of a full-scale experimental study. Furthermore, a validated numerical model can be used to generate rich data sets for bond behavior, with various steel and concrete properties and bond-zone design. Developing a model validated bond-zone model requires careful consideration because of various bond mechanisms observed in experimental investigations, all of which may not be reflected in the model. The level of detail in a FE model varies with the scale of the model. Accordingly, the bond-zone models have been developed at several scales: (1) element-scale, (2) bar-scale, (3) rib-scale, and (4) intermediate-scale. The following is a brief description of each model at different scale:

- In an element-scale model, structural components such as beams and columns are modeled using line elements, and a rotational spring is introduced at the column-foundation or beam-column interface to simulate deformation, and potentially strength loss, associated with slip of reinforcement resulting from loss of bond strength. This modeling approach has been favored because it enables an analysis of the structural component or even entire structure with great efficiency (Berry, Lehman, & Lowes, 2008; Hwang & Lignos, 2017).

- In a bar-scale model, the reinforcing bar is modeled using a truss element and is embedded in a concrete volume modeled using solid elements. For many applications, perfect bond between bar and concrete elements is assumed, due to simplicity and efficiency of this

modeling approach (Hawileh et al., 2009). Alternatively, a bond constitutive model, representing the local bond stress versus slip response, is introduced. This bond model is typically defined using experimental data (Eligehausen et al., 1983; Lowes, Moehle, & Govindjee, 2004; Murcia-Delso & Shing, 2014, 2015).

- A rib-scale model treats both the bond-zone concrete and reinforcing bar as continuums, represented with solid elements. This highly refined model enables explicit modeling of the ribs of the bar and concrete at the concrete-bar interface. A contact model is used to account for shear and normal stress transfer at the interface. Rib-scale model is computationally intensive due to a significant number of elements. Nevertheless, it has an advantage in that bond-zone response such as shear and radial stress developed in the course of debonding and interlocking of ribs (i.e., dowel action) can be directly reproduced as the analysis result (Lagier, Massicotte, & Charron, 2016; Li, 2010; Salem & Maekawa, 2004).

- In some cases, both concrete and bar are modeled with solid elements and a cohesive element is introduced at the concrete-steel interface. The influence of the deformation of a bar such as ribs is implicitly considered through the interface law (or interface model) defined at the cohesive element. Thereby, radial stress by mechanical interlocking can be simulated. This model is called intermediate-scale model. Like the bar-scale model, it is required to use a phenomenological interface model based on test data to account for bond effect (Cox & Herrmann, 1998; Michou et al., 2015).

In summary, element-scale and bar-scale models are considered appropriate for simulating global behavior of RC structures, where local bond response is not significant to the global response. By contrast, rib-scale and intermediate-scale models have the potential to reproduce local bond response. The advantage of the rib-scale model is that it does not require an "empirically-derived" bond (or interface) constitutive model to represent bond response such as radial bond stress and slip, which plays a critical role in producing local crack or crushing of concrete material. It must be noted that those bond models are limited to the range of material and geometrical properties for which they were developed (e.g., concrete strength, reinforcement configuration and coating, and confinement level). Thus, for the goal of reproducing local bond response for a wide range of bond configurations by means of FE simulation, rib-scale modeling seems a more appropriate approach (Lagier et al., 2016). Therefore, this research study utilizes a

rib-scale modeling approach to benefit from its feature that can mitigate the reliance on a phenomenological bond model.

1.4   Research Objectives and Scopes

The research project herein aims to develop a physics-based rib-scale FE model for RC bond-zone behavior simulation, without resorting to a phenomenological bond model, that has the capability to (1) simulate global applied load-slip displacement response, (2) reproduce crack initiation and growth pattern, and (3) subsequently capture different modes of failure (e.g., bar pullout failure and concrete splitting failure). To achieve the goals, the geometry of the ribs on a deformed bar and the surrounding concrete at the vicinity of the interface are explicitly represented, as in other studies (Lagier et al., 2016; Li, 2010; Salem & Maekawa, 2004). The model is defined using only experimentally-obtained material properties and geometrical parameters. To account for *bond* between concrete and steel, a contact formulation that represents mechanical characteristics of such bond, is used. The applicability of the proposed FE modeling approach is verified using available test data (Metelli & Plizzari, 2014; Murcia-Delso et al., 2013; Ramirez & Russell, 2008).

The research study will examine aspects of the model that are critical to predicting the bond response. Two different types of test specimens are employed to develop and validate the model: (1) pullout test specimens composed of a single straight reinforcement embedded in concrete block and (2) RC beam specimens with bar splices loaded in tension due to beam bending moment. These types of specimens were selected to consider different bond behavior. It is noted that for both specimen types, quasi-static monotonic loading under displacement control was employed. The successful completion of this study provides the following research contributions:

- modeling strategy to reproduce bond behavior, specialized for different characteristics of bond-zone behavior (characterized by either pullout of single straight bar or bar splices in tension by bending moment loading);
- key material and geometrical parameters that have a significant impact on bond behavior for various specimen configurations;
- values (or ranges of values) for key model parameters that result in an accurate prediction of bond response. Those parameters include concrete crushing and fracture energy, concrete tensile yield strength, and contact properties for shear and normal behavior;

- providing much richer data sets characterizing bond-zone behavior, in comparison to experimental testing.

1.5   Dissertation Organization

This dissertation is presented in six chapters. CHAPTER 1 outlines the research background and problem statement, followed by the research objectives and scope. In CHAPTER 2, a so-called rib-scale FE modeling approach to RC bond-zone behavior is proposed and is discussed with the modeling and analysis details included: geometrical configuration, FE discretization, material and contact models, loading application strategy, and solution scheme. CHAPTER 3 discusses the concrete models from a constitutive modeling point of view with an emphasis on its proper use for the problem at hand. CHAPTER 4 presents the first application of the proposed modeling approach to the simulation of pullout of reinforcement embedded in a concrete block. The second application to simulating reinforcement splice failure in concrete beam structure is given in CHAPTER 5. Lastly, CHAPTER 6 summarizes the key findings and contributions of this study. It also discusses the limitations of the proposed modeling approach and related future work.

CHAPTER 2.   RIB-SCALE FINITE ELEMENT MODELING APPROACH TO RC BOND-ZONE BEHAVIOR

2.1   Introduction

Unlike the typical bar-scale modeling strategy widely adopted in structural FEA, where the reinforcement and concrete are modeled, respectively, with truss (or line) and solid elements and a bond constitutive model is applied between them (often, perfect bond model is preferred) (Eligehausen et al., 1983; Lowes et al., 2004; Murcia-Delso & Shing, 2014, 2015), the rib-scale model represents both materials with solid elements and employs a contact model for the concrete-reinforcement interface, intended to capture the physical interaction (e.g., dowel action) between two parts under loading. This modeling strategy, so-called rib-scale FE modeling approach, has been initiated by the fundamental question as to if bond behavior can be reproduced as a result of FE simulation without the use of an "empirically-derived" bond constitutive model (Lagier et al., 2016; Seok et al., 2018). When it comes to simulating bond behavior in this study, a major reason for not relying on an empirical bond constitutive model is because such model is an approximated representation designed for structure- (or member-) level analysis. Particularly, many available bond models have the limitation in reproducing robust radial stress development induced by the locking and consequent dowel action due to the presence of ribs on a deformed reinforcement (Eligehausen et al., 1983; Murcia-Delso & Shing, 2014). It must be mentioned that such mechanism is the key to generate the consequent hardening and softening response of the surrounded concrete material, ultimately causing bond failure. In this Chapter, general information about the rib-scale FE modeling approach to simulating bond-zone behavior will be discussed, including geometrical configuration, material models, and contact models. Afterward, quasi-static loading control and explicit solver scheme will be discussed. Throughout this study, ABAQUS FE software package will be used for model development.

2.2   Geometrical Configuration

Figure 2.1 shows the geometric configuration of the bond-zone including the bar, bar ribs, and surrounding concrete. The FE model incorporates this, with the topology at the reinforcement-concrete interface defined by the relative rib area (R_r). The R_r is defined as the ratio of the rib area

projected on to the plane normal to the bar axis with respect to the product of the nominal bar perimeter and center-to-center rib spacing (Darwin & Graham, 1993) and can be expressed as below.

$$R_r = \frac{\frac{\pi}{4}[(d_b + 2h_r)^2 - d_b^2]}{\pi d_b s_r} = \frac{(d_b + 2h_r)^2 - d_b^2}{4d_b s_r} \tag{2.1}$$

where d_b is the (nominal) bar diameter; s_r is the center-to-center rib spacing; and h_r is the rib height.

Reflecting the actual R_r in the model is very important. Research by Metelli & Plizzari (2014) showed that variation in R_r can result in a variation in bond strength of as much as 40% in pullout tests for specimens without confining reinforcement. Similarly, Tholen & Darwin (1996) observed that bond strength increases with increasing R_r for beam-end and splice tests confined with transverse bars. In the case when actual rib geometry information is not available, the empirical formulas for rib geometry depicted in Figure 2.1(a) are defined such that $a_r = 0.1d_b$, $b_r = 0.2d_b$, $h_r = 0.05d_b$, and $s_r = 0.5d_b$, which result in the R_r of 0.1. Currently used deformed reinforcing bars typically have R_r values ranging from 0.05 to 0.20 (Seok et al., 2018).

To facilitate the model creation, a reinforcement model is created, such that the ribs are shaped as a series of parallel rings oriented perpendicular to the bar axis, as shown in Figure 2.1(b). Here, reinforcement is meshed with 3D continuum solid elements.

(a)   (b)
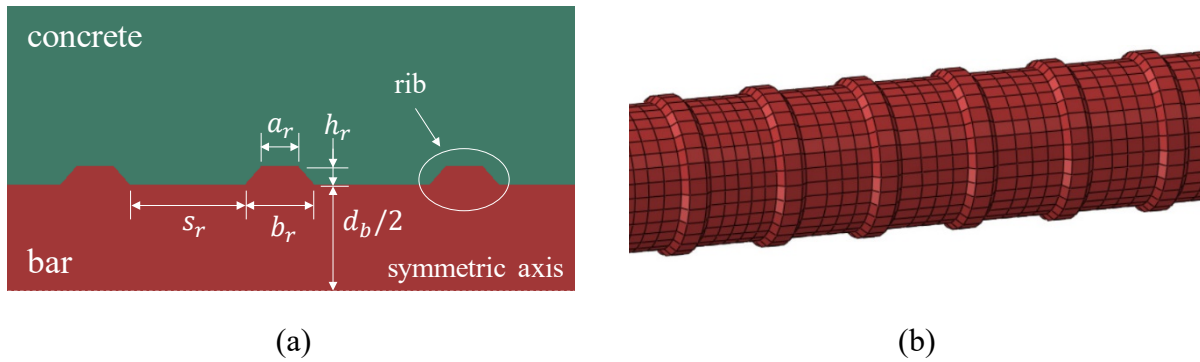
Figure 2.1 Configuration of the bond-zone showing the reinforcement and surrounding concrete: (a) section view of reinforcement and adjacent concrete (b) 3D view of reinforcement

2.3   Material Models

In defining material models for concrete and steel reinforcement, more attention needs to be given to the concrete model than the steel model, because in almost case, bond failure arises from the concrete failure involving crushing, cracking, or both. Steel reinforcement typically remains in an elastic or initial yielding stage at the ultimate loading, which is quite predictable and straightforward behavior from a material modeling point of view. Hence, it is very important to employ the concrete constitutive model capable of reproducing robust hardening and softening response under different multiaxial stress states, validated by the experimental data. Details about the choice of a proper concrete model will be discussed in CHAPTER 3. On the other hand, the steel model for reinforcement can be represented using a set of stress-strain data, which in general, is based on the measured data. If the measured data were not available, there are many models developed for this purpose (e.g., Raynor et al. (2002) and Hoehler & Stanton (2006)).

2.4   Contact Model

At the reinforcement-concrete interface, it is required to define a contact model to simulate force transfer across the interface. Most FE software (ABAQUS, ANSYS, LS-DYNA) provides two contact models: (1) node-to-surface contact model, in which contact conditions are enforced such that each node on one side of contact interface interacts (called "slave" nodes) with a point of projection on the surface on the opposite side of the contact interface (called "master" surface), and (2) surface-to-surface contact model, in which contact conditions are enforced in an average sense over regions of the "master" and "slave" surfaces (Simulia, 2014; Wriggers & Zavarise, 2004). Thus, the node-to-surface contact model is recommended for use when a surface is in contact with a point, such as a sharp object like a pin or bullet impacting a plate or membrane. The surface-to-surface contact model is most appropriate for use in modeling contact between the surfaces of two bodies that are moving relative to each other. Given the fact that pullout behavior of reinforcement against the surrounding concrete acts like the latter case, the surface-to-surface contact model is most appropriate and was used for this study, as employed in other studies (Lagier et al., 2016; Seok et al., 2018).

The surface-to-surface contact formulation in ABAQUS is defined with appropriate properties for the tangential, normal, and cohesive behaviors. For tangential behavior, the

Coulomb's law of friction is used, with an appropriate tangential friction coefficient defined to reflect the actual roughness between the concrete and steel materials. For example, Idun & Darwin (1999) have found the friction coefficient of about 0.5 between steel reinforcement and concrete. The normal behavior is associated with the pressure-overclosure relation in the normal direction of the interface and it is defined using the *hard* contact, which enforces infinite stiffness for overclosure at locations where two surfaces are in contact and pressed against each other. No penetration is allowed with this *hard* contact, while separation is allowed after contact. Chemical adhesion generated in the curing process is related with the cohesive behavior, which can be ignored in case of deformed reinforcement, as it has been experimentally and numerically observed that adhesion is only initiated before slip and accounts for an inconsequential part of bond resistance (Abrams, 1913; Lagier et al., 2016; Salem & Maekawa, 2004; Seok et al., 2018).

2.5   Quasi-Static Analysis

All the experimental test programs to be simulated were conducted under quasi-static conditions. When it comes to the loading application in the FE model, velocity-, rather than displacement-, controlled loading is used to help maintain quasi-static conditions. When displacement-controlled loading is used, it is observed that even very small increments in displacement causes the acceleration to fluctuate drastically with time, resulting in periods of high kinetic energy, and thus dynamic response, during the analysis history. The use of velocity-controlled loading enables stable acceleration and facilitates maintenance of the quasi-static loading employed in the laboratory. It must be noted that kinetic energy must remain below 1% of the internal energy over time when using a velocity loading control, in order to minimize dynamic impact on the response.

2.6   Explicit Solution Scheme

Force transfer by bond is a complex phenomenon resulting in significant nonlinear material response at the concrete-steel interface. Compressive crushing and tensile crack initiation and propagation in the concrete are typical hallmarks of such nonlinearity. Indeed, experimental data show that nonlinear response and ultimate failure of the test specimens were mainly due to large strains and deformations that developed around the interface. Simulation of this type of response using Implicit solution algorithms is often impossible due to convergence problems (Simulia,

2014). Thus, an Explicit Dynamic solution procedure is chosen throughout this study. This solution algorithm employs an explicit central-difference time integration rule with a small step size to integrate the equations of motion for the body and does not require iteration to achieve convergence at each step in the load history. It has been shown to be computationally efficient for the analysis of reinforced concrete components exhibiting large quasi-static nonlinear problems (Genikomsou & Polak, 2015).

2.7   Conclusions

General information about the rib-scale FE modeling approach for RC bond-zone behavior simulation is discussed. The ABAQUS software is used to accomplish the model development and FE analysis. The ABAQUS has the capabilities of simulating large deformations and contact simulations and is relatively well equipped with automatic meshing functions and stable solution algorithms. In the model, high-resolution mesh is applied in the vicinity of the reinforcement-concrete interface to capture the actual geometry of ribs on a deformed bar. The empirical formulas for the detailed rib geometries, such as center-to-center rib spacing and rib height, are proposed in cases where no information regarding the actual reinforcement deformation exists. It is very important to employ a concrete constitutive model capable of reproducing robust hardening and softening response under different multiaxial stress states, as RC bond failure mainly arises from concrete failure accompanying cracking and crushing. Modeling the steel reinforcement is relatively easier and can be achieved using the measured stress-strain data. At the interface, a surface-to-surface contact model that represents mechanical characteristics of bond is introduced to predict bond response by enforcing proper tangential and normal, and cohesive contact interactions without employing a bond constitutive model. This approach can mitigate the reliance on bond models which limited to particular material and structural conditions. When it comes to the loading application, quasi-static loading condition is achieved by velocity-loading control scheme, which is observed to enable stable acceleration over analysis time. Kinematic energy must remain below 1% of the internal energy over time, in order for the analysis not to be considered as dynamic analysis.

CHAPTER 3.   CONCRETE MATERIAL MODEL

3.1   Introduction

Many concrete constitutive models have been developed for simulating nonlinear response due to cracking and crushing mechanisms. One very popular framework for these concrete constitutive models is the combination of plasticity and damage mechanics theories, which is referred to as damage-plasticity model (Grassl et al., 2013). This class of concrete constitutive models is preferred for general applications as it enables simulation of both tensile and compressive failures of the concrete; examples include Grassl (2008), Grassl & Jirásek (2006), Jason et al. (2006), Ju (1989), Lee & Fenves (1998), Nguyen & Houlsby (2008), Nguyen & Korsunsky (2008), Valentini & Hofstetter (2013), and Voyiadjis et al. (2008). Many commercial FE software programs provide a damage-plasticity model(s) for concrete material by default, with formulations varying for each FE software.

As discussed previously for rib-scale simulation of bond-zone behavior, nonlinearity is due primarily to concrete crushing and cracking. Thus, evaluation of existing concrete constitutive models is a necessary first step in the research process. In the following sections, two different concrete damage-plasticity models will be discussed: (1) concrete damaged-plasticity (CDP) model (Simulia, 2014), which is included in ABAQUS and (2) concrete damage-plasticity model (CDPM2) (Grassl et al., 2013), which is implemented as a user-subroutine material *VUMAT* in ABAUQS for use by the author. The first model is chosen for discussion because it is one of the most commonly used concrete damage-plasticity models in the literature. The second model is one of the state-of-the-art concrete models in the class of damage-plasticity models, which has shown its outstanding capability of simulating nonlinear response under static/dynamic multiaxial stress states. For this reason, CDPM2 is chosen among many existing models for this study.

3.2   Concrete Damaged-Plasticity (CDP) Model in ABAQUS

The CDP model was originally proposed by Lubliner et al. (1989) and then improved by Lee & Fenves (1998). The model was implemented in the FE software platform ABAQUS (Simulia, 2014). Due to the model's reasonable performance and easy accessibility within such a popular software tool, a considerable number of FE analyses for concrete structures have been performed

using the CDP model. The following sections present the components that comprise the CDP constitutive model. These include the elastic stress-strain relationship, yield surface, plastic flow potential, and hardening/softening rule. Note that in all mathematical expressions followed, the tension is defined to be positive.

3.2.1 Stress-Strain Relationship

The CDP model assumes that the two failure mechanisms of the concrete material are tensile cracking and compressive crushing, which are mathematically considered with corresponding damage variables in the model's stress-strain relationship as follows.

$$\boldsymbol{\sigma} = (1 - \omega_t)(1 - \omega_c)\bar{\boldsymbol{\sigma}} \tag{3.1}$$

$$\bar{\boldsymbol{\sigma}} = \boldsymbol{E}{:}\left(\boldsymbol{\varepsilon} - \boldsymbol{\varepsilon}_p\right) \tag{3.2}$$

where $\boldsymbol{\sigma}$ is the nominal stress tensor; ω_t and ω_c are the tensile and compressive scalar damage variables, respectively, ranging from 0 (undamaged) to 1 (fully damaged); $\bar{\boldsymbol{\sigma}}$ is the effective stress tensor; $\boldsymbol{E}$ is the elastic stiffness tensor; $\boldsymbol{\varepsilon}$ is the total strain tensor; $\boldsymbol{\varepsilon}_p$ is the plastic strain tensor.

3.2.2 Stress in Cylindrical Coordinate System

For easy formulation, the 3D stress states are defined in the cylindrical coordinates (Haigh-Westergaard coordinates). The transformation of stress components in Rectangular Cartesian coordinates into those in cylindrical coordinates is mathematically straightforward using stress invariants. Given the effective stress tensor $\bar{\boldsymbol{\sigma}}$, the first invariant of the volumetric effective stress tensor is

$$I_1 = \bar{\boldsymbol{\sigma}}{:}\boldsymbol{\delta} \tag{3.3}$$

where $\boldsymbol{\delta}\ (= \delta_{ij})$ is the Kronecker delta and thus, is equal to 3x3 identity tensor.

The second and third invariants of the deviatoric effective stress tensor, $\bar{\boldsymbol{s}}$, are

$$J_2 = \frac{1}{2}\bar{\boldsymbol{s}}{:}\bar{\boldsymbol{s}} \tag{3.4}$$

$$J_3 = \frac{1}{3}\bar{\boldsymbol{s}}^3{:}\boldsymbol{\delta} \tag{3.5}$$

$$\text{where}\ \ \bar{\boldsymbol{s}} = \bar{\boldsymbol{\sigma}} - \boldsymbol{\delta}I_1/3 \tag{3.6}$$

Now, in cylindrical coordinates, stress can be expressed with the three orthogonal components, which are determined as volumetric effective stress ($\bar{\sigma}_V$), norm of the deviatoric

effective stress ($\bar{\rho}$), and load angle ($\bar{\theta}$) in this study. All these components are defined using the stress invariants as follows.

The volumetric effective stress is

$$\bar{\sigma}_V = \frac{I_1}{3} \tag{3.7}$$

The norm of the deviatoric effective stress is

$$\bar{\rho} = \sqrt{2J_2} \tag{3.8}$$

The load angle is

$$\bar{\theta} = \frac{1}{3}\cos^{-1}\left(\frac{3\sqrt{3}}{2}\frac{J_3}{J_2^{3/2}}\right) \tag{3.9}$$

3.2.3 Yield Function and Hardening/Softening

The plastic strain arises only when the material exceeds its elastic limit stress. In a 1D stress state such as uniaxial compression, for example, the concrete material has the elastic limit stress of 30% of concrete compressive strength f_c. However, for a 3D stress state such as triaxial compression with nonuniform lateral confining pressure, a general limit state criterion needs to be defined in the 3D stress space. This criterion is called the yield surface, which is used to identify the onset of plastic flow. The yield surface increases/decreases according to the material's hardening/softening rule. It is understood that for the isotropic and homogeneous constitutive model for concrete, the yield surface exhibits three-folded symmetry about the volumetric stress (or hydrostatic pressure) axis on the deviatoric plane view (e.g., Figure 3.1).
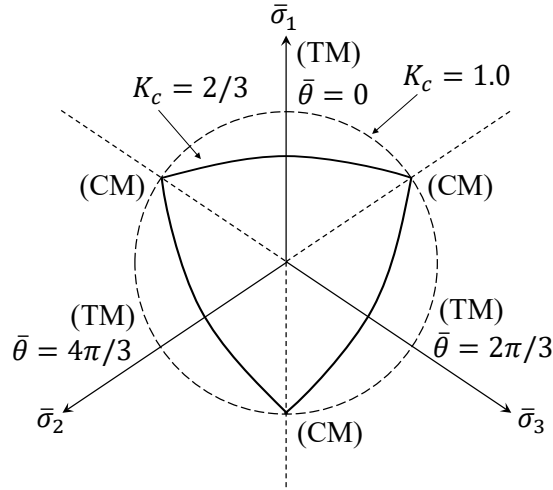
Figure 3.1 CDP model's yield surface on the deviatoric plane, where TM and CM represent the tensile meridian and compressive meridian.

The yield function, a mathematical expression for the yield surface, plays a role in providing the criterion for judging the current material state as being either elastic or plastic. The CDP model's yield function takes the following form and its corresponding yield surface on the deviatoric plane is shown in Figure 3.1.

$$f_p(\bar{\sigma}_V, \bar{\rho}, \tilde{\pmb{\varepsilon}}_p) = \frac{1}{1 - \alpha_1}\left(\frac{\sqrt{3}}{\sqrt{2}}\bar{\rho} + 3\alpha_1\bar{\sigma}_V + \alpha_2(\tilde{\pmb{\varepsilon}}_p)\langle\hat{\bar{\sigma}}_1\rangle_+ - \alpha_3\langle-\hat{\bar{\sigma}}_1\rangle_+\right) - \bar{\sigma}_c(\tilde{\varepsilon}_{pc}) \quad (3.10)$$

where $\bar{\sigma}_c$ is the effective compressive cohesion stress, used as the hardening/softening law; $\tilde{\varepsilon}_{pc}$ is the equivalent compressive plastic strain, used as the hardening/softening variable. The hat mark ($\hat{x}$) indicates the principal component of the tensor, and thus $\hat{\bar{\sigma}}_1$ is the maximum principal component of the effective stress tensor. $\langle x\rangle_+$ is the positive operator, defined as $\langle x\rangle_+ = \max(0, x)$.

The parameters α_1, α_2, and α_3 are the dimensionless parameters, defined in Eqs. (3.11)-(3.13).

$$\alpha_1 = \frac{f_{bc}/f_c - 1}{2f_{bc}/f_c - 1} \quad (3.11)$$

$$\alpha_2 = \frac{\bar{\sigma}_c(\tilde{\varepsilon}_{pc})}{\bar{\sigma}_t(\tilde{\varepsilon}_{pt})}(1 - \alpha) + (1 + \alpha) \quad (3.12)$$

$$\alpha_3 = \frac{3(1 - K_c)}{2K_c - 1} \quad (3.13)$$

In these equations, f_{bc} and f_c are the concrete biaxial and uniaxial compressive strengths, respectively. In general, f_{bc}/f_c is taken as 1.16. $\bar{\sigma}_t$ is the effective tensile cohesion stress, used as the hardening/softening law. $\tilde{\varepsilon}_{pt}$ is the equivalent tensile plastic strain, used as the hardening/softening variable. K_c is the ratio of the second deviatoric stress invariant ($\bar{\rho}$) on the tensile meridian (TM) to that on the compressive meridian (CM), which determines the degree of the convex shape of the yield surface on the deviatoric plane (Figure 3.1). K_c must meet the condition, $0.5 < K_c \leq 1.0$, and the default value is 2/3.

The yield surface evolves as the two hardening/softening variables $\tilde{\varepsilon}_{pc}$ and $\tilde{\varepsilon}_{pt}$ are accumulated under loading leading to the growth of plastic flow, until it reaches its maximum extent, called failure surface. Once the failure surface is reached, the concrete material starts to lose its load-carrying capacity and thus, the yield surface shrinks, up to a limit of its ultimate residual strength, called residual surface. The first phase, where the yield surface growth from the initial yield surface to the failure surface is referred to as the material hardening process, and the second phase from the failure surface to the residual surface as the material softening process.

3.2.4 Plastic Flow

Once the concrete material exceeds its limit state defined by Eq. (3.10), plastic flow develops, which is defined in the rate form as

$$\dot{\varepsilon}_p = \lambda \boldsymbol{m} = \lambda \frac{\partial g_p}{\partial \bar{\boldsymbol{\sigma}}} \tag{3.14}$$

where λ is the dimensionless plastic multiplier that determines the magnitude of the plastic strain, and g_p is the plastic potential function that controls the dilatancy of the material.

The CDP model assumes a non-associative flow rule ($g_p \neq f_p$) and adopts the Drucker-Prager hyperbolic function as the plastic potential function, specified as

$$g_p(\bar{\sigma}_V, \bar{\rho}) = \sqrt{(\epsilon f_t \tan \psi)^2 + \frac{3}{2}\bar{\rho}^2} + \bar{\sigma}_V \tan \psi \tag{3.15}$$

where ψ is the dilation angle representing the slope of g_p measured on the meridian plane; f_t is the concrete uniaxial tensile strength; ϵ is the eccentricity that defines the rate at which the function approaches the asymptote and the default value is 0.1. The parameter ϵ has been introduced to avoid the singular point at the apex of the flow potential function (Simulia, 2014).

3.3 Concrete Damage-Plasticity Model (CDPM2)

Despite continued efforts through the years to advance damage-plasticity models for concrete, models still fail to provide accurate simulation of response for concrete subjected to different multiaxial loading scenarios (Grassl & Jirásek, 2006). Recently, a concrete plasticity model formulated in the effective stress space combined with a strain-based damage law was proposed to further advance concrete constitutive modeling, which is named concrete damage-plasticity model (CDPM1) (Grassl & Jirásek, 2006). This model was limited to monotonic loading applications, and thus was further improved in its extended version, concrete damage-plasticity model (CDPM2), to apply to cyclic loading and to ensure the mesh-independent softening response (Grassl et al., 2013). Hereafter, a brief summary of the CDPM2 is presented. For details, the reader is referred to the work of Grassl et al. (2013).

3.3.1 Stress-Strain Relationship

The stress-strain relationship used in CDPM2 decouples the positive (tensile) and negative (compressive) damage, unlike CDP model presented in Eq. (3.1), and is given by Eq. (3.16).

$$\boldsymbol{\sigma} = (1 - \omega_t)\overline{\boldsymbol{\sigma}}_t + (1 - \omega_c)\overline{\boldsymbol{\sigma}}_c \tag{3.16}$$

where $\overline{\boldsymbol{\sigma}}_t$ and $\overline{\boldsymbol{\sigma}}_c$ are the positive and negative parts of the effective stress tensor $\overline{\boldsymbol{\sigma}}_c$, respectively. They are defined using the principle effective stress $\overline{\boldsymbol{\sigma}}_p$ as $\overline{\boldsymbol{\sigma}}_t = \langle \overline{\boldsymbol{\sigma}}_p \rangle_+$ and $\overline{\boldsymbol{\sigma}}_c = \langle \overline{\boldsymbol{\sigma}}_p \rangle_-$, where $\langle x \rangle_+ = \max(0, x)$ and $\langle x \rangle_- = \min(0, x)$.

3.3.2 Yield Function, Plastic Flow, and Hardening

The CDPM2's yield function is proposed based on the triaxial failure criterion for concrete proposed by Menetrey & Willam (1995) as

$$f_p\left(\bar{\sigma}_V, \bar{\rho}, \bar{\theta}, \kappa_p\right) = \left\{[1 - q_{h1}]\left(\frac{\bar{\rho}}{\sqrt{6}f_c} + \frac{\bar{\sigma}_V}{f_c}\right)^2 + \frac{\sqrt{3}}{\sqrt{2}}\frac{\bar{\rho}}{f_c}\right\}^2 + m_0 q_{h1}^2 q_{h2}\left(\frac{\bar{\rho}}{\sqrt{6}f_c}r + \frac{\bar{\sigma}_V}{f_c}\right) - q_{h1}^2 q_{h2}^2 \tag{3.17}$$

$$\text{where } q_{h1} = \begin{cases} q_{h0} + (1 - q_{h0})\left(\kappa_p^3 - 3\kappa_p^2 + 3\kappa_p\right) - H_p\left(\kappa_p^3 - 3\kappa_p^2 + 2\kappa_p\right) & \text{if } \kappa_p < 1 \\ 1 & \text{if } \kappa_p \geq 1 \end{cases} \tag{3.18}$$

$$q_{h2} = \begin{cases} 1 & \text{if } \kappa_p < 1 \\ 1 + H_p\left(\kappa_p - 1\right) & \text{if } \kappa_p \geq 1 \end{cases} \tag{3.19}$$

$$r = \frac{4(1 - e^2)(\cos \bar{\theta})^2 + (2e - 1)^2}{2(1 - e^2) \cos \bar{\theta} + (2e - 1)\sqrt{4(1 - e^2)(\cos \bar{\theta})^2 + 5e^2 - 4e}} \tag{3.20}$$

$$m_0 = \frac{3(f_c^2 - f_t^2)}{f_c f_t} \frac{e}{e + 1} \tag{3.21}$$

In these equations, e is the eccentricity parameter and is taken as 0.52 for $f_{bc}/f_c = 1.16$. The function r controls the shape of the yield function on the deviatoric plane (Figure 3.2). The parameter m_0 is the dimensionless frictional strength given by Menetrey & Willam (1995).

The yield surface evolves according to the values of the dimensionless variables q_{h1} and q_{h2}, that are dependent on the hardening variable (or cumulative plastic strain) κ_p (Figure 3.2 and Figure 3.3). The variables q_{h1} and q_{h2} change with respect to the accumulated κ_p, as graphically illustrated in Figure 3.4, where H_p is the artificial hardening modulus that helps to introduce the equivalent strain $\tilde{\varepsilon}$ during the material softening (will be discussed later). As seen in Figure 3.3, the evolving yield surface keeps a closed-shape in the hardening process until it gets to the open-shaped failure surface where $q_{h1} = q_{h2} = 1$. This failure surface is identical to that of Menetrey & Willam (1995).

The CDMP2 follows a non-associative plastic flow. The plastic potential function is defined as

$$g_p(\bar{\sigma}_V, \bar{\rho}, \kappa_p) = \left\{ [1 - q_{h1}] \left(\frac{\bar{\rho}}{\sqrt{6}f_c} + \frac{\bar{\sigma}_V}{f_c} \right)^2 + \frac{\sqrt{3}}{\sqrt{2}} \frac{\bar{\rho}}{f_c} \right\}^2 + q_{h1}^2 \left(\frac{m_0 \bar{\rho}}{\sqrt{6}f_c} + \frac{m_g}{f_c} \right) \tag{3.22}$$

$$\text{where} \quad m_g = A_g B_g f_c \exp \left(\frac{\bar{\sigma}_V - q_{h2} f_t/3}{B_g f_c} \right) \tag{3.23}$$

$$A_g = 3 q_{h2} f_t/f_c + m_0/2 \tag{3.24}$$

$$B_g = \frac{(q_{h2}/3)(1 + f_t/f_c)}{\ln A_g - \ln(2D_f - 1) - \ln(3q_{h2} + m_0/2) + \ln(D_f + 1)} \tag{3.25}$$

In the above equations, m_g is the variable that controls the ratio of volumetric to deviatoric plastic flow. A_g and B_g are the parameters derived from assumptions on the plastic flow in uniaxial tension and compression, respectively, in the post-peak regime where $q_{h1} = 1$. The derivation of these parameters is found in Grassl & Jirásek (2006). The parameter D_f is the ratio of the inelastic lateral strain to the inelastic axial strain and is set to 0.85, per Grassl et al. (2013).

During plastic flow, the hardening variable κ_p is accumulated according to the evolution law defined below.

$$\dot{\kappa}_p = \frac{\|\dot{\varepsilon}_p\|}{x_h}(\cos\bar{\theta})^2 = \frac{\dot{\lambda}\|\boldsymbol{m}\|}{x_h}(\cos\bar{\theta})^2 \tag{3.26}$$

$$\text{where} \quad x_h = \begin{cases} A_h - (A_h - B_h)\exp(-R_h/C_h) & \text{if } R_h \geq 0 \\ E_h\exp(R_h/F_h) + D_h & \text{if } R_h < 0 \end{cases} \tag{3.27}$$

$$R_h = -\bar{\sigma}_V/f_c - 1/3 \tag{3.28}$$

Here, the parameters A_h, B_h, C_h, and D_h are calibrated from the strain values at peak stress under uniaxial tension, uniaxial compression, and triaxial compression, as detailed in Grassl & Jirásek (2006). E_h and F_h are determined to ensure the smooth transition between two parts of Eq. (3.27) as $E_h = B_h - D_h$ and $F_h = [(B_h - D_h)C_h]/(A_h - B_h)$. For the rate form of κ_p in Eq. (3.26), the hardening ductility measure x_h, which is dependent on R_h, is designed to provide a more ductile response under compression than under tension. This helps to achieve realistic dilation response of concrete, particularly under high confinement conditions.
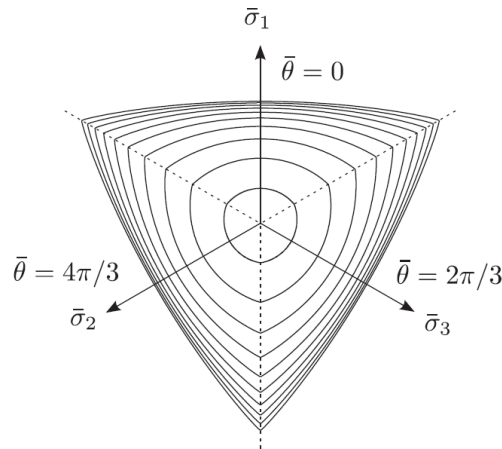
Figure 3.2 Evolution of the CDPM2's yield surface on the deviatoric section during hardening for a constant volumetric stress $\sigma_V/f_c = -3$ (Grassl et al., 2013)
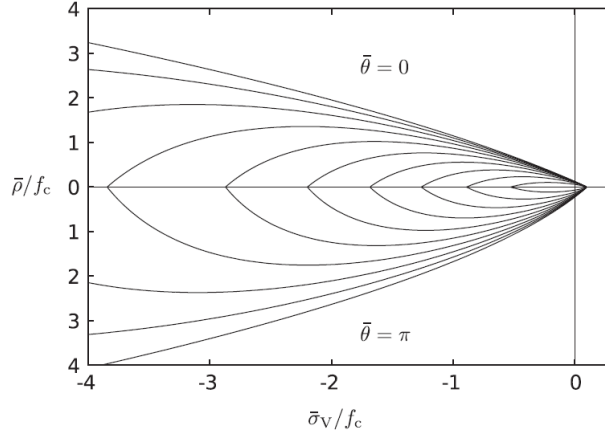
Figure 3.3 Evolution of the CDPM2's yield surface on the TM and CM sections during hardening (Grassl et al., 2013)
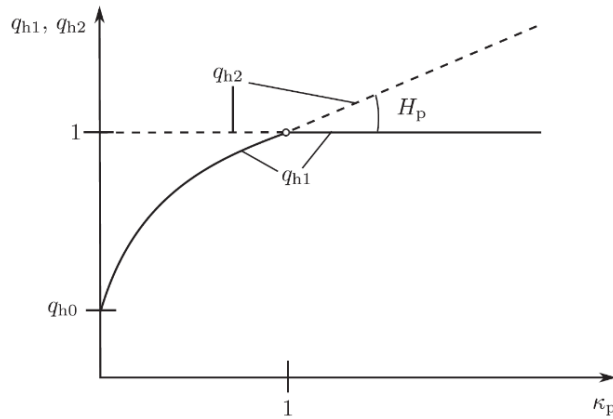
Figure 3.4 Graphical representation of q_{h1} and q_{h2} according to κ_p (Grassl et al., 2013)

3.3.3 Damage (Softening)

In the CDPM2, softening response of the concrete is formulated based on the effective stress. According to Eq. (3.17), a value of q_{h2} greater than one in the post-peak regime (where $q_{h1} = 1$ and $q_{h2} > 1$) leads to a continuous expansion of the yield surface beyond the failure surface (where $q_{h1} = q_{h2} = 1$), resulting in an increase in effective stress $\bar{\sigma}$. Then, $\bar{\sigma}$ is reduced (scaled down) in the nominal stress σ (i.e., softened stress) by the tensile damage ω_t, compressive damage ω_c, or both, developed during the post-peak phase, as formulated in Eq. (3.16). For uniaxial tension, damage is initiated when an equivalent strain exceeds the threshold $\varepsilon_0 = f_t/E$. Now, for multiaxial stress state, a more general expression for the "scalar-valued" equivalent strain $\tilde{\varepsilon}$ needs to be derived, on which basis those scalar damage parameters, ω_t and ω_c, can be predicted. To derive

$\tilde{\varepsilon}$, the variable q_{h2} in the yield function (Eq. (3.17)) is used: Setting $q_{h1} = 1$ and $q_{h2} = \tilde{\varepsilon}/\varepsilon_0$, where $\varepsilon_0 = f_t/E$, into the yield function and solving for $\tilde{\varepsilon}$ gives

$$\tilde{\varepsilon} = \frac{\varepsilon_0 m_0}{2}\left[\left(\frac{\bar{\rho}}{\sqrt{6}f_c}r + \frac{\bar{\sigma}_V}{f_c}\right) + \sqrt{\left(\frac{\bar{\rho}}{\sqrt{6}f_c}r + \frac{\bar{\sigma}_V}{f_c}\right)^2 + \frac{3\varepsilon_0^2\bar{\rho}^2}{2f_c^2}}\right] \tag{3.29}$$

For instance, the effective stress states of the concrete uniaxial tensile strength in the multiaxial stress space are defined as $\bar{\sigma}_1 = f_t$ and $\bar{\sigma}_2 = \bar{\sigma}_3 = 0$. It follows that $\bar{\sigma}_V = f_t/3$, $\bar{s}_1 = 2f_t/3$, $\bar{s}_2 = \bar{s}_3 = -f_t/3$, $\bar{\rho} = \sqrt{2/3}f_t$, and $r = 1/e$. Substituting these into Eq. (3.29) yields $\tilde{\varepsilon} = f_t/E$, which validates the effectiveness of Eq. (3.29).

3.3.3.1 Tensile Damage

As stated earlier, the CDPM2 treats tensile damage and compressive damage separately. The following explains how they are formulated in the model. First, the tensile damage variable ω_t is determined based on the prescribed stress-inelastic strain relation in uniaxial tension, such as the one shown in Figure 3.5. In the figure, the inelastic strain ε_i is defined using three scalar history variables κ_{dt}, κ_{dt1}, and κ_{dt2}. To illustrate how those history variables are related to ε_i, a plasticity stress-strain model combined with one damage variable is considered:

$$\begin{aligned}
\sigma &= (1 - \omega)\bar{\sigma} \\
&= (1 - \omega)E(\varepsilon - \varepsilon_p) \\
&= E\{\varepsilon - [\varepsilon_p + \omega(\varepsilon - \varepsilon_p)]\} \\
&= E(\varepsilon - \varepsilon_i)
\end{aligned} \tag{3.30}$$

where ε_i is the inelastic strain, defined as $\varepsilon_i = \varepsilon_p + \omega(\varepsilon - \varepsilon_p)$, and ω is the damage parameter. The graphical interpretation of the variables used in the above equation is presented in Figure 3.6, where ε_p is irreversible and $(\varepsilon - \varepsilon_p)$ in the third line of Eq. (3.30) is reversible. For more details, refer to the work of Grassl (2008). Applying this concept to the model with tensile damage only, the inelastic strain ε_i can be defined as

$$\varepsilon_i = \kappa_{dt1} + \omega_t\kappa_{dt2} \tag{3.31}$$

The part $(\varepsilon - \varepsilon_p)$ in the second line of Eq. (3.30) can be replaced with κ_{dt}, and thus Eq. (3.30) becomes

$$\sigma = (1 - \omega_t)E(\varepsilon - \varepsilon_p) = (1 - \omega_t)E\kappa_{dt} \tag{3.32}$$

All the above history variables κ_{dt}, κ_{dt1}, and κ_{dt2} are defined in the rate form as

$$\dot{\kappa}_{dt} = \dot{\bar{\varepsilon}} \tag{3.33}$$

$$\dot{\kappa}_{dt1} = \begin{cases} \|\dot{\varepsilon}_p\|/x_s & \text{if } \dot{\kappa}_{dt} > 0 \text{ and } \kappa_{dt} > \varepsilon_0 \\ 0 & \text{if } \dot{\kappa}_{dt} = 0 \text{ or } \kappa_{dt} > \varepsilon_0 \end{cases} \tag{3.34}$$

$$\dot{\kappa}_{dt2} = \dot{\kappa}_{dt}/x_s \tag{3.35}$$

$$\text{where} \quad x_s = 1 + (A_s - 1)R_s \tag{3.36}$$

$$R_s = \begin{cases} -\sqrt{6}\bar{\sigma}_V/\bar{\rho} & \text{if } \bar{\sigma}_V \leq 0 \\ 0 & \text{if } \bar{\sigma}_V > 0 \end{cases} \tag{3.37}$$

In the above equations, x_s is the softening ductility measure, that is analogous to x_h of Eq. (3.27). A_s is the model parameter determined from the softening response under uniaxial compression. To be specific, the effective stress in uniaxial compression can be defined as $\bar{\sigma}_1 = -\sigma_c$ and $\bar{\sigma}_2 = \bar{\sigma}_3 = 0$. It follows that $\bar{\sigma}_V = -\sigma_c/3$ and $\bar{\rho} = \sqrt{2/3}\sigma_c$, and thus $\bar{\sigma}_V/\bar{\rho} = -1/\sqrt{6}$. Plugging $\bar{\sigma}_V/\bar{\rho} = -1/\sqrt{6}$ into Eq. (3.37) gives $R_s = 1$, which results in $x_s = A_s$ by Eq. (3.36).

The bilinear stress-inelastic strain relation for tension softening shown in Figure 3.5 is defined as

$$\sigma = \begin{cases} f_t - (f_t - \sigma_1)\varepsilon_i/\varepsilon_{f1} & \text{if } 0 < \varepsilon_i \leq \varepsilon_{f1} \\ \sigma_1 - \sigma_1(\varepsilon_i - \varepsilon_{f1})/(\varepsilon_i - \varepsilon_{f1}) & \text{if } \varepsilon_{f1} < \varepsilon_i \leq \varepsilon_f \\ 0 & \text{if } \varepsilon_f < \varepsilon_i \end{cases} \tag{3.38}$$

where ε_f is the threshold at which the uniaxial tensile stress is equal to zero; ε_{f1} is the threshold at which the uniaxial tensile stress is equal to σ_1 described in the figure.

Now, setting Eq. (3.32) equal to Eq. (3.38) with ε_i substituted by Eq. (3.31) and solving for ω_t gives

$$\omega_t = \begin{cases} \dfrac{(E\kappa_{dt} - f_t)\varepsilon_{f1} - (\sigma_1 - f_t)\kappa_{dt1}}{E\kappa_{dt} + (\sigma_1 - f_t)\kappa_{dt2}} & \text{if } 0 < \varepsilon_i \leq \varepsilon_{f1} \\ \dfrac{E\kappa_{dt}(\varepsilon_f - \varepsilon_{f1}) + \sigma_1(\kappa_{dt1} - \varepsilon_f)}{E\kappa_{dt}(\varepsilon_f - \varepsilon_{f1}) - \sigma_1\kappa_{dt2}} & \text{if } \varepsilon_{f1} < \varepsilon_i \leq \varepsilon_f \\ 0 & \text{if } \varepsilon_f < \varepsilon_i \end{cases} \tag{3.39}$$

To ensure a mesh-independent softening response, fracture energy is used to estimate the value of ω_t. For the bilinear softening law as in Figure 3.5, the tensile fracture energy G_f is the area under the curve and is calculated as

$$G_f = (f_t w_{f1} + \sigma_1 w_f)/2 \tag{3.40}$$

where w_{f1} and w_f are the displacement thresholds and have a relation with ε_{f1} and ε_f, such that $w_{f1} = \varepsilon_{f1}L_e$ and $w_f = \varepsilon_f L_e$, in which L_e is the characteristic length of the finite element mesh.

According to Jirásek & Zimmermann (1998), it is reasonable to assume that $\sigma_1/f_t = 0.3$ and $w_{f1}/w_f = 0.15$, which follows that $w_f = G_f/(0.225 f_t)$. Then, replacing ε_{f1} and ε_f in Eq. (3.39) with w_{f1} and w_f gives

$$\omega_t = \begin{cases} \dfrac{(E\kappa_{dt} - f_t)w_{f1} - (\sigma_1 - f_t)\kappa_{dt1}L_e}{E\kappa_{dt}w_{f1} + (\sigma_1 - f_t)\kappa_{dt2}L_e} & \text{if } 0 < \varepsilon_i L_e \leq w_{f1} \\ \dfrac{E\kappa_{dt}(w_f - w_{f1}) + \sigma_1(\kappa_{dt1}L_e - w_f)}{E\kappa_{dt}(w_f - w_{f1}) - \sigma_1\kappa_{dt2}L_e} & \text{if } w_{f1} < \varepsilon_i L_e \leq w_f \\ 0 & \text{if } w_f < \varepsilon_i L_e \end{cases} \qquad (3.41)$$
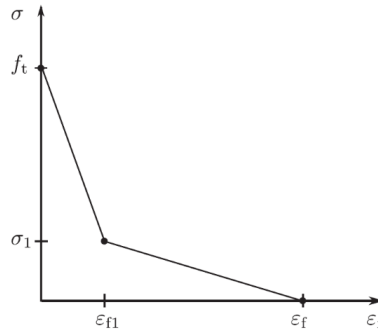
Figure 3.5 Bilinear stress-inelastic relation for softening (Grassl et al., 2013)
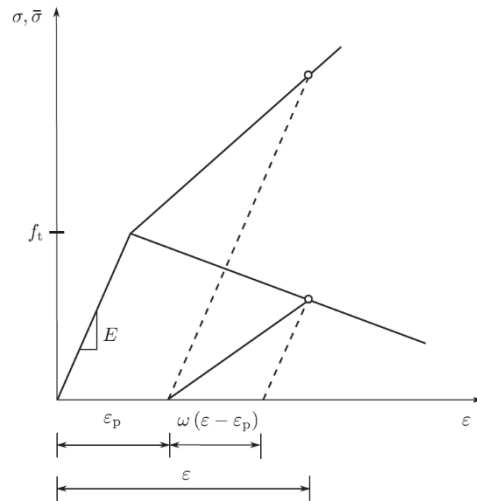
Figure 3.6 Graphical representation of ε, ε_p, ε_i, and ω for the damage-plasticity model with one damage variable. The dashed line represents elastic unloading with the same stiffness as the initial elastic stiffness E (Grassl et al., 2013)

3.3.3.2 Compressive Damage

In a similar way, the compression damage variable ω_c is defined using three scalar history variables κ_{dc}, κ_{dc1}, and κ_{dc2}, which are defined in the rate form as

$$\dot{\kappa}_{dc} = \alpha_c \dot{\tilde{\varepsilon}} \tag{3.42}$$

$$\dot{\kappa}_{dc1} = \begin{cases} \alpha_c \beta_c \|\dot{\varepsilon}_p\|/x_s & \text{if } \dot{\kappa}_{dt} > 0 \text{ and } \kappa_{dt} > \varepsilon_0 \\ 0 & \text{if } \dot{\kappa}_{dt} = 0 \text{ or } \kappa_{dt} > \varepsilon_0 \end{cases} \tag{3.43}$$

$$\dot{\kappa}_{dc2} = \dot{\kappa}_{dc}/x_s \tag{3.44}$$

$$\text{where} \quad \alpha_c = \sum_{i=1}^{3} \frac{\bar{\sigma}_{pc,i}(\bar{\sigma}_{pt,i} + \bar{\sigma}_{pc,i})}{\|\bar{\sigma}_p\|^2} \tag{3.45}$$

$$\beta_c = \frac{f_t q_{h2}\sqrt{2/3}}{\bar{\rho}\sqrt{1 + 2D_f^2}} \tag{3.46}$$

Here, $\bar{\sigma}_{pt,i}$ and $\bar{\sigma}_{pc,i}$ are the tensile and compressive stress components of the principal effective stresses, respectively. The variable α_c takes the portion of compressive stress with respect to the given effective stress tensor, which varies from 0 for pure tension to 1 for pure compression. The variable β_c is introduced to provide a smooth transition from pure damage to damage-plasticity softening process, which can take place during cyclic loading.

The stress-inelastic strain relation for compression softening is defined in the exponential form as

$$\sigma = f_t \exp(-\varepsilon_i/\varepsilon_{fc}) \quad \text{if } \varepsilon_i > 0 \tag{3.47}$$

where ε_{fc} is the inelastic strain threshold determining the initial inclination of the compressive softening curve.

As is done for the tension case in Eq. (3.31) and Eq. (3.32), it can be defined that $\varepsilon_i = \kappa_{dc1} + \omega_c \kappa_{dc2}$ and $\sigma = (1 - \omega_c)E\kappa_{dc}$. Substituting the first equation into Eq. (3.47) and equating that to the second equation yields a nonlinear equation that can be solved for ω_c using a numerical algorithm such as a modified Newton-Rapson iteration method.

3.4   Comparisons of Concrete Models

In this section, yield functions and approaches to material dilatancy and ductility for the CDP model and CDPM2 are compared, as they are the key components to differentiate between the two

models and eventually make the difference in model performance, particularly under high confining pressure states. It is noted that modeling material dilatancy is incorporated in hardening/softening rules.

3.4.1 Yield Function

In material constitutive equations, yield function is used to determine the onset of strength loss of the material, i.e., occurrence of plastic flow. The yield surface increase/decrease according to the material's hardening/softening. When concrete reaches its maximum strength, the resultant yield surface is called the failure surface. Thus, the failure surface is designed to represent concrete failure test data under diverse multiaxial stress states. In Figure 3.7, the tensile meridian (TM) and compressive meridian (CM) of the failure surfaces of the CDP model and CDPM2 are compared with the test data from the literature (Ansari & Li, 1998; Attard & Setunge, 1996; Balmer, 1949; Candappa et al., 2001; Chinn & Zimmerman, 1965; Imran, 1996; Kotsovos & Newman, 1980; Lan & Guo, 1999; Mills & Zimmerman, 1970; Richart et al., 1928; Schickert & Winkler, 1977; Sfer et al., 2002; Smith et al., 1989; Xie et al., 1995). The CDP model's yield function f_p follows a linear relationship between $\bar{\rho}$ and $\bar{\sigma}_V$ (Eq. (3.10)); it therefore tends to overestimate the concrete yield stress limit as the volumetric stress component (or hydrostatic pressure) increases, as evidenced by the literature (Lim et al., 2016). The model's TM shows a large deviation from the test data than the CM. Hence, in RC bond pullout problem (CHAPTER 4), as the concrete material in the bond-zone experiences the high-pressure stress state, the model's overestimated yield function can lead to an unsatisfactory concrete response. On the other hand, the CDPM2's yield function f_p follows the nonlinear relationship between $\bar{\rho}$ and $\bar{\sigma}_V$ (Eq. (3.17)), which provides a relatively better fit to the test data, as $\bar{\sigma}_V$ increases, particularly on TM.
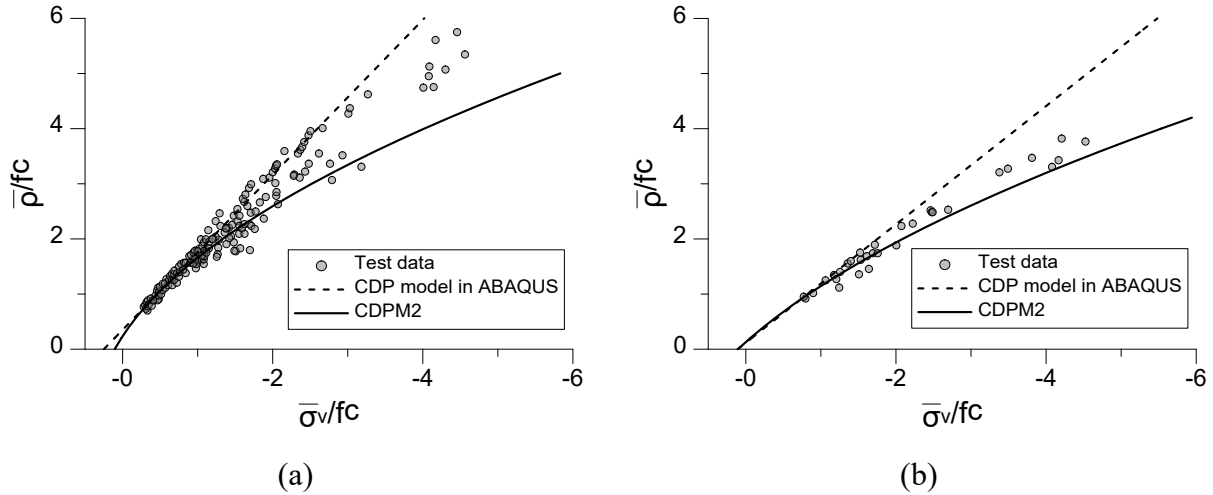
Figure 3.7 Failure surfaces of CDP model and CDPM2 on the (a) compression and (b) tension meridian sections, in comparison with the test data

3.4.2 Approach to Material Dilatancy

Granular materials require non-associative flow rule (i.e., yield function f_p and plastic flow function g_p are not identical) to reproduce realistic dilatancy of the materials. Concrete models considered in this study adopt the non-associative flow rule as well, as concrete acts like a granular material. Figure 3.8(a) shows yield function and non-associative plastic flow function of the CDP model when the current stress is on the yield function, and how the dilatancy of concrete material is determined in the CDP model. In the figure, plastic strain increment $d\boldsymbol{\varepsilon}_p$ at the given stress state is determined as perpendicular to the plastic flow function. Then, the $\bar{\sigma}_V$-direction component of $d\boldsymbol{\varepsilon}_p$ represents the material dilatancy (volume change). However, it has been found that in the CDP model, taking advantage of the non-associative flow rule is not enough to achieve the realistic dilation (Lim et al., 2016; Poliotti & Bairán, 2019; Yu et al. 2010). Specifically, the CDP model takes the linear relationship between $\bar{\rho}$ and $\bar{\sigma}_V$ to define the plastic flow function g_p with a fixed slope (Eq. (3.15)), which leads to the dilation overestimation under heavily confined conditions (Lim et al., 2016; Poliotti & Bairán, 2019; Yu et al., 2010). As a result, the CDP model overestimates the axial stress and underestimates the corresponding strain in case of the concrete specimens subjected to axial compression and uniform lateral confining pressure (Lim et al., 2016). This is strongly attributed to the poor dilatancy reproduction and is partly due to the overestimated yield surface stated earlier. Simulating the proper dilatancy of the granular material under different

multiaxial stress states is a complicated problem and is still an open challenge. Some research imposed adaptive dilation angle that is assumed to be dependent on the current stress/strain state, instead of the fixed dilation angle for ψ in Eq. (3.15) (Lim & Ozbakkaloglu, 2014; Poliotti & Bairán, 2019). Alternatively, a plastic flow function that takes the nonlinear relationship between $\bar{\rho}$ and $\bar{\sigma}_V$ with the gradually lower slope with the larger $\bar{\sigma}_V$ was used, like the CDPM2 (Figure 3.8(b) and Eq. (3.22)). Additionally, the CDPM2 employs a hardening ductility measure to make the material response be more ductile under compression than under tension (Eqs. (3.27) and (3.36)).
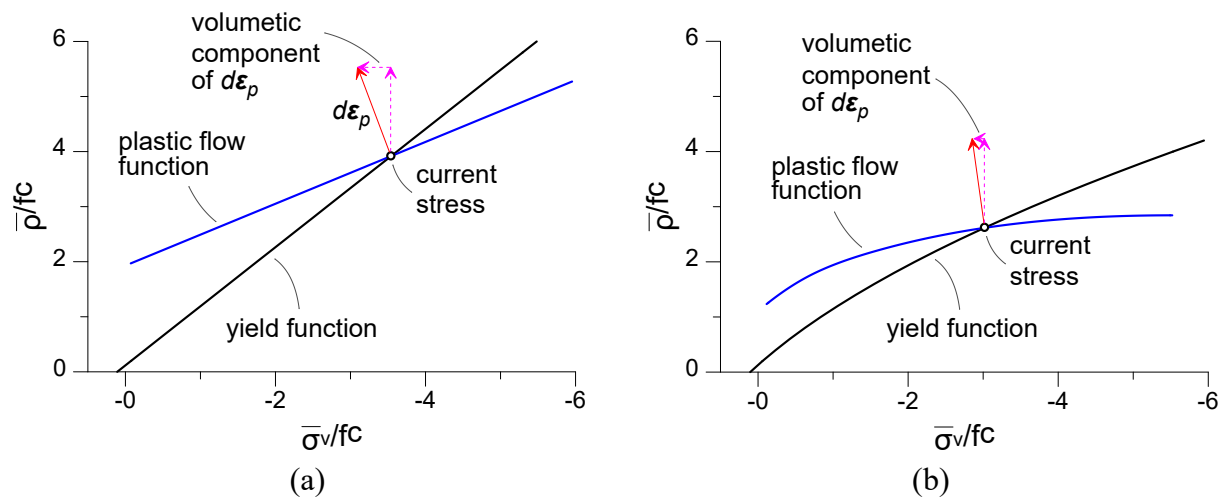
Figure 3.8 Geometric representation of the concrete material dilatancy (a) in CDP model and (b) CDPM2

3.5   Evaluation of Concrete Damage-Plasticity Models

The performance of the concrete models discussed above is evaluated using existing experimental results from concrete uniaxial, biaxial, and triaxial compression tests and uniaxial tension tests. To this end, CDPM2 is implemented in ABAQUS by the author. The material properties of FE models for those tests are listed in Table 3.1. All the FE models are made of a single 3D cubic element with an edge length of 100 mm (3.94 in.).

For the CDP model, the model input parameters or data are defined as follows. Concrete material response in compression is defined using a set of stress-strain data. The stress-strain model proposed by Yang et al. (2014) is used to simulate concrete compressive response, where the

measured Elastic modulus value presented in Table 3.1 is used instead of the one calculated by the model. The post-peak behavior of the model is then adjusted to give a linear softening branch such that a stress of 20% f_c is reached at the prescribed residual strain (ε_{20}). This value is defined as 0.011 and 0.0081 for uniaxial/biaxial tests and triaxial tests, respectively. It is noted that the ε_{20} value doesn't affect the uniaxial tension test. The details about determining ε_{20} will be discussed in Chapter 5.4.3. In addition, plasticity parameters, which include the dilation angle (ψ), eccentricity (ϵ), ratio of biaxial compressive strength to uniaxial compressive strength (f_{bc}/f_c), and ratio of the second stress invariant on the tensile meridian to that on the compressive meridian at initial yield (K_c), are defined as 31°, 0.1, 1.16, and 0.66, respectively.

The material parameters for CDMP2 are set as follows: $A_h = 0.08$, $B_h = 0.003$, $C_h = 2$, $D_h = 1.0 \times 10^{-6}$, $A_s = 5$, $D_f = 0.85$, $H_p = 0.01$, and $\varepsilon_{fc} = 1.0 \times 10^{-4}$. All these values are the recommended values by the authors who developed the model (Grassl et al., 2013).

The first analyses involve uniaxial and biaxial compression tests (Kupfer et al., 1969). In the experiments, concrete specimens with the size of 200 x 200 x 50 mm (7.9 x 6.9 x 2.0 in.) were subjected to uniaxial or biaxial compression in the long axis (axes) of the specimens (i.e., axis parallel to 200 mm length). The thin thickness (50 mm) of the specimen was intended to prevent the noticeable deviations from a uniform stress distribution across the specimen thickness (Kupfer et al., 1969). In Figure 3.9, each model response is compared with its corresponding test data. The CDP model and CDPM2 responses provide similar results and agree well with the experimental data.

The next evaluation is done for the triaxial compression test (Imran & Pantazopoulou, 1996). In the experiments, concrete cylinder specimen was subjected to a constant lateral confining pressure and was axially compressed until enough hardening curve was achieved. The test was repeated for three different confining pressure levels, 2.49 ksi (17.2 MPa), 4.37 ksi (30.1 MPa), and 6.24 ksi (43 MPa). Figure 3.10 compares the concrete responses between simulated using both concrete materials and measured from the test. It is shown that CDPM2 reasonably captured the test data, whereas CDP model significantly deviated. For the CDP model, such disagreement gets prominent as higher confining pressure is applied. This observation is a well-known drawback of CDP model reported in the literature (Lim et al., 2016; Simulia, 2014; Yu et al., 2010), and is attributed to the model's poor ability to reproduce the material's dilatancy in high hydrostatic stress states. As the dilation of concrete is over- or under-predicted, higher or lower stress is developed

within the material compared to the experimental data. For example, in case of the model subjected to the confining pressure of 6.25 ksi (43 MPa), stress values after the onset of softening are largely over-predicted, and even display an artificial "hardening" effect, as shown in Figure 3.10.

Lastly, the concrete models are tested for uniaxial tension case (Gopalaratnam & Shah, 1985). Figure 3.11 shows that both concrete models simulate the measured data well up to the concrete tensile strength. Once the models reach the concrete tensile strength, different softening responses are observed. The CDP model exhibits a linear softening response, as it follows the fracture energy concept when defining the softening response, which, by default in ABAQUS, assumes a linear softening curve. The assumption of such linear softening could lead to delayed concrete softening response. By contrast, a bilinear softening response is chosen for CDPM2, which reasonably captures the test data.

Overall, CDPM2 can reproduce concrete nonlinearity under different multiaxial stress states, whereas CDP model has significant limitations in the triaxial compression condition. This observation emphasizes the importance of carefully selecting a concrete model for the purpose of physics-based simulation. This, however, does not suggest that CDPM2 must be used in all simulations. As stated earlier, the implementation of a new material model such as CDPM2 into ABAQUS requires a great amount of effort. The default model (CDP model) is adequate for cases with low confinement. For example, simulating bar splice failure induced by concrete cover cracking via the rib-scale FE modeling approach can be achieved using CDP model available in ABAQUS, as the failure mechanism for this particular test doesn't exhibit the concrete crushing response typically occurring at high hydrostatic pressure condition. The details about this type of simulation will be discussed in CHAPTER 5. On the other hand, simulating the pullout behavior of RC bond via the rib-scale FE modeling approach requires a more elaborate concrete model such as CDPM2, because concrete surrounding the reinforcement being pulled on undergoes both concrete crushing and cracking. This application will be presented in CHAPTER 4.

Table 3.1 Material properties used for the evaluation of concrete models

| Applied loading type | Material properties | | | | | | Reference |
	f_c	f_t	E	G_f	G_{fc}	ν	
Uniaxial compression (σ_1/σ_2= -1/0)	4.8 (32.8)	0.48 (3.3)	4600 (32)	0.52 (0.091)	114 (20)	0.2	Kupfer et al., (1969)
Biaxial compression (σ_1/σ_2= -1/-1)							
Triaxial compression	6.9 (47.4)	0.69 (4.74)	4400 (30)	0.57 (0.010)			lmran & Pantazopoulou (1996)
Uniaxial tension	5.8 (40)	0.51 (3.5)	4100 (28)	0.31 (0.055)			Gopalaratnam & Shah (1985)
Note: all values are in US units, whereas the values in parenthesis are in SI units. f_c: concrete compressive strength, ksi (MPa) $\quad$ G_f: concrete fracture energy, lb/in. (N/mm) f_t: concrete tensile strength, ksi (MPa) $\quad\quad$ G_{fc}: concrete crushing energy, lb/in. (N/mm) E: elastic modulus of concrete material, ksi (GPa) $\quad$ ν: Poisson's ratio							
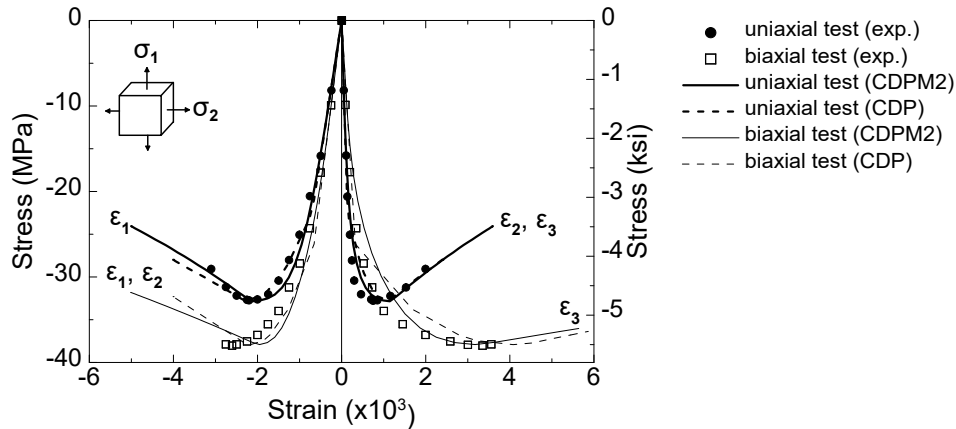
Figure 3.9 Comparison of concrete models responses with experimental data from uniaxial and biaxial compression tests (Kupfer et al., 1969)
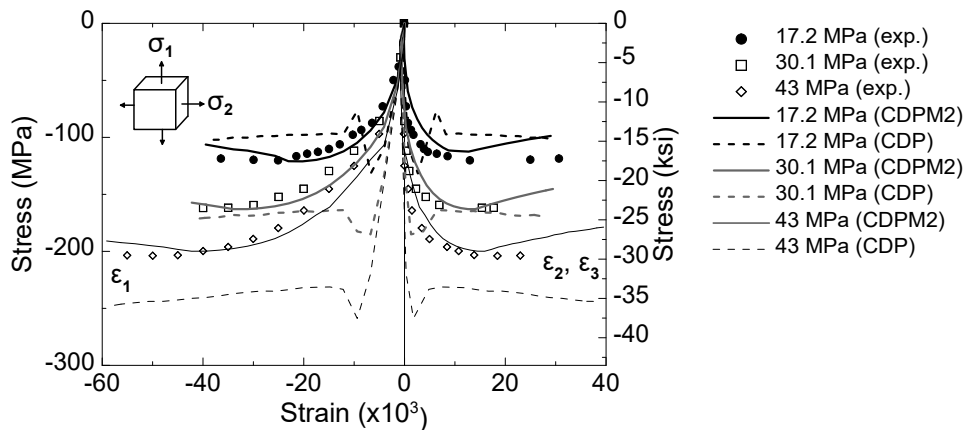
Figure 3.10 Comparison of concrete models responses with experimental data from triaxial compression tests (Imran & Pantazopoulou, 1996)
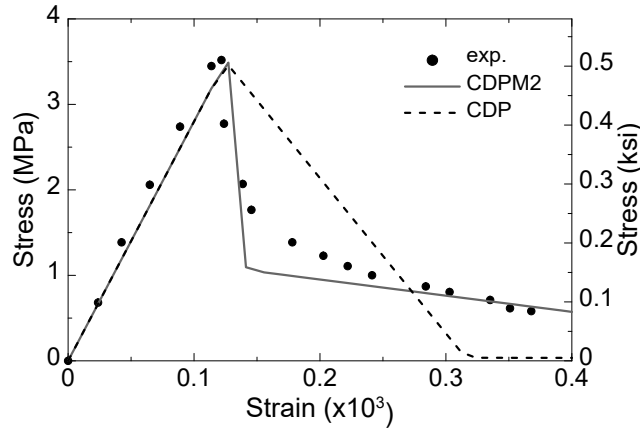
Figure 3.11 Comparison of responses of concrete models with experimental data from uniaxial tension test (Gopalaratnam & Shah, 1985)

3.6   Conclusions

RC bond failure mechanism exhibits highly nonlinear behavior of concrete material, involving a combination of concrete compressive crushing and tensile cracking. Therefore, the concrete model used must be well understood from a constitutive modeling and mechanical point of view. Of many concrete constitutive models proposed in the literature, two concrete models based on the framework of the damage-plasticity model are selected for discussion: (1) CDP model and (2) CDPM2. The first model is one of the most commonly used concrete models in the literature. The second is one of the recently developed models and is characterized by its ability to predict a wide range of experimental results of concrete subjected to multiaxial stress states.

The CDP model implements a linear yield function, of which the evolution is determined based on the accumulated plastic strain. Hardening and softening responses are dependent on the size of the evolving yield function. A non-associative plastic flow based on the Drucker-Prager hyperbolic function is used, which also takes the form of a linear function.

The CDPM2 assumes a nonlinear yield function to represent realistic concrete yield surface observed in experimental tests. A non-associative plastic potential function is defined in the nonlinear form. One notable feature of the model is its use of the effective (undamaged) stress space to introduce the scalar-valued inelastic strain. It enables a quantitative determination of damage in tension and compression. Another feature of the model is the introduction of an adoptive ductility measure dependent on the current volumetric stress state in order to simulate realistic dilatancy.

The performance of the two models is tested for different loading conditions: uniaxial, biaxial, triaxial compression and uniaxial tension. The comparison of model responses with test data shows that both models predict the responses of concrete subjected to uniaxial and biaxial compression and uniaxial tension well. In the triaxial compression condition, the response predicted by the CDP model deviated considerably from test data. This arises from the model's poor ability to reproduce the material's dilatancy in high hydrostatic stress states. The CDPM2 shows a good agreement with the triaxial compression test data.

CHAPTER 4.   FINITE ELEMENT SIMULATION OF PULLOUT BEHAVIOR OF REINFORCEMENT-CONCRETE BOND

4.1   Introduction

Reinforced concrete (RC) is a composite structural material comprising reinforcing steel embedded within concrete; adequate force transfer between concrete and steel, typically referred to as bond, is required to achieve composite action. A standard way of investigating RC bond behavior, including bond-zone load transfer mechanism, factors that affect bond strength, and bond force (or stress) versus slip relationship, is to conduct the pullout test. The pullout test is done in a way that single straight reinforcement embedded with short embedment length in concrete cylinder or prism (Figure 4.1) is axially pulled on until the failure of the test specimen. The "short" embedment length is intended to provide a uniform bond stress distribution along the bonded area, which enables the measurement of pure bond force.

Finite element analysis (FEA) is used often to supplement experimental testing to investigate behavior and design of structural systems and components. For RC components and systems subjected to loading, accurate simulation of response requires accurate simulation of concrete and steel material response as well as accurate simulation of bond between concrete and reinforcing steel (i.e., bond-zone response). Typically, bond-zone response is modeled using bar-scale models that define a one-dimensional (1D) bond stress versus slip displacement relationship at the concrete-steel interface. Chen et al. (2011), Erfanian & Alaa (2019), and Murcia-Delso & Shing (2014, 2015) have proposed these types of models and demonstrated their effectiveness in simulating the impact of bond on component and system-level response. However, these types of models are limited to the range of material and geometric properties for which they were developed, and thus, reveal limitations when applied to bond-zones with different design parameters that develop different stress fields. To be specific, simulating the behavior of reinforced concrete at this "bar-scale" is challenging for the following reasons. First, it requires accurate simulation of *bond* at the concrete-steel interface. Second, it requires accurate simulation of multi-dimensional concrete response, as failure due to reinforcement pullout results from nonlinear concrete material response (crushing and cracking) caused by the bearing of the ribs. Eventually, the geometry and stress fields around bond-zone require high resolution modeling with highly refined element meshes to achieve accurate results.

Multi-dimensional rib-scale modeling, in which load-deformation response is simulated in both parallel and perpendicular to the reinforcing bar axis, can overcome many of the limitations of 1D bond modeling. Multi-dimensional rib-scale modeling employs solid elements to represent bond-zone geometry, including reinforcement ribs and surrounding concrete (Figure 2.1). In general, a contact model, which controls load transfer between two materials, is used to simulate load transfer between concrete and steel at the bar-concrete interface. Previous studies employing rib-scale modeling include Brown et al. (1993), Lagier et al. (2016), Li (2010), Salem & Maekawa (2004), and Seok et al. (2018). Among them, specific examples simulating bond-zone behavior due to the pullout load of reinforcement are discussed below:

- Salem & Maekawa (2004) simulated the response of pullout specimens using a 2D axisymmetric rib-scale FE model. To achieve accurate simulation of strength, the elastic material modulus for the concrete in the vicinity of the bar was artificially reduced by 50%. Use of a reduced material modulus was justified by the fact that concrete water-cement ratio can increase below a reinforcing bar during construction and result in reduced concrete strength.

- Li (2010) simulated pullout test specimen response using a 3D FE model. Like initial attempts by Salem and Maekawa's and the author, simulated bond zone stiffness and strength were overestimated in comparison with the test data.

- Lagier et al. (2016) simulated the response of lap splice of reinforcing bars in ultra-high-performance fiber-reinforced concrete (UHPFRC), in which two pairs of spliced bars were directly loaded in tension in opposite directions. To obtain the bond-zone response in agreement with measured test data, concrete tensile stress versus strain relationship inputted to the model was calibrated with the concrete tensile strength reduced by almost a half. This calibration was justified by the nonuniform fiber dispersion and orientation over the specimen.

The observation in common with these studies is that concrete material response near the bond-zone was overestimated when inputting measured material properties without any calibration. In this regard, Li (2010) has also acknowledged the need for accurate modeling of concrete response, but not much detail as to how to improve the concrete model has not been addressed. Hence, this study was initiated in an attempt to investigate the reason why concrete models needed to be calibrated when employing rib-scale FE model to simulate bond-zone behavior. To

understand the material mechanisms of concrete response, two different concrete models available in the literature were chosen for discussion: (1) concrete damaged-plasticity (CDP) model (Simulia, 2014), which is included in ABAQUS, and (2) concrete damage-plasticity model 2 (CDPM2), which was originally developed by Grassl et al. (2013) and was implemented as a user-subroutine material *VUMAT* in ABAUQS for use by the authors (Seok, 2019). The first model was chosen because it is one of the most commonly used concrete damage-plasticity models readily found in the literature. Note that the CDP model was designed for the applications in which concrete is subjected to the monotonic/cyclic load under low confining pressures (Simulia, 2014) and the details will be given later. The second model is one of the state-of-the-art concrete models, which has shown great capability of simulating nonlinear response under static/dynamic multiaxial stress states with various range of confining pressures. For this reason, the CDPM2 was chosen for this study, among many other existing models.

The main aim of this study is to propose a physics-based rib-scale FE modeling approach to simulate bond-zone behavior of monotonic pullout test of reinforcement embedded in concrete, based on the material and physical properties (no significant calibration required like the previous studies). The characteristics of the two concrete models were thoroughly compared from a constitutive modeling point of view to give the ground for the significance of concrete model and eventually to identify an appropriate concrete model in application to the rib-scale FE modeling approach to simulate pullout test. The performance of the simulated results with each of the two concrete models was evaluated by comparing them with the experimental results (Lundgren, 2000; Metelli & Plizzari, 2014; Murcia-Delso et al., 2013).

4.2   Experimental Tests Used for Model Development and Calibration

In this study, three different types of pullout test specimens were used for the model development and the validation of the developed rib-scale FE model: (1) plain concrete prism, (2) concrete cylinder with 12.7-mm (No. 4) spiral reinforcement placed at perimeter of the specimen, and (3) concrete cylinder with 1-mm (0.039 in.) thick steel tube, as presented in the sequential order in Table 4.1. These specimens each consisted of a single reinforcement bar embedded with a bonded length equal to $5d_b$, designed to provide a uniform bond stress distribution along the bonded area and to prevent the yielding of reinforcement under loading. Figure 4.2 describes the boundary and loading conditions for each specimen. In all cases, the embedded reinforcing bar was pulled in the

vertical direction, while the vertical movement of the concrete was fixed. It is noted that the first specimen failed by concrete splitting, whereas the second and third ones failed by reinforcement pullout (typically observed in confined specimens). The detailed information about each specimen, including concrete compressive and tensile strength, concrete fracture energy, steel yield strength, rebar diameter, etc., are summarized in Table 4.1.
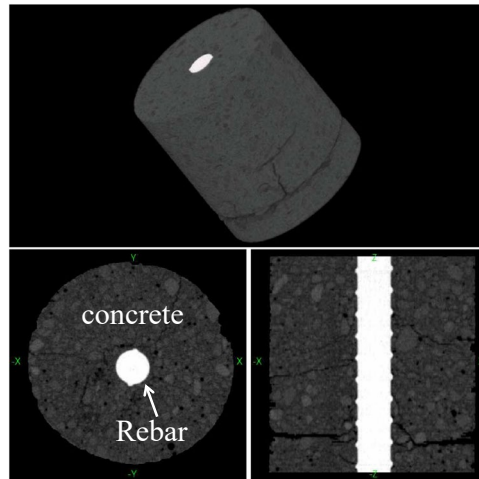
Figure 4.1 Typical configuration of pullout test (X-ray images from Li (2010))

Table 4.1 Material properties of pullout test specimens used for FEA

Test	Failure mode	Concrete					Reinforcement		
		E	ν	f_c	f_t	G_f	f_y	d_b	L_b
Metelli & Plizzari (2014)[1]	SPL	26.7[a] (3870)	0.2	42.7 (6.19)	3.4 (0.49)	0.11[c] (0.64)	940 (136)	20 (0.78)	$5d_b$
Murcia-Delso et al. (2013)[2]	PO	27.6[a] (4000)	0.2	34.5 (5.0)	3.5 (0.51)	0.089[c] (0.51)	420[d] (61)	57 (2.25)	$5d_b$
Lundgren (2000)[2]	PO	28.0[a] (4060)	0.2	36 (5.2)	3.6[b] (0.52)	0.12[c] (0.68)	420[d] (61)	16 (0.63)	$5d_b$

Note: all values are in SI units, whereas the values in parenthesis are in US units.
SPL: splitting failure
PO: pullout failure
E: elastic modulus of concrete material, GPa (ksi)
ν: Poisson's ratio
f_c: concrete compressive strength, MPa (ksi)
f_t: concrete tensile strength, MPa (ksi)
G_f: concrete fracture energy, N/mm (lb/in.)
f_y: yield strength of steel reinforcement, MPa (ksi)
d_b: diameter of reinforcement, mm (in.)
L_b: embedment length of reinforcement

[1] specimen with no confinement
[2] specimen with confinement
[a] estimated using the model proposed by Yang et al. (2014)
[b] estimated as $f_c/10$.
[c] estimated using Eq. (2.1)
[d] assumed as Grade 60 steel
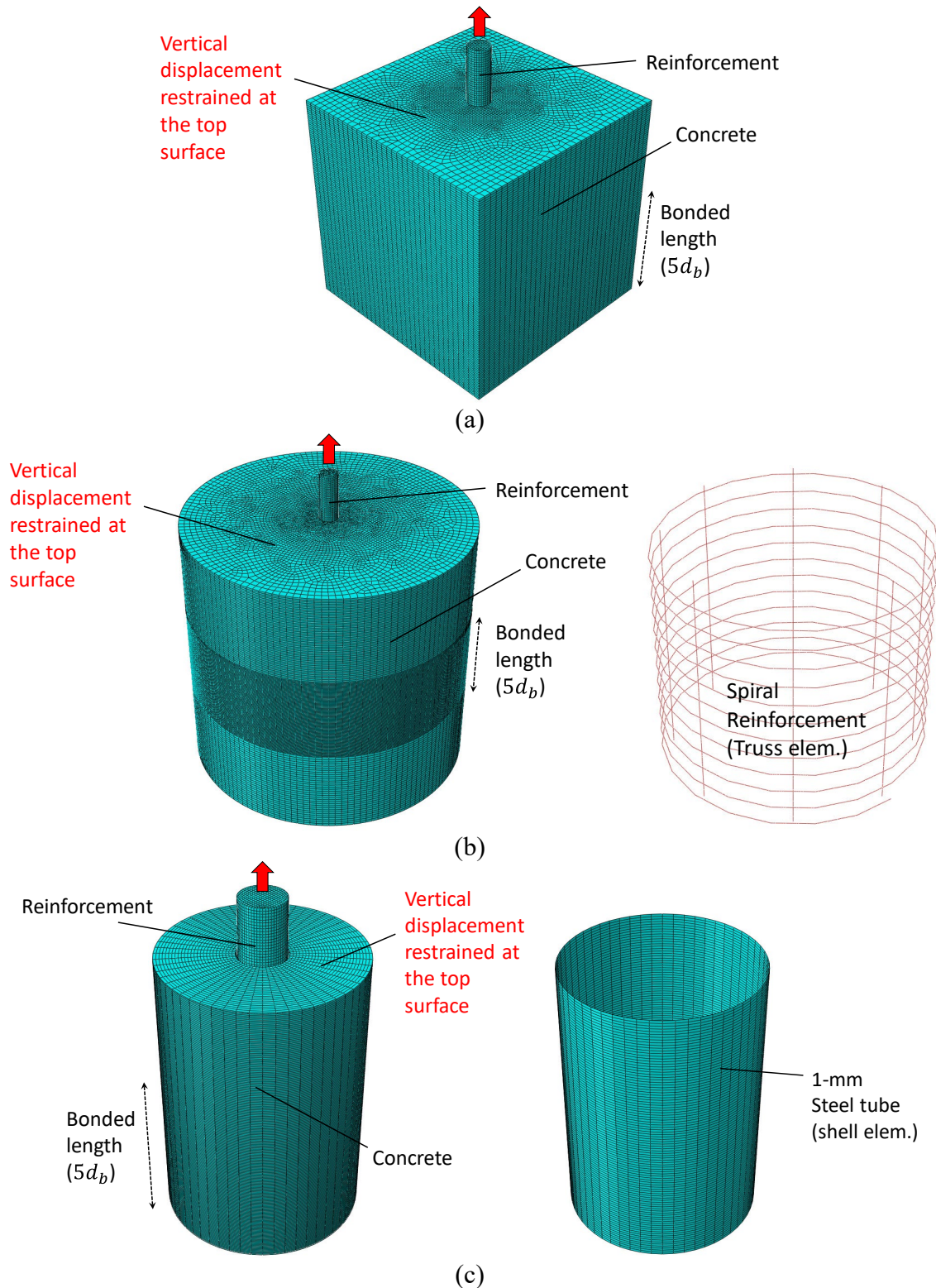
Figure 4.2 FE models of pullout test specimens and their boundary/loading conditions: FE models of (a) Metelli & Plizzari (2014); (b) Murcia-Delso et al. (2013); and (c) Lundgren (2000)

4.3 Issues in Rib-Scale FE Modeling for Pullout Test

As the preliminary study, the first two pullout out tests (Metelli & Plizzari 2014; Murcia-Delso et al. 2013) listed in Table 4.1 were simulated via the modeling strategy described above. The simulation results were achieved using an ABAQUS model in which concrete material response is simulated using the concrete damaged-plasticity (CDP) model and the general (surface-to-surface) contact model. The CDP model was used as, of all of the ABAQUS concrete models (Chen et al., 2011; Feng et al., 2015; Genikomsou & Polak, 2015; Huang et al., 2015; Nana et al., 2017), it has been considered to be the most suitable model for capturing material damage due to both compressive and tensile loading. The plasticity parameters for the CDP model, which include the dilation angle (ψ), eccentricity (ϵ), ratio of biaxial compressive strength to uniaxial compressive strength (f_{bc}/f_c), and ratio of the second stress invariant on the tensile meridian to that on the compressive meridian at initial yield (K_c), were defined as 31°, 0.1, 1.16, and 0.66, respectively. Use of these values for plasticity parameters have been verified in several literature. Details about the CDP model is given in CHAPTER 3.2. The average size of finite element mesh in the bond-zone were 2.0 mm (0.079 in.) and 5 mm (0.20 in.), respectively, for each specimen. Figure 4.3 shows the bond stress versus displacement response as measured in laboratory pullout tests and as simulated by the authors using the ABAQUS software and rib-scale FE models. In both cases, analyses results showed that the simulated bond stress and initial stiffness were higher than test data. Much higher overestimated values for stress and stiffness were observed in the pullout test with confinement (second specimen), where, for example, the simulated bond stress was about 2.5 times greater than the measured one. These overestimated results are aligned with the results found in previous rib-scale FE modeling for pullout tests (Lagier et al. 2016; Li 2010; Salem & Maekawa 2004).

Evaluation of simulation results suggested two potential reasons for the disparity between simulated and measured response histories: (1) inaccurate simulation of concrete-steel contact using the surface-to-surface contact model and (2) inaccurate simulation of concrete material response due to an inadequate concrete constitutive model. Inaccuracy in the surface-to-surface contact approach was discounted due work by Wriggers & Zavarise (2004), which demonstrated the accuracy and robustness of the model for simulating the sliding response of two blocks. Instead, special attention was paid to choosing a proper concrete model. It can start with a good understanding/prediction of mechanical behavior of concrete, as predicted by the model. In pullout

tests, the concrete "key" placed ahead of the reinforcement ribs experiences severe compressive loading and, ultimately, crushing under high confining pressure condition taking place at the early stages of pullout loading, as shown in Figure 4.4. As the bar continue to be pulled out, the concrete key behind the ribs and those forward-moved ribs make a gap, which eventually leads to the concrete crack opening. At the same time, the concrete in the bond-zone experiences shear deformation. This emphasizes the importance of using a robust concrete material model that can model nonlinear compressive and tensile response under wide range of multiaxial stress states.

(a)   (b)
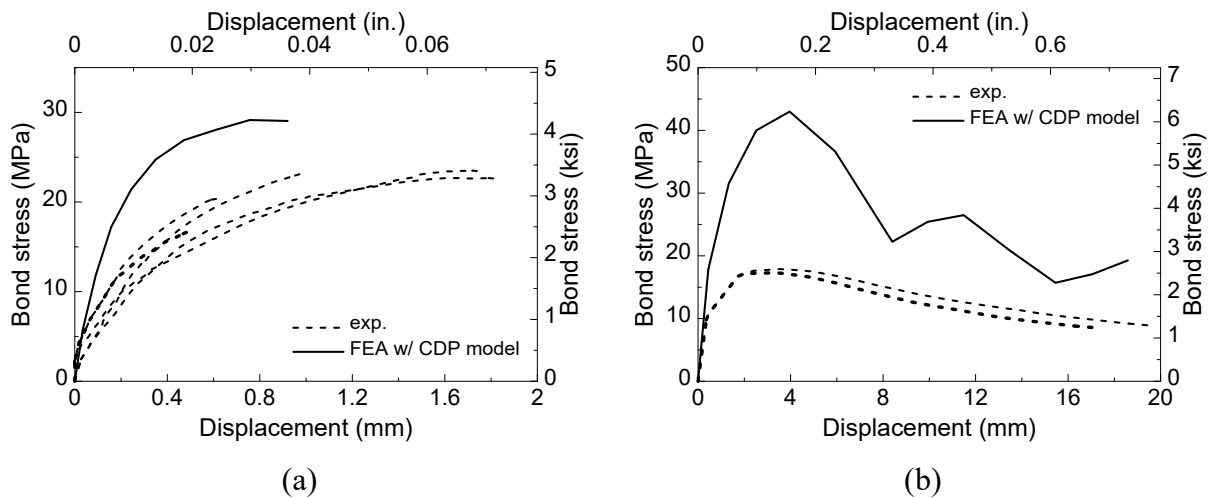
Figure 4.3 Rib-scale FE simulation of reinforcement-concrete pullout specimens using CDP model in ABAQUS: (a) specimen without confinement (Metelli & Plizzari, 2014) (b) specimen with confinement (Murcia-Delso et al., 2013)
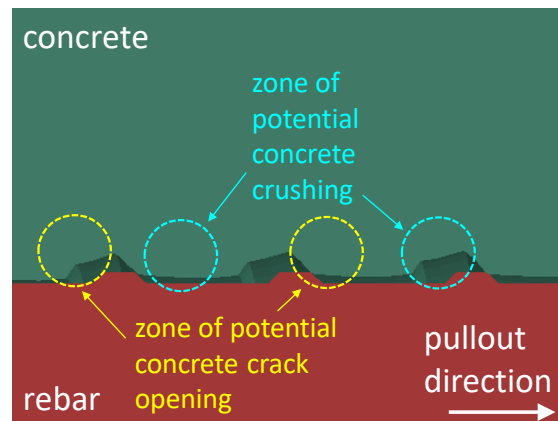
Figure 4.4 Potential zones of concrete crack opening and crushing found in pullout test of reinforcement embedded in concrete

4.4   FE Model Development for Pullout Test

Rib-scale FE models for the three pullout test specimens listed in Table 4.1 were developed using each of the considered concrete models with their corresponding material information. The FE models were created with small enough element sizes to guarantee mesh size-independent response. and one example of mesh sensitivity study results is presented in this section. In addition, impact of tangential friction coefficient in the contact model on simulation results is presented.

4.4.1   FE discretization

Finite element size was determined sufficiently small to create actual geometry of the bond-zone. For example, FE model of the first specimen in Table 4.1 was created with the finite element size of 2 mm (0.079 in.), shown in Figure 4.5. The figure displays a section cut view of the concrete part of the FE model and is shown to well represent the bond-zone topology. Furthermore, the mesh sensitivity study was conducted using different element sizes: 1.7 mm (0.067 in.), 2.0 mm (0.079 in.), and 2.2 mm (0.087 in.). As shown in Figure 4.6, not much difference in response for the considered different sizes of elements was observed, indicating that it is okay to use the element size of 2 mm (reference element size) for this particular analysis. In a similar way, appropriate element size was decided for each following analysis.
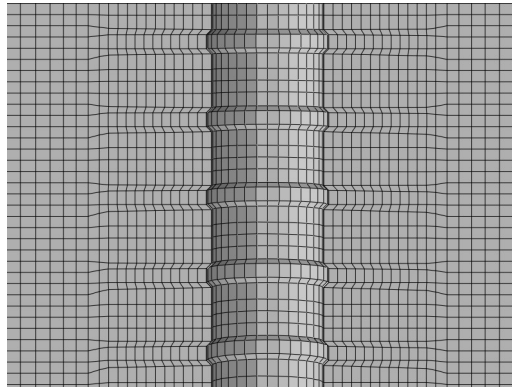
Figure 4.5 Section cut view of element discretization of concrete part in the bond-zone for pullout test specimen
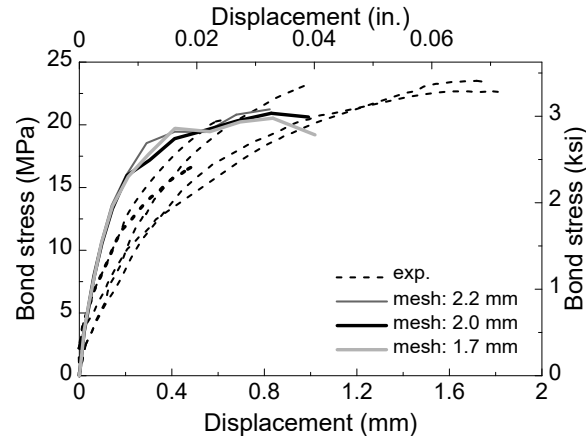
Figure 4.6 Element size sensitivity on FEA results of pullout test (Metelli & Plizzari, 2014)

4.4.2 Impact of Tangential Friction Coefficient in Contact Model

Idun & Darwin (1999) have found the appropriate value for the friction coefficient between normal concrete and steel materials is 0.5. Thus, the effectiveness of this value to rib-scale FE model for pullout test was analyzed by simulating the FE models each using two different tangential friction coefficients (0 and 0.5). Figure 4.7 shows the simulated responses with those two tangential coefficient values, along with the corresponding pullout test data (first specimen). The comparison results indicate that different tangential coefficients didn't have a noticeable impact on results. This implies that in case of pullout test specimens (particularly with short anchorage length), RC bond is governed by the bearing of reinforcement ribs against the surrounding concrete key.
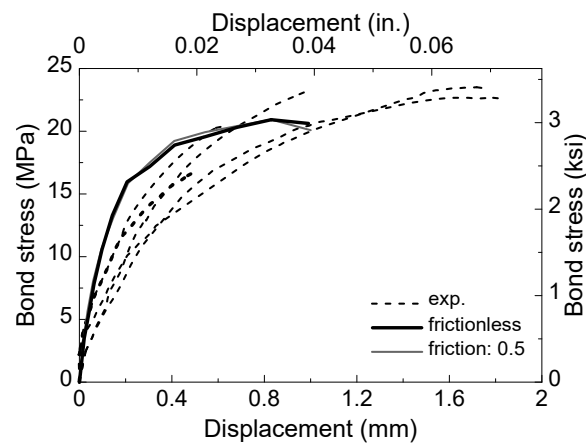
Figure 4.7 FEA results of pullout test, performed with the tangential friction coefficient of 0 (frictionless) and 0.5 and compared with test data (Metelli & Plizzari, 2014)

4.5   FE Simulation Results

4.5.1   Pullout test with no confinement

Based on the modeling methods discussed earlier, a pullout test specimen with no confinement (Metelli & Plizzari, 2014) is simulated. The material properties of the specimen are presented in Table 4.1 and the FE model for the specimen is shown in Figure 4.2 (a).

Figure 4.8 shows the comparison of bond stress-displacement responses obtained using the CDP model and CDPM2 with data measured from the experimental test. Note that bond stress is calculated as $P/(\pi d_b L_b)$, where P is the applied load, and (slip) displacement is measured at the unloaded end of the reinforcement. The results simulated with CDPM2 results in substantially better agreement with test data, in terms of the initial stiffness, peak stress, and displacement at the peak stress, than is provided by the CDP model. Better simulation results with CDPM2 are due to a more accurate estimation of stress in concrete under high volumetric stress states. This arises mainly from the CDPM2's capability of reproducing realistic dilatancy of concrete material under heavy confined conditions, as verified in the material model test for triaxial compression loading (Figure 3.10), and partly from the model's better representation of the concrete yield surface compared with the experimental data (Figure 3.7). Figure 4.9 compares the results simulated using CDP model and CDPM2 with respect to the volumetric stress fields that develop in concrete at peak load. The comparison indicates that concrete around the bond-zone is in a heavily confined condition and CDP model produces higher volumetric stress than CDPM2 does. Particularly, it is shown that the concrete key placed ahead of the reinforcement ribs is in a high-pressure stress states, with values as high as five times greater than the concrete compressive strength when using the CDP model. The CDPM2 produces much less volumetric stress in concrete near the ribs. It should be mentioned that the highest volumetric stress observed in the material test for triaxial compression (i.e., the case of 43 MPa lateral confinement in Figure 3.10) is two times greater than the concrete compressive strength. Based on these results, it can be concluded that the rib-scale FE model requires a concrete model that can simulate nonlinear (hardening/softening) responses under highly confined conditions for successful analysis.

Figure 4.10(a) and Figure 4.10(b) show the concrete tensile (cracking) and compressive (crushing) damages simulated with CDPM2. The test report specifies that the specimen failed by concrete splitting (Figure 4.10 (c)), which is exactly captured in the simulation (Figure 4.10 (a)), where concrete crack develops across the specimen section (i.e., splitting failure pattern). Concrete

crushing by the dowel action around the reinforcement ribs is also reasonably reproduced, as depicted in Figure 4.10 (b).
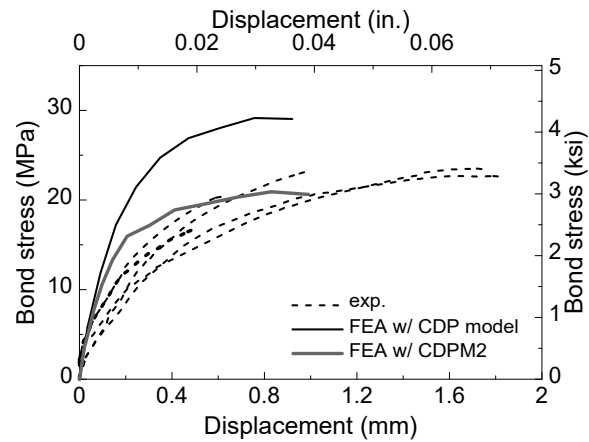
Figure 4.8 Comparison between results simulated with different concrete models (CDP model and CDPM2) and measured in pullout test with no confinement (Metelli & Plizzari, 2014)
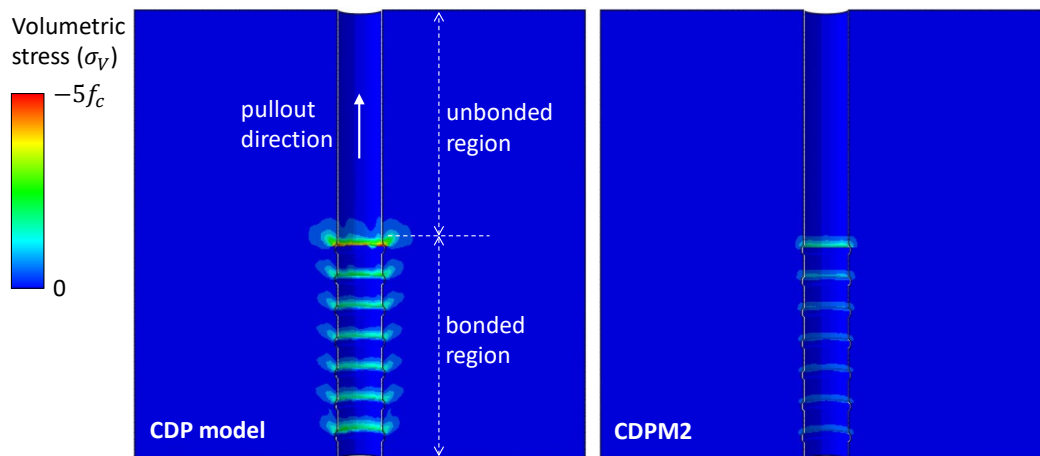
Figure 4.9 Volumetric stress distribution fields of concrete in bond-zone at peak load, viewed at the section across the center of the reinforcement

(a)

(b)

(c)
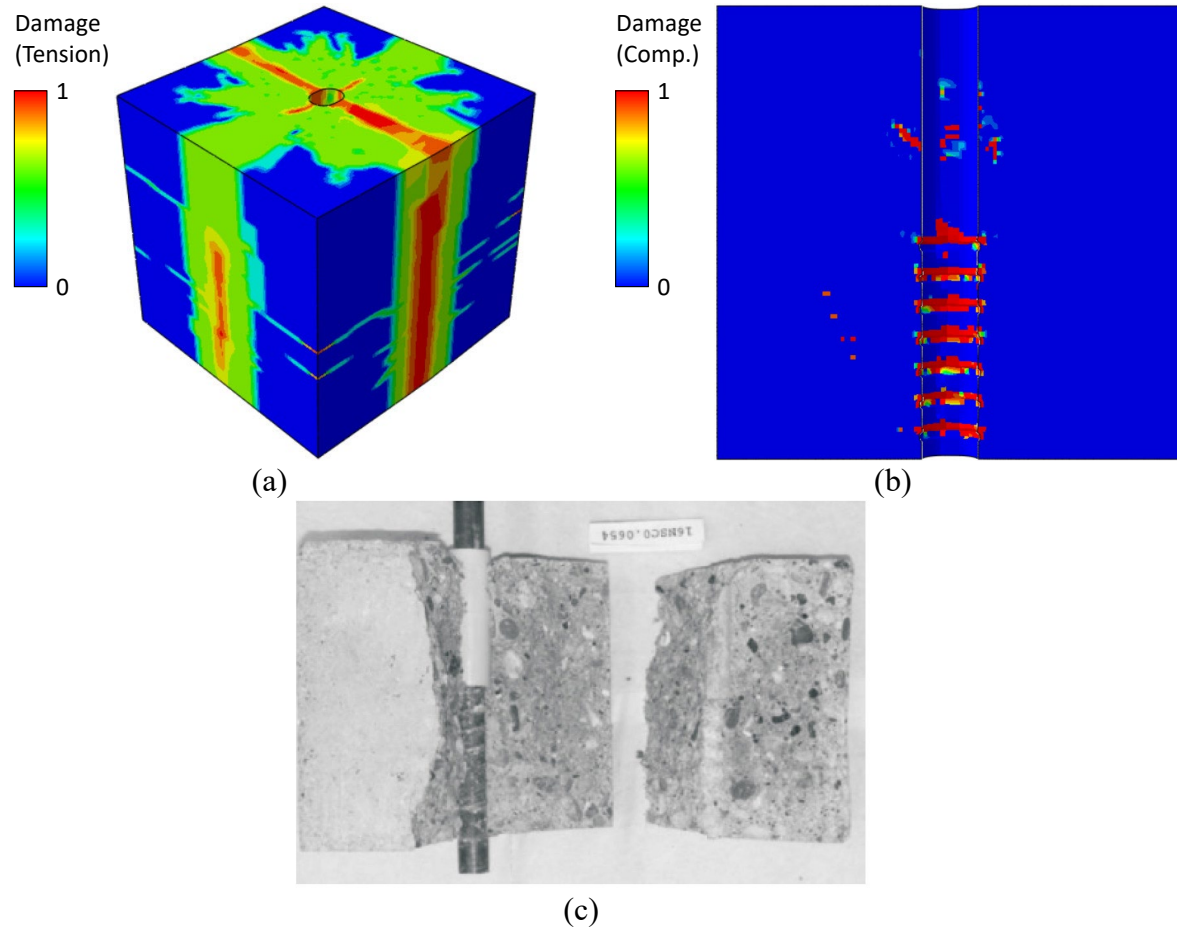
Figure 4.10 Damage patterns at failure: (a) simulated tensile damage (cracking), (b) simulated compressive damage (crushing) at the section, and (c) concrete splitting failure experimentally observed in Metelli & Plizzari (2014). Note that damage index indicates 0 for undamaged and 1 for fully damaged.

4.5.2   Pullout test with confinement

The next analysis is the pullout specimen tested by Murcia-Delso et al. (2013), where the specimen is confined with spiral steel reinforcement (second specimen in Table 3.1). FE model is created such that it has a characteristic element length of about 5 mm (0.20 in.) in the bond-zone, whereas a relatively coarse mesh scheme is used in the outer region, as shown in Figure 4.2 (b). The spiral reinforcement, which provides the confinement effect, is modeled with truss elements, and it is embedded in the "host" concrete solid elements. This *embedded element* technique assumes *perfect* bond between concrete solid elements and rebar truss elements, enforcing that the transitional degrees of freedom of the embedded nodes are constrained to the host elements, whereas the rotational degrees of freedom are not constrained (Simulia, 2014).

Figure 4.11 compares the bond stress-displacement curves between obtained using the CDP model and CDPM2 with experimental test data. The simulation with CDPM2 predicts the initial stiffness well but overestimated the bond stress particularly at the peak load. This can be attributed to the fact that the spiral reinforcement modeled with *perfect* bond with the concrete produced a higher confinement level than what it is to be expected in the test. Thus, it is expected to achieve better simulation results if more realistic constraints between the concrete solid elements and rebar truss elements (e.g., bond constitutive model), which can limit the bond resistance and allow for slip, were used. Modeling such a constraint technique is beyond the scope of this study. The analysis stopped due to a numerical non-convergence issue at around a slip displacement of 10 mm, caused by severe compressive damage in the concrete material that led to an unstable stress update. Specifically, a general return-mapping algorithm for plasticity was used to update the stress, hardening variable (or cumulative plastic strain), and plastic multiplier within each material point, where all these variables were iteratively updated until they satisfied the prescribed criteria using an iterative Newton's method. The numerical issue occurred when the Jacobian matrix became singular due to either the infinite or zero value of the matrix component(s).

Figure 4.12 shows the simulated concrete crack patterns including the crack initiation and propagation. These observed damage patterns imply that the specimen lost its strength gradually, resulting in the gradual slip of the reinforcement (i.e., pullout failure). This contrasts with the previous specimen's failure mode where concrete was split suddenly (i.e., concrete splitting failure).
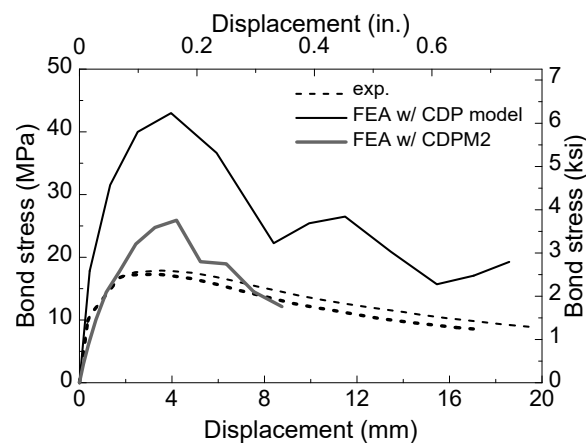

Figure 4.11 Comparison between results simulated with different concrete models (CDP model and CDPM2) and measured in pullout test with confinement of spiral reinforcement (Murcia-Delso et al., 2013)
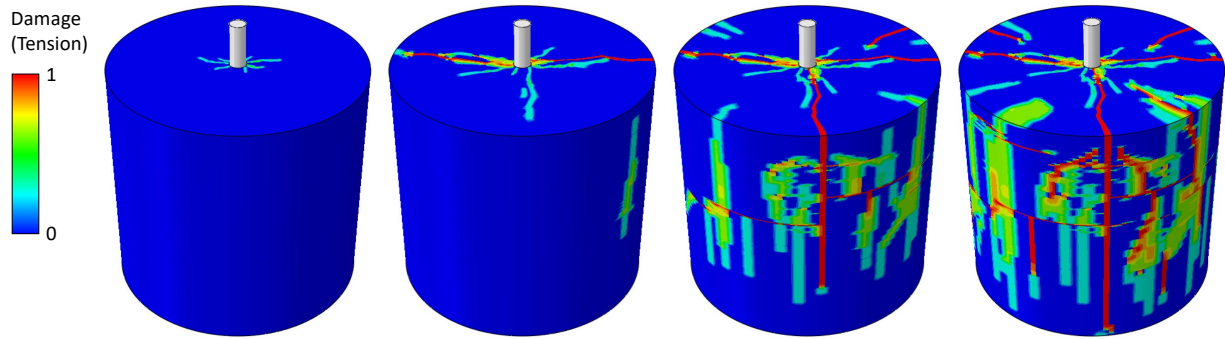
Figure 4.12 Concrete tensile damage (cracking) initiation and its propagation patterns under increasing pullout load. Note that damage index indicates 0 for undamaged and 1 for fully damaged.

Finally, a FE simulation is performed for a pullout test specimen confined with steel tube (third specimen in Table 3.1). A 1-mm steel tube surrounding a concrete cylinder is used to provide confinement on the specimen. The model is created to have a characteristic element length of 1 mm in the bond-zone. The steel tube is assumed to be G60 steel and is modeled with shell elements. The *general* contact (surface-to-surface) formulation is introduced at the interface between the concrete cylinder and steel tube. Within the contact model, *hard* contact is imposed for normal behavior and Coulomb's friction law with the friction coefficient of 0.5 is applied for tangential behavior, whereas cohesive (adhesion) behavior is ignored. The FE model of the specimen is presented in Figure 4.2 (c).

In Figure 4.13, the bond stress-displacement responses simulated with the CDP model but with different tangential friction coefficients (0 and 0.5) defined for the interface between concrete and tube are compared with the test data. Both simulations highly overestimate the bond stress, with values as much as about 2.5 times higher than test data. Particularly, it was observed that the reinforcing bar yielded for both cases and even reached its ultimate strength for the case where a friction coefficient of 0.5 is used. It is noted that reinforcement yielding was not observed in the test.

Figure 4.14 shows the bond stress-displacement responses simulated with CDPM2. The analysis reasonably predicted the peak bond stress and hardening/softening response. However, the analysis stopped at a displacement of 2 mm, due to the same reason stated for the second specimen (an unstable stress update due to severe compressive damage in the concrete material). Figure 4.15 displays the simulated damage patterns at peak stress. It is shown that there is no notable concrete cracking going through the specimen and concrete crushing is localized in the

bond-zone. This indicates that the specimen failed with pullout failure mode, which is in agreement with the experimental observations.
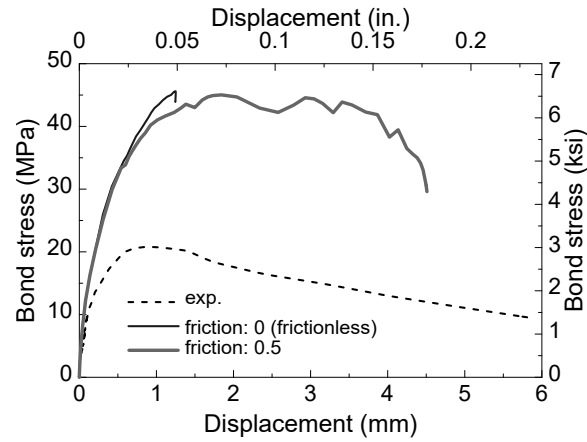
Figure 4.13 Effect of different tangential friction coefficients between concrete and steel tube on bond stress-displacement response
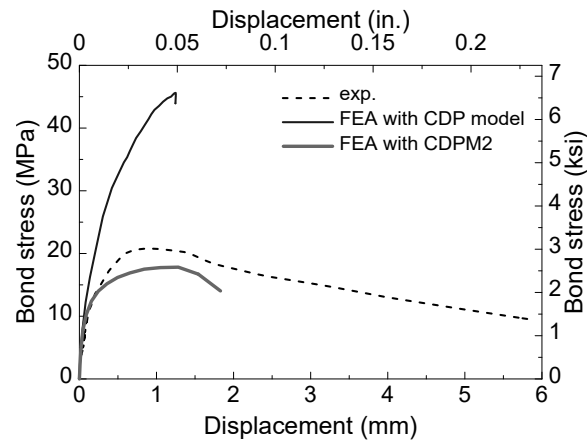

Figure 4.14 Comparison between results simulated with different concrete models (CDP model and CDPM2) and measured in pullout test with confinement of steel tube (Lundgren, 2000)
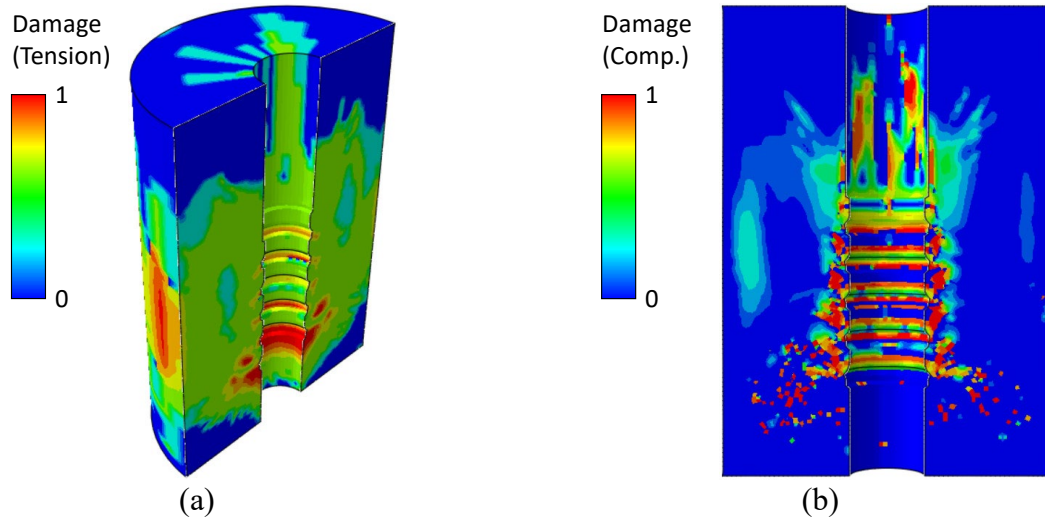
Figure 4.15 Damage patterns at failure: (a) tensile damage (cracking) and (b) compressive damage (crushing) at the section. Note that damage index indicates 0 for undamaged and 1 for fully damaged.

4.5.3 Summary of Comparisons with Tests

The rib-scale FE modeling approach was applied to simulate three different pullout test specimens, which include the specimens with (1) no confinement, (2) spiral reinforcement confinement, and (3) steel tube confinement. Two concrete material models – CDP model and CDPM2 – were separately used as the concrete model for each test specimen to compare their performance. Overall, the CDP model tended to overestimate the bond stress and associated displacement, whereas the CDPM2 yielded simulation results comparable to test data. This is mainly due to the CDPM2's improved capability to simulate concrete hardening and softening response under high volumetric stress states as shown in Figure 3.9.

The developed rib-scale FE models were able to capture different failure modes for different types of specimens: The models predicted concrete splitting failure mechanism for the specimen with no confinement and pullout failure mechanism for the specimen with confinement. The proposed modeling approach revealed limitations in predicting bond behavior when the embedded element technique was employed to model the constraint condition between the reinforcement (truss elements) and concrete (solid elements). The embedded element assumes perfect bond that led to an over-constraint condition between solid and truss elements, and thus provided higher confinement level to the concrete elements inside the spiral reinforcement. The

comparison of the simulation results between the specimens confined with spiral reinforcement and steel tube (Figure 4.11 and Figure 4.14) supports this observation.

There was numerical non-convergence with CDPM2 when the concrete elements experienced severe damage (softening) under high volumetric stress states. Further study associated with numerical stress update is necessary to resolve this problem.

4.6   Conclusions

In this paper, it is proposed a rib-scale FE modeling approach for the simulation of pullout tests of reinforcement embedded in concrete. In the proposed modeling approach, both the concrete and reinforcing bar in the bond-zone are represented with refined solid elements to explicitly capture the deformations of rebar and the surrounding concrete. The surface-to-surface contact model is applied to the interface to allow for the load transfer between two different bodies (concrete and reinforcement). The examples of application illustrate new consideration with respect to the selection of a robust concrete model that can reproduce material response under different multiaxial stress states. Two concrete models – CDP model and CDPM2 – were considered as the study models. These models were compared and discussed from a constitutive modeling point of view and evaluated with three pullout tests. The CDP model and CDPM2 were separately applied to each test specimen to compare their performance against the experimental results.

The FE models were developed within the ABAQUS FE software platform. The CDPM2 was implemented into the software as a user-subroutine material *VUMAT*. The FE simulation results showed that the CDPM2 produced bond stress versus slip results comparable to the measured data in the three specimens tested. The CDP model showed limitations in reproducing the material hardening/softening response, leading to the overestimation of the bond stress. The developed FE models with CDPM2 were able to capture different failure modes for different types of specimens: splitting failure mechanism for the specimen with no confinement and pullout failure mechanism for the specimen with confinement.

Some limitations were found in the proposed modeling approach. First, when spiral reinforcement was modeled with truss elements and the confinement condition was achieved through the *embedded element* technique in ABAQUS, the provided confinement level was found higher than the expected, due to the assumption of *perfect* bond between the embedded rebar truss elements and concrete solid elements. This led to the overestimation of the bond strength. Second,

non-convergence issue within the CDPM2 was observed when the concrete elements were severely damaged in high volumetric stress states. Further work is needed on the numerical stress update to address this problem.

CHAPTER 5.   FINITE ELEMENT SIMULATION OF REINFORCEMENT SPLICE FAILURE IN BEAM STRUCTURES

5.1   Introduction

The lap splice is the most common method of creating a continuous line of reinforcement when the required line of reinforcement exceeds the practical (due to fabrication, transport, or construction) bar length. For construction in the U.S., to achieve the lap splice connection, the overlap length must satisfy the design requirements of ACI Committee 318 (2014). The design criteria for splice strength and length have been developed, primarily, on the basis of experimental test data, which, with advances in concrete and reinforcement materials, creates a continuous need for additional experimental testing. Experimental testing is the most straightforward way to observe external failure mechanisms as well as global behavior of structural members under loading but provided limited information about internal failure mechanism such as concrete cracking and crushing near the reinforcement.

Numerical analysis has been used widely to explore structural behavior beyond the limitations of experimental testing. Most of the previous work addressing simulation of splices is associated with the development of an interface element (or model) that can represent the bond resistance between the reinforcement and surrounding concrete, and its application to member- or structure-level simulation of RC structures (Chen et al., 2011; Erfanian & Alaa, 2019; Murcia-Delso & Shing, 2014, 2015). A few research projects have sought to investigate local bond-zone behavior using rib-scale FE modeling approaches. An example is the work of Lagier et al. (2016), where bond response of lap splices in ultra-high-performance fiber-reinforced concrete (UHPFRC) without confinement was simulated. The model was validated using data from tensile load tests, in which direct tensile load was applied to each of the two spliced bars. The test specimens failed primarily due to concrete crack opening and bar pullout mechanism. In defining a contact model at the concrete-bar interface, friction was considered by introducing a penalty stiffness in the tangential direction. The *hard* contact was enforced on rib front faces to minimize the penetration into the concrete surface. To account for cohesion, some allowable stress criteria in normal and shear directions, represented by bilinear curves, were defined. With these contact properties, the FE model could capture stress distribution in the bar and the associated concrete crack opening at different loading levels. However, the use of the aforementioned contact properties for friction and

adhesion had little influence on the result since the bond response turned out to be dominated by bearing, i.e., interlocking of ribs against concrete. This was further evidenced by the fact that similar results were obtained using a frictionless bond interface. In short, rib-scale model offers promise to capture the dominant effect of bearing on bond behavior and thus to eliminate the effort for specifying the contact properties for modeling bond in RC structure.

5.2   Objectives

This study aims to numerically simulate the bond-zone behavior of spliced longitudinal bars in reinforced concrete beams subjected to monotonically increasing loading via the rib-scale FE modeling approach. The FE model is calibrated and validated using full-scale beam splice tests (Ramirez & Russell, 2008). In the tests, specimens failed in concrete splitting developed at the top surface in the splice bars region due to a combination of prying action of bars and concrete crack opening in tension by bending moment force (details are given later). This failure mechanism is different from what was observed in the tests of Lagier et al. (2016), where only bar splices were subjected to direct tensile loading, leading to concrete crack opening caused by the pulling-out motion of the bars. The main objectives are to provide an FE model that can predict bond response for bar splices in RC beams and to suggest the range of parameters for accurate prediction. The proposed model is characterized by its ability to: (1) distinguish bond behavior characterized by uncoated and epoxy-coated deformed bars including the effect of confinement on bond strength; (2) reproduce global load-displacement relationship; (3) simulate crack initiation and growth patterns; and thus (4) capture the failure mode of the specimens.

The concrete damaged-plasticity (CDP) model is used for concrete material, whereas the CDPM2 is not used since high hydrostatic pressure levels are caused by rib bearing during large sliding motions of reinforcement and given that no such effect is expected in splice tests.

5.3   Experimental Tests Used for Model Development and Calibration

5.3.1   Geometric Information

A series of 18 experimental tests on bar splices in concrete beams were conducted with the purpose of extending the use of the AASHTO LRFD Bridge Design Specifications for splice length of uncoated and epoxy-coated bars to concrete compressive strengths up to 15 ksi (103 MPa)

(Ramirez & Russell, 2008). Figure 5.1 depicts the experimental setup of a typical specimen. The distance between the loading points and supports was 48 in. (1.2 m); the distance between the supports, and thus the constant moment region, was also 48 in. (1.2 m). Three pairs of longitudinal bars (#6, #8, or #11) were spliced at the top of a specimen with the concrete cover equal to the bar diameter within the constant moment region. Splice lengths varied by bar size. The presence of transverse bars in the constant moment region was also considered. In the constant moment region, the top section of a specimen including bar splices and the surrounding concrete was subjected to tensile loading by bending moment force. As the applied loading increased, bar splices tended to rotate upward and beyond a certain point, crack opening occurred on the top surface of the splice region. All the specimens ended in concrete splitting failure, followed by yielding of the spliced bars in the constant moment region, due to a combination of the prying action of the bars and concrete crack opening in tension by bending moment force. Of the 18 specimens tested, the eight specimens shown in Table 5.1 were chosen for FE simulation. The specimen dimensions and variables are given in the same table. The tests with epoxy-coated bars are identified by a test specimen name that starts with "II" instead of "I" with other parameters remaining the same.

Table 5.1 Specimen geometric and material variables

Specimen	Bar size	Cover (in.)	size (B x H) (in.)	Splice length (in.)	Transverse bars	f_c (ksi)	f_y (ksi) Uncoated / coated
I-1 (II-11)	#6	0.75	9 x 18	16	-	15.0	78.3 / 70.3
I-4 (II-15)	#6	0.75	9 x 18	16	#3@8''	15.0	78.3 / 70.3
I-3 (II-12)	#11	1.50	18 x 18	36	-	15.0	66.0 / 74.0
I-6 (II-16)	#11	1.50	18 x 18	36	#4@8''	15.0	66.0 / 74.0

Note: 1 in. = 25.4 mm; 1 ksi = 6.89 MPa; B = beam specimen width; H = beam specimen height; f_c used herein is the designed concrete compressive strength; Specimens starting with a name of "II" in parenthesis are the beams having spliced epoxy-coated bars, while they have the same dimensions to their companions (i.e. "I" specimens).

(a)

(b)
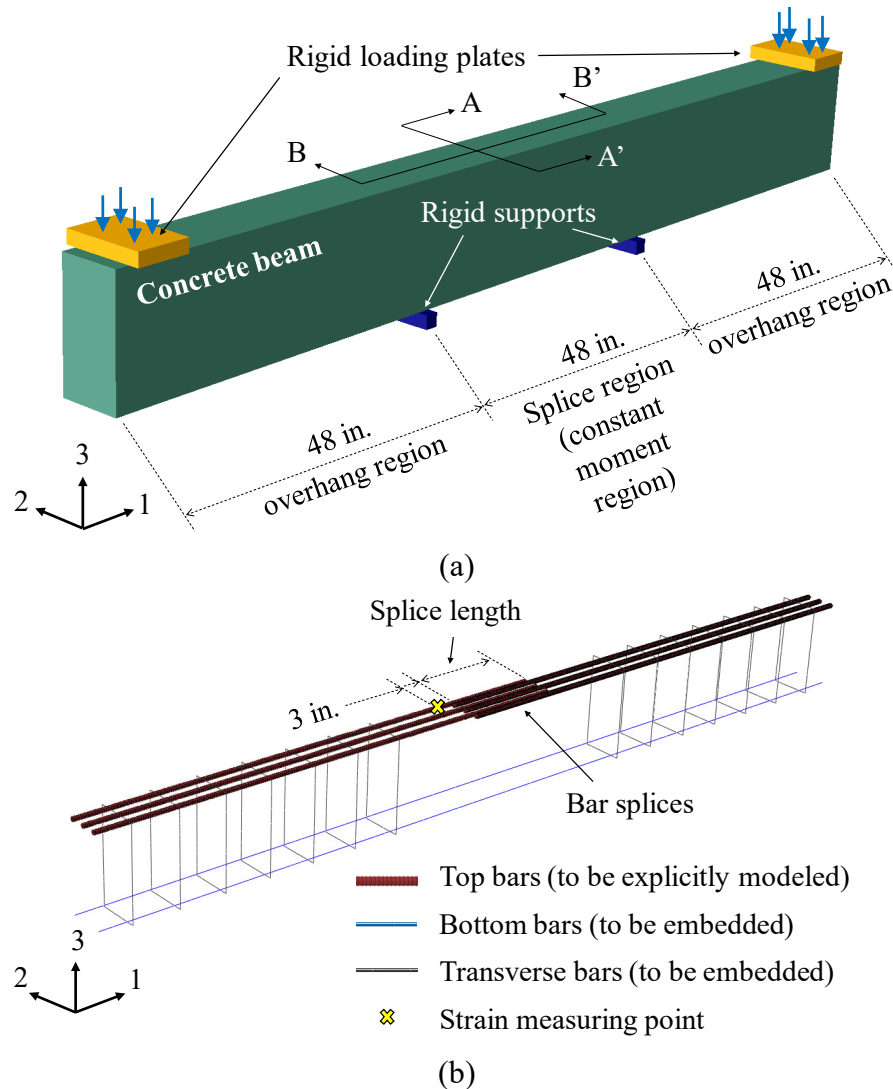
Figure 5.1 Typical beam splice test specimen: (a) Test setup and (b) layout of reinforcing bars (without transverse bars in the splice region)

5.3.2   Material Information

The concrete mix used was designed for a compressive strength of at least 15 ksi (103 MPa). The water-to-cement ratio was 0.20, and the maximum size of the coarse aggregate was 0.5 in. The reinforcing bars used were ASTM A615 Grade 60 steel. Yielding strengths of bars (f_y) obtained from material test varied in each specimen, and they are presented in Table 5.1.

5.4 Rib-Scale FE Modeling of RC Beams with Splices

This section presents the model used in the study, including the modeling approach, constitutive models for concrete and bar, contact model on the concrete-bar interface, and boundary conditions. Aspects of the model that are critical to predicting the response of the RC beams with splices subjected to monotonically increasing tensile loading are identified. The optimal range (or values) of model parameters are investigated and then calibrated in the following section.

5.4.1 FE Model Configurations of Bar Splices, Loading, and Boundary Condition

For modeling purposes, beam specimens can be considered to comprise four types of components: the concrete "beam", sets of transverse reinforcing bars that are spaced at intervals along the length of the beam, two longitudinal bars in the lower part of the beam, and three pairs of spliced longitudinal bars (Figure 5.1 and Table 5.1). Bar splices and the surrounding concrete are explicitly represented using the rib-scale modeling approach, as they are the region of interest in the simulations. The remaining reinforcing bars, such as longitudinal bars at the bottom and transverse bars, are not geometrically represented but embedded in the beam. In the test, R_r was 0.091 and 0.135 for the #6 and #11 bars, respectively. In the FE model, R_r of 0.1 is used in both bars for simplicity. Also, because the rib geometry information of bars (i.e., a_r, b_r, h_r, and d_b) is not reported in the literature (Ramirez & Russell, 2008), they are determined to result in R_r of 0.1 by means of the empirical formulas, presented earlier in Eq. (2.1) and re-introduced in Table 5.2. The effect of changes in rib geometry while maintaining the same R_r is discussed later.

In the FE model, the two beam supports were represented by rigid bearings, as shown in Figure 5.1, where only the vertical displacement U_3 was constrained. The rigid loading plates were restrained in all transitional and rotational directions except U_3, allowing for applying the load in that direction.

5.4.2 FE Discretization

Figure 5.2 shows the finite element mesh for Specimen I-4. Two different sections in Figure 5.1 are shown to illustrate the elements' regularity and arrangement. The concrete beam was meshed using the solid element C3D8R, an 8-node brick element with reduced integration to avoid shear locking. Three pairs of spliced bars at the top were also explicitly modeled with the same element. Both transverse bars and bottom bars were modeled by the truss element T3D2 and embedded in

the concrete beam. Because the rib-scale modeling approach requires a high level of mesh refinement, the element length at the interface region in Specimen I-4, for instance, was refined with as small as 0.3 in. A total of 1,862,024 elements consisted of that specimen. The typical mesh element shape was a cuboid with longer edges in the U_2 and U_3 directions (Section A-A' in Figure 5.2) than the ones in the U_1 direction (Section B-B' in Figure 5.2). This was unavoidable due to the representation of ribs, which have many bumps when a bar is cut in the U_1 direction as shown in Figure 2.1, making that direction's edges shorter. Otherwise, much more elements would be needed to maintain a relatively regular element shape. No numerical errors were found due to these elements' rectangularity during the analysis.
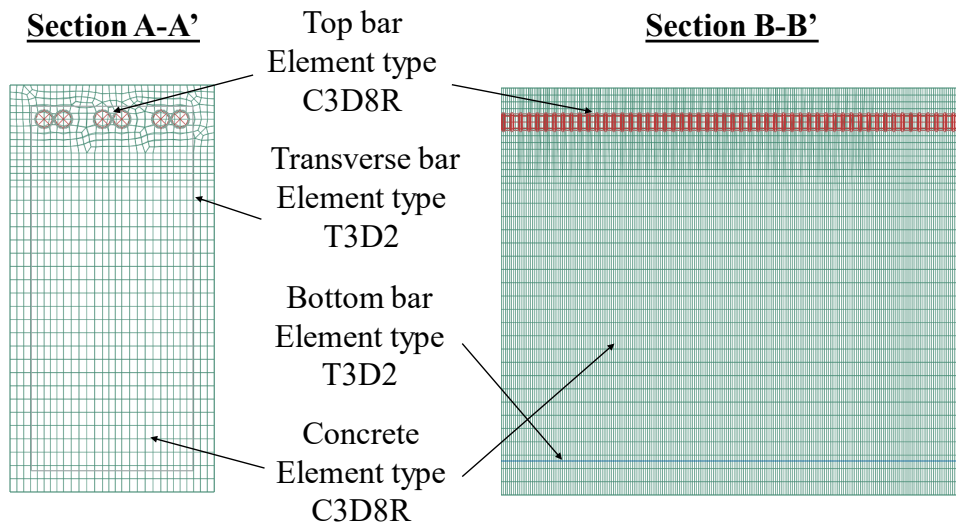
Figure 5.2 Finite element type and transparent view of mesh scheme at different sections of Specimen I-4

Table 5.2 Bar splice geometry information

Specimen	Bar size	d_b (in.)	a_r (in.)	b_r (in.)	h_r (in.)	s_r (in.)	R_r
I-1 (II-11)	#6	0.75	0.075	0.15	0.0375	0.375	0.1
I-4 (II-15)	#6	0.75	0.075	0.15	0.0375	0.375	0.1
I-3 (II-12)	#11	1.41	0.141	0.282	0.0705	0.705	0.1
I-6 (II-16)	#11	1.41	0.141	0.282	0.0705	0.705	0.1
Note: 1 in. = 25.4 mm; $a_r = 0.1d_b$; $b_r = 0.2d_b$; $h_r = 0.05d_b$; and $s_r = 0.5d_b$; R_r was calculated using Eq. (2.1).							

5.4.3   Concrete Model

Since high hydrostatic pressure levels are caused by rib bearing during large sliding motions of reinforcement and given that no such effect is expected in splice tests, the CDP model is used in this study. In the CDP model, concrete hardening and softening, damage, and yield criterion are determined by several key plasticity parameters: dilation angle (ψ), eccentricity (ϵ), ratio of biaxial compressive strength to uniaxial compressive strength (f_{bc}/f_c), and ratio of the second stress invariant on the tensile meridian to that on the compressive meridian at initial yield (K_c). These values were chosen to be as 31°, 0.1, 1.16, and 0.75, respectively, for all analyses. The ψ of 31° was found to be appropriate for simulating the concrete dilatancy (Genikomsou & Polak, 2015; Huang et al., 2015) and justification for the use of K_c of 0.75 is presented later. The other values, e of 0.1 and f_{bc}/f_c of 1.16, are the default values in ABAQUS software.

The model treats concrete compressive and tensile behavior separately. It defines concrete response under tensile loading by the concrete yield stress and corresponding strain, displacement, or fracture energy. Initially, concrete tensile strength (f_t), was defined using the ACI 318 Code (ACI 318 Committee, 2014) equation for concrete modulus of rupture, f_t = 7.5 f_c with f_c in psi. This value was later adjusted to provide a better fit to the experimental data. At the onset of tensile cracking, both strain and displacement corresponding to concrete yield stress may differ depending on the concrete element size. Therefore, the fracture energy (G_f), which ensures mesh-objective simulation of the response, was used throughout all the analyses presented in this paper. Martin et al. (2007) found from the material test that G_f for normal strength concrete ranges between 0.48 and 0.72 lb/in. (0.084-0.13 N/mm), as shown in Table 5.3. When experimental fracture energy is not available, the empirical equation proposed by Bažant & Becq-Giraudon (2002) and then reconstructed by Martin et al. (2007) can be used to obtain the estimated G_f, as follows:

$$G_f = \begin{cases} 0.0143\alpha_o \left(\dfrac{f_c'}{8.41}\right)^{0.40} \left(1+\dfrac{A_{max}}{0.0763}\right)^{0.43} \left(\dfrac{w}{c}\right)^{-0.18} & \text{in } lb/in. \\[3mm] 0.0025\alpha_o \left(\dfrac{f_c'}{0.058}\right)^{0.40} \left(1+\dfrac{A_{max}}{1.94}\right)^{0.43} \left(\dfrac{w}{c}\right)^{-0.18} & \text{in } N/mm \end{cases} \tag{5.1}$$

where α_o is an aggregate shape factor (i.e., 1 for rounded aggregate or 1.12 for angular aggregate); f_c is the concrete compressive strength (psi or MPa); A_{max} is the maximum aggregate size (in. or mm); w/c is the concrete water-cement ratio.

It should be noted that the above equation was proposed based on test data covering various values of f_c with the strength up to 19 ksi (131MPa). Given all the specimens considered have f_c of 15 ksi (103MPa), A_{max} of 0.5 in., and w/c of 0.2 in common, G_f was estimated to be 1.0 lb/in. (0.18 N/mm). This value is much higher than what has been observed for normal strength concrete materials, shown in Table 5.3. Nevertheless, higher G_f is consistent with Bažant & Becq-Giraudon (2002) who note that G_f for high-strength concrete has been observed to be significantly larger than for normal-strength concrete.

Concrete material response under compressive loading is typically defined using a set of stress-strain data, obtained experimentally or through available models. The experimental test reports only concrete compressive strength with respect to curing age. Hence, this study utilized the stress-strain model proposed by Yang et al. (2014), to simulate compressive response (Figure 5.3). Post-peak behavior of the model is then adjusted to give a linear softening branch such that a stress of 20% f_c is reached to the prescribed residual strain (ε_{20}). The value of ε_{20} is determined based on the concrete crushing energy concept because post-peak response in FE model is mesh size dependent. In general form, concrete crushing energy (G_{fc}) is defined as given below (Coleman & Spacone, 2001; Jansen & Shah, 1997).

$$G_{fc} = L_e \int_{\varepsilon_0}^{\varepsilon_{20}} \sigma d\varepsilon$$

$$\text{or} \tag{5.2}$$

$$\frac{G_{fc}}{L_e} = \int_{\varepsilon_0}^{\varepsilon_{20}} \sigma d\varepsilon$$

where L_e is the characteristic length of finite element mesh in the crack band; σ and ε are stress and strain in concrete compressive stress-strain curve, respectively; ε_0 and ε_{20} are the peak strain and residual strain at 20% f_c in post-peak response, respectively.

The integral part of the above equation represents the area under post-peak behavior, shown with the shaded area in Figure 5.3. The typical value of G_{fc} for normal and high strength concrete has been experimentally observed to be 114-171 lb/in. (20-30 N/mm) [34], as presented in Table 5.3. Given experimentally-obtained G_{fc} and user-defined L_e for the FE model, ε_{20} can be expressed as follows (Coleman & Spacone, 2001).

$$\varepsilon_{20} = \frac{G_{fc}}{0.6f_c L_e} - \frac{0.8f_c}{E} + \varepsilon_0 \qquad (5.3)$$

where E is the elastic modulus of the concrete material.

In all the analyses carried out in this study, f_c and L_e are 15 ksi and 0.3 in., respectively. Assuming G_{fc} to be as 133 lb/in. (23 N/mm), ε_{20} is estimated as 0.05 by the above equation. The consequent concrete stress-strain response under compressive loading is provided in Figure 5.4(a).

Table 5.3 Values (or ranges) of parameters found in the literature

| Material	Parameter	Value	Note	Literature
Concrete	G_f	0.48-0.72 lb/in. (0.084-0.013 N/mm)	Normal strength concrete	Martin et al. (2007)
	G_{fc}	114-171 lb/in. (20 - 30 N/mm)	Normal and high strength concrete	Jansen and Shah (1997)
	f_t	$7.5\sqrt{f_c}$ for psi units		ACI Committee 318 (2014)
		$4.0\sqrt{f_c}$ for psi units ($0.33\sqrt{f_c}$ for MPA units)		fib Bulletin No. 45 (2008)
Concrete-bar interface	μ	0.56	Uncoated	Idun and Darwin (1999)
		0.49	Coated	
	R_r	0.05 to 0.20		Eligehausen et al. (1983); Metelli & Plizzari (2014); Murcia-Delso et al. (2013); Tholen & Darwin (1996); Zuo & Darwin (1998)
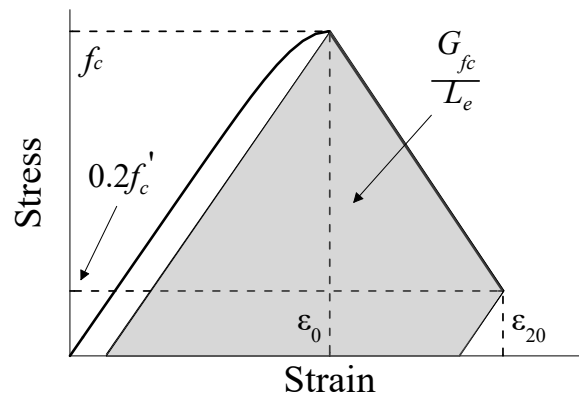
Figure 5.3 Concrete compressive stress-strain model by Yang et al. (2014)
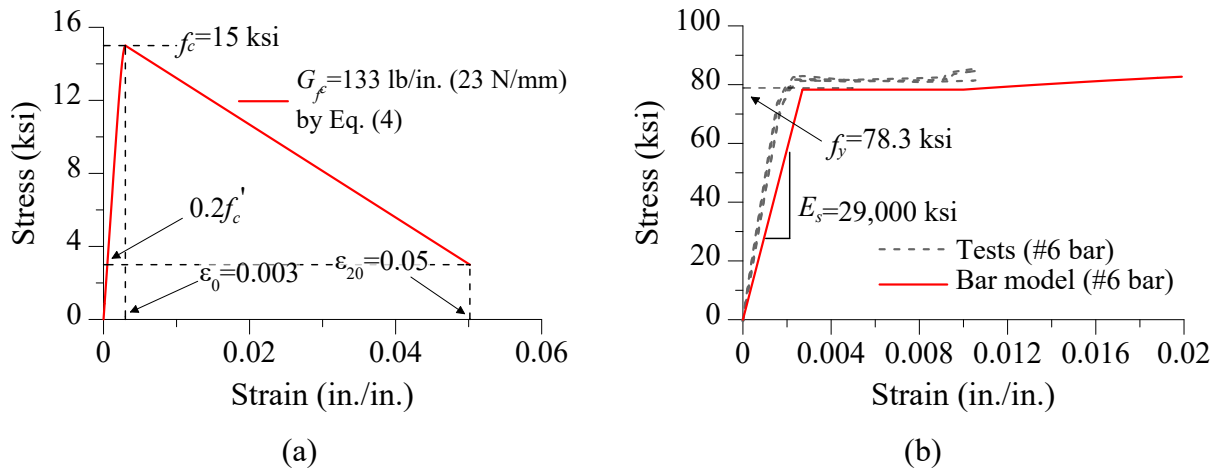
Figure 5.4 Material models used for FE model development: (a) concrete stress-strain response in compression and (b) steel stress-strain response in tension for # 6 bar in Specimen I-4.

5.4.4 Steel Model for Reinforcement

Figure 5.4(b) shows the stress versus strain curves measured from tests of samples of the #6 bars. From these curves, the elastic modulus of the steel bar (E_s), corresponding to the slope of the curves, was roughly estimated as 40,000 ksi (276 GPa), which is much beyond the typical E_s of steel, 29,000 ksi (200 GPa). This is assumed to arise from measuring strain over a short gauge length, with the area reduced by the filling needed to attach the gauge to the bar. In addition, the test data has provided only the measured stress-strain response up to the strain of 0.01, which is way before the typical ultimate strain (e.g., 0.1). It is important to represent the inelastic response of the bar because, in the tests, bar yielding occurred before the peak load. For these reasons, a bar model was generated using the model proposed by Raynor et al. (2002) with the measured yield strength of the bar (f_y) presented in Table 5.1 and typical E_s. The stress-strain response for #6 bar generated by the model is shown in Figure 5.4(b). It must be noted that for the model, the ultimate strength, strain at the onset of hardening, and ultimate (peak) strain were assumed to be 90 ksi (620 MPa), 0.01, and 0.12, respectively.

5.4.5 Contact Model

The contact model was used to define contact interaction properties at the concrete-steel interface. It includes the tangential behavior for friction and normal behavior for load transfer by the wedging of ribs into concrete key as well as cohesive behavior for chemical adhesion between two materials.

The general contact (surface-to-surface contact formulation) in ABAQUS enables such contact interactions in a simple way that ensures the contact conditions described above are enforced efficiently (Simulia, 2014). As for the tangential behavior, the friction coefficient that reflects the roughness of the materials was used for analysis. Idun & Darwin (1999) have found from tests that the uncoated and epoxy-coated bars have the friction coefficients of 0.561 and 0.491, respectively, as presented in Table 5.3. These coefficients were used as the base values for analysis and were adjusted afterward to match the experimental data of the specimens. The normal behavior describing the contact pressure-overclosure relationship was represented using the default *hard* contact in ABAQUS. The *hard* contact enforces infinite stiffness with overclosure when two surfaces are in contact and pressed against each other, resulting in no penetration between the two interfacial surfaces. The use of *hard* contact can be justified in that the tests failed in part due to the force rotating upward of the bar splices that pressed concrete cover to open. With this definition, the concrete cover moved upward as much as the bars pushed upward. The cohesive behavior that accounts for chemical adhesion was ignored, as bond is expected to be dominated by bearing and friction. Indeed, it has been experimentally and numerically observed that for deformed bars, adhesion accounts for an inconsequential part of bond resistance, and only before slip is initiated (Abrams, 1913; Lagier et al., 2016; Salem & Maekawa, 2004).

5.5   FE Modeling Calibration and Material Parameter Investigation

5.5.1   Modeling Calibration

Table 5.3 lists values, ranges of values and equations defining concrete material properties, reinforcing steel geometric properties and concrete-steel interface parameters that could be expected to determine the bond-zone and, as a result, beam specimen simulated response. A series of analyses were conducted to investigate the sensitivity of simulated response to variation in these parameters and establish appropriate values for use in simulating bond-zone behavior. Specimen I-4, constructed using uncoated reinforcing bars and with confining reinforcement, was selected for this study. Table 5.4 lists values of these critical parameters used in the analyses.

Among the parameters, both the tensile strength f_t and friction coefficient μ were expected to have a significant impact on simulated response and were simultaneously examined as the study variables. This choice arose from the assumption that G_f obtained from Eq. (5.1) provides a

reasonable estimate and G_{fc} has minimal impact on response because concrete crushing failure was not found to be controlling in the laboratory test. Figure 5.5 shows the applied load versus displacement at the tip of the overhang region of the beam obtained for various values of f_t and μ, compared with experimental data. The applied load represents the average of the two values from the actuators represented by rigid plates. Laboratory data show that as soon as the peak load was attained, the specimen started to exhibit little hardening (flattening) until it failed. When the analysis was performed with ACI-suggested $f_t=7.5\sqrt{f_c}$ and μ=0.5 (approximate value for epoxy-coated bar), the simulation showed consistently high stiffness gradients and a load capacity well in excess of that measured in the laboratory. Post-peak flattening and softening response was not captured. These aspects of the simulated response history were attributed to an overestimation of f_t in the analysis. Drops in the load-displacement history that are followed by strength recovery result from concrete cracking, which produces rapid strength loss, followed by increasing deformation in the vicinity of the crack, which produces increasing steel stress and specimen strength gain. Another simulation was conducted using the fib-suggested equation, $f_t=0.33\sqrt{f_c}$ for MPa units (fib Bulletin No. 45, 2008), which corresponds to $4.0\sqrt{f_c}$ for psi units. Using this value of f_t, the FE analysis yielded a slightly lower load-displacement curve than the one with $7.5\sqrt{f_c}$, but still did not show any notable post-peak response within the expected range of displacement.

Given that the uncertainty in predicting f_t in high-strength concrete also impacts μ, the analysis was repeated with $4.0\sqrt{f_c}$ and a reduced μ of 0.1. The reduction in μ led to a distinct descending branch, initiated at the displacement corresponding to the peak load observed in the test. When f_t was further reduced to $3.0\sqrt{f_c}$ with maintaining μ=0.1, the simulated result almost matched the test, especially when it comes to the peak load/displacement and post-peak response. Further smaller value of f_t resulted in the lower peak load only, which is not presented in Figure 5.5. Often, overestimation of the stiffness is attributed to shrinkage cracking that occurs in laboratory, which was not included in simulation. In addition, to achieve the higher strength concrete, silica fume was added to the mix. This type of mix is associated with significant shrinkage cracking, leading to a reduction in stiffness at early loading stage. The use of the multiplier 3.0 can be attributed to the fact that a wide variation in tensile strength of concrete is expected and has been experimentally observed in concrete material tests (fib Bulletin No. 45, 2008; Raphael, 1984). It may also arise from different sizes and configurations between material

test specimens and beam specimens. Besides, overestimation of concrete tensile softening behavior is a well-known limitation of the CDP model (Lee & Fenves, 1998). The reduction in f_t could compensate for this shortcoming. A similar approach to reducing tensile capacity was applied to the modeling of lap splice tests in ultra-high-performance fiber-reinforced concrete (UHPFRC) (Lagier et al., 2016). In that model, measured tensile stress-strain curve of UHPFRC has reduced by almost a half to simulate experimental response. Significant reductions in μ values when compared to the experimental ones may have resulted from inaccurate force transfer at the concrete-steel interface represented with rib geometry, generated by the general contact model (surface-to-surface contact formulation). The evaluation of this contact model has not been thoroughly discussed in this study.

Now, based on the observation made above, Specimen II-11, which corresponds to the opposite case of Specimen I-4 (i.e., epoxy-coated and unconfined specimen), was simulated with the calibrated values of f_t and μ, that are $3.0\sqrt{f_c}$ and 0.1, respectively (Figure 5.6). The simulation result showed a much higher peak load and the corresponding displacement when compared to test data. Another analysis was carried out with μ of 0, as it is expected that μ for coated bar would smaller than that for uncoated bar. Then, they showed good agreement in both load and displacement around the peak. This implies that a coated bar is very sensitive to μ as expected and furthermore, μ needs to be reduced to zero, or close to zero, to numerically provide the best fit to the test and simulate the presence of coating.

Table 5.4 Range of values of the parameters investigated and values recommended for use

| Material	Parameter	Range of value investigated	Recommended value	Unit	Ref.
Concrete	G_f	0.6, 1.02	1.02	(lb/in.)	Eq. (5.1) Figure 5.7
	G_{fc}	133, 171	-	(lb/in.)	Figure 5.8
	f_t	$7.5\sqrt{f_c}$, $4.0\sqrt{f_c}$, $3.0\sqrt{f_c}$	$3.0\sqrt{f_c}$ (=367.4 psi)	(f_c in psi)	Figure 5.5 Figure 5.6
	ψ	20, 31, 40	31	(°)	Figure 5.10
Concrete-bar interface	μ (uncoated)	0, 0.1, 0.5	0.1	-	Figure 5.5
	μ (epoxy-coated)	0, 0.1	0	-	Figure 5.6
	R_r	See Table 5.5		-	Figure 5.9
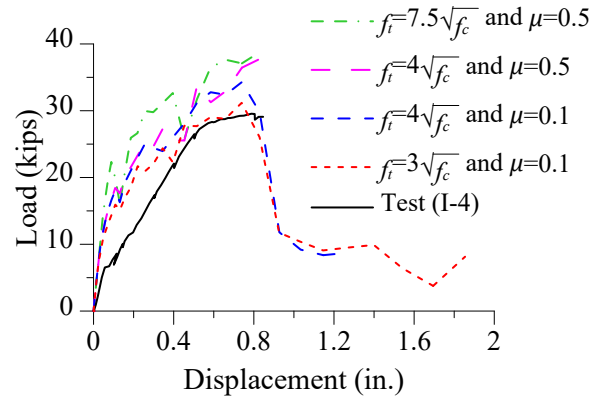
Figure 5.5 Comparison between results simulated with different combinations of f_t and μ and measured in Specimen I-4
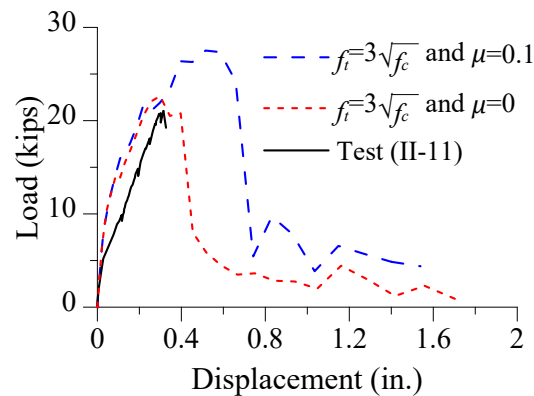

Figure 5.6 Comparison between results simulated with different combinations of f_t and μ and measured in Specimen II-11

5.5.2   Further Investigation on Material and Geometrical Parameters

Another series of analyses were conducted using the recommended values of f_t and μ determined from the above analyses, listed in Table 5.4. In these analyses, optimal approaches for defining G_f, G_{fc}, and rib geometry were assessed. Additionally, two plasticity parameters associated with the CDP model, ψ and K, were examined because ψ has shown a considerable influence on inelastic response of the material (Genikomsou & Polak, 2015) and K determines yield surface shape of the material. The effects of the other parameters in the CDP model (e and f_{bc}/f_c), are not addressed, as FE analyses were carried out with their default values in ABAQUS, which relatively have been well defined. An investigation of the parameters was conducted using the FE model calibrated above for Specimen I-4.

- Concrete fracture energy (G_f): simulations were conducted to evaluate the value of G_f for use in high strength concrete analyses. The G_f value obtained from Eq. (5.1), 1.0 lb/in. (0.18 N/mm), was compared with G_f for normal strength concrete, 0.6 lb/in. (0.1 N/mm),

in Figure 5.7. The latter G_f is the one falling within the G_f range presented in Table 5.3. The simulation response indicates that Eq. (5.1) provides a reasonable estimate of G_f for high strength concrete material and the G_f for normal strength concrete has lower fracture energy capacity as addressed in the literature (Bažant & Becq-Giraudon, 2002).

- Concrete crushing energy (G_{fc}): two different G_{fc} that fall within the typical G_{fc} range (Table 5.3) were considered to examine its effect. One was the G_{fc} of 133 lb/in. (23 N/mm), which belongs to the typical range of G_{fc}, and the other was 171 lb/in. (30 N/mm), which is the upper-bound value of the typical range of G_{fc}. The ε_{20} values, corresponding to these two G_{fc}, were computed by the Eq. (5.3) as 0.05 and 0.064, respectively. Figure 5.8 shows the simulation response obtained for these two G_{fc} values, along with the test data. It is seen that the difference in G_{fc} does not have significant impact on simulated response. This observation indicates that the G_{fc} range found in the test provides quite consistent simulation response of the considered specimen. All the following FE analyses were performed with G_{fc}=133 lb/in.

- Rib geometry: the impact of rib geometry on response was examined by changing the rib configuration but maintaining the R_r value of 0.1. Table 5.5 presents the rib geometry combinations considered for investigation. The rib configuration for R1 was taken from Specimen I-4. The other two experimental groups (R2 and R3) were made to have different geometry configuration with the same R_r value used in R1. It should be noted that h_r and s_r increase with the ascending order of experimental groups: h_r and s_r for R1 < h_r and s_r for R2 < h_r and s_r for R3. Figure 5.9 compares the simulation response for R1, R2, and R3 with the test data. From this figure, it can be observed that larger h_r and s_r lead to smaller peak load and displacement. It is very important to note that although the same R_r is maintained, different rib configurations have a significant impact on bond response and a physics-based rib-scale modeling approach can capture its effect.

- Dilation angle (ψ): the impact of ψ on simulated response was investigated by conducting analyses using ψ values of 20°, 31°, and 40° (see Figure 5.10). As observed in other simulations (Genikomsou & Polak, 2015; Huang et al., 2015), ψ of 31° provided a good agreement with test data and was chosen for subsequent simulations. It should be noted that concrete material response that undergoes nonlinearity is very sensitive to ψ.

- Second deviatoric stress invariant ratio (K_c): the parameter K_c is an influencing parameter that determines the yield surface shape for a stress state in the CDP model. It must meet the condition: $0.5 < K_c \leq 1.0$ (Lubliner et al., 1989; Simulia, 2014). The default value is 0.67 (=2/3) (Simulia, 2014) and in general, has been adopted for simulation of normal-strength concrete. However, it has been observed from the experimental evidence (Ansari & Li, 1998) that compressive meridian for high-strength concrete has lower slope with increasing hydrostatic stress equivalent than that for normal strength concrete, resulting in a higher value of K_c. Thus, the impact of K_c was assessed. A comparison of simulation results according to different K_c values, 0.67, 0.75, and 1.0, is presented in Figure 5.11. All simulations resulted in the similar peak load but K_c of 1.0 showed the highest load levels before the peak in comparison with other K_c values. Between K_c of 0.67 and 0.75, similar load-displacement curves were observed until exhibiting flattening of the curves. Then the K_c value of 0.67 showed a slightly larger response to both load and displacement. For accuracy, all the following models took the K_c of 0.75.
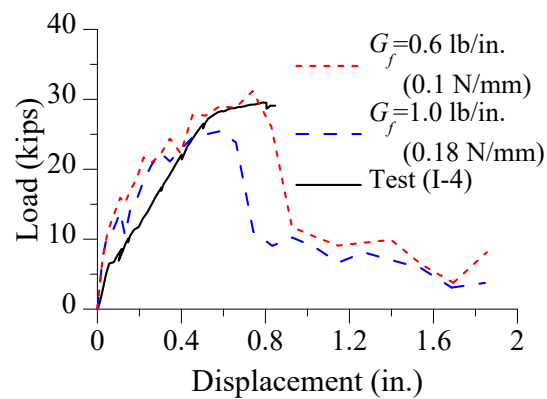

Figure 5.7 Load vs. displacement response of Specimen I-4 for different G_f
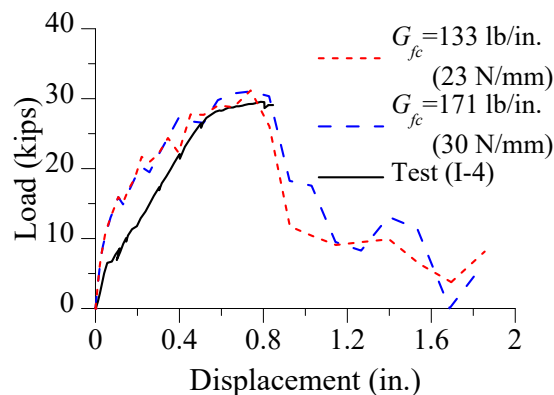
Figure 5.8 Load vs. displacement response of Specimen I-4 for different G_{fc}
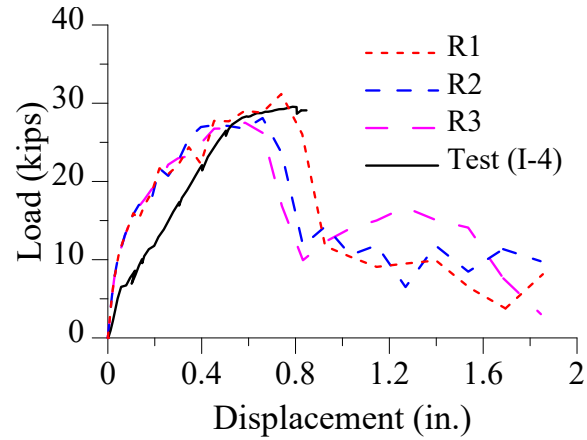
Figure 5.9 Load vs. displacement response of Specimen I-4 for different rib geometry combinations
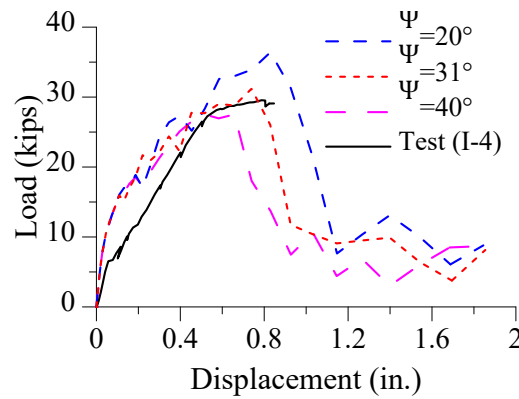
Figure 5.10 Load vs. displacement response of Specimen I-4 for different ψ
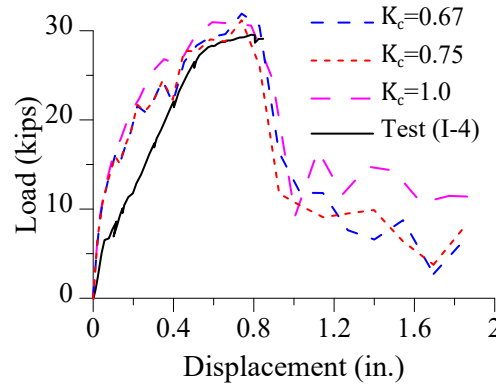
Figure 5.11 Load vs. displacement response of Specimen I-4 for different K_c

Table 5.5 Rib geometry combinations considered for investigation

	Bar size	d_b (in.)	a_r (in.)	b_r (in.)	h_r (in.)	s_r (in.)	R_r (Eq. (2.1))	Note
R1	#6	0.75	0.075	0.15	0.0375	0.375	0.1	Specimen I-4
R2	#6	0.75	0.075	0.155	0.04	0.4	0.1	
R3	#6	0.75	0.075	0.175	0.05	0.5	0.1	

5.5.3 Recommended Values of Identified Parameters

Table 5.4 provides the summary of material parameter values recommended for a rib-scale FE model of bar splices in concrete beam, developed with ABAQUS software. Of the parameters listed in the table, both f_t and μ need to be calibrated based on the comparisons between simulated and tested results. The μ value plays a critical role in distinguishing the behavior between epoxy-coated and uncoated bars. On the other hands, it is demonstrated that G_f and G_{fc} for concrete material have been well defined in the literature: the empirical equation for G_f, Eq. (5.1), and measured G_{fc} range work well for predicting the experimental results. Plasticity parameters in the CDP model, ψ and K_c, were assessed. Particularly, the variations in ψ value make significant changes in post-peak behavior of the model. The ψ of 31° and K_c of 0.75 provide simulation results comparable to the test data considered in this study. A series of analyses on the rib configuration indicates the importance of representing the rib configurations as they are in the actual deformed bar because a rib-scale FE model can capture the impact of rib geometry.

5.6 FE Simulation Results

5.6.1 Uncoated Bars

Based on the results of the parameter studies described above, the response of test specimens with uncoated bars was simulated using the recommend model parameters listed in Table 5.4 and measured material parameters listed in Table 5.1. Figure 5.12 shows the simulated load versus displacement curves, along with their corresponding test results. In the tests, load-displacement responses after attaining their peak load displayed sudden drops due to strength loss resulted from a splitting-type failure in the spliced region. Since the testing was conducted under load control, the post-peak behavior could not be properly measured. Thus, only responses up to the peak load were given in the figures. The simulated responses are in good agreement with the test data, including the reproduction of peak load and strength loss. It is noteworthy that the proposed FE modeling approach incorporated the presence of the confinement and reflected its effect on the analysis response. In both tests and FE simulations, Specimen I-4 and I-6, confined with transverse bars in the spliced region, displayed a brief plateau phase after the initial linear phase, corresponding to yielding in the bar, then reaching an inflection point peak load, after which concrete splitting developed in the splice region. Such plateau was not observed in their companion,

Specimen I-1 and Specimen I-3, which had no confinement. Peak load (P) and the corresponding displacement (D) differences between the test and the FE analysis were evaluated by means of P_{FEA}/P_{Test} and D_{FEA}/D_{Test}, respectively. The results are listed in Table 5.6.

In Figure 5.13, the applied load versus bar strain response obtained in the spliced region of Specimen I-6 is shown. The measuring point is marked in Figure 5.1. Although the measured strain was an infinitesimal quantity that is difficult to predict, the FE model could simulate the tested load versus strain relationship within a reasonable deviation.

Crack initiation and development simulated for Specimen I-4 (confined case) was demonstrated with the one observed in the test. In the specimen, crack openings aligned with the U_2 direction were sparsely initiated at the top of the beam under 10 kip (44 kN). As loading increased, more cracks were evenly developed throughout the top surface. Particularly, in Figure 5.14, a comparison of crack distribution between the simulation and test is shown for the applied load of 17 kip (76 kN) and peak load of 30 kip (207 kN), where the gray-zone illustrates crack occurring. It is seen that the concrete splitting crack development pattern observed in the test was reasonably captured through the proposed modeling methodology. Such ability of the proposed modeling methodology is also confirmed through the comparison for the unconfined specimen (I-3), presented in Figure 5.15. Figure 5.16 shows maximum principal stress fields of Specimen I-4, taken in a longitudinal section across the center of one of the spliced bars, under two different applied loads, 17 kip (76 kN) and 30 kip (207 kN). It is observed from the figure that most of the top concrete part in the splice region exceeded the predefined concrete tensile strength, f_t of 367.4 psi for this case, under the load of 17 kip, followed by failure transition to the bottom of concrete beam at the peak load.

Table 5.6 Test and FEA results

| Specimen	Test		FEA		$\frac{P_{FEA}}{P_{Test}}$ (%)	$\frac{D_{FEA}}{D_{Test}}$ (%)
	P_{Test} (kip)	D_{Test} (in.)	P_{FEA} (kip)	D_{FEA} (in.)		
I-1	28.2	0.51	27.5	0.52	98.5	102.0
I-4	29.6	0.79	31.2	0.74	105.4	93.7
I-3	88.6	0.65	87.0	0.51	98.2	78.5
I-6	96.4	0.80	102.6	0.82	106.4	102.5
II-11	21.0	0.31	22.6	0.30	107.6	96.8
II-15	28.8	0.60	24.4	0.52	84.7	86.7
II-12	64.5	0.39	68.9	0.24	106.8	61.5
II-16	92.0	0.66	80.8	0.45	87.8	68.2
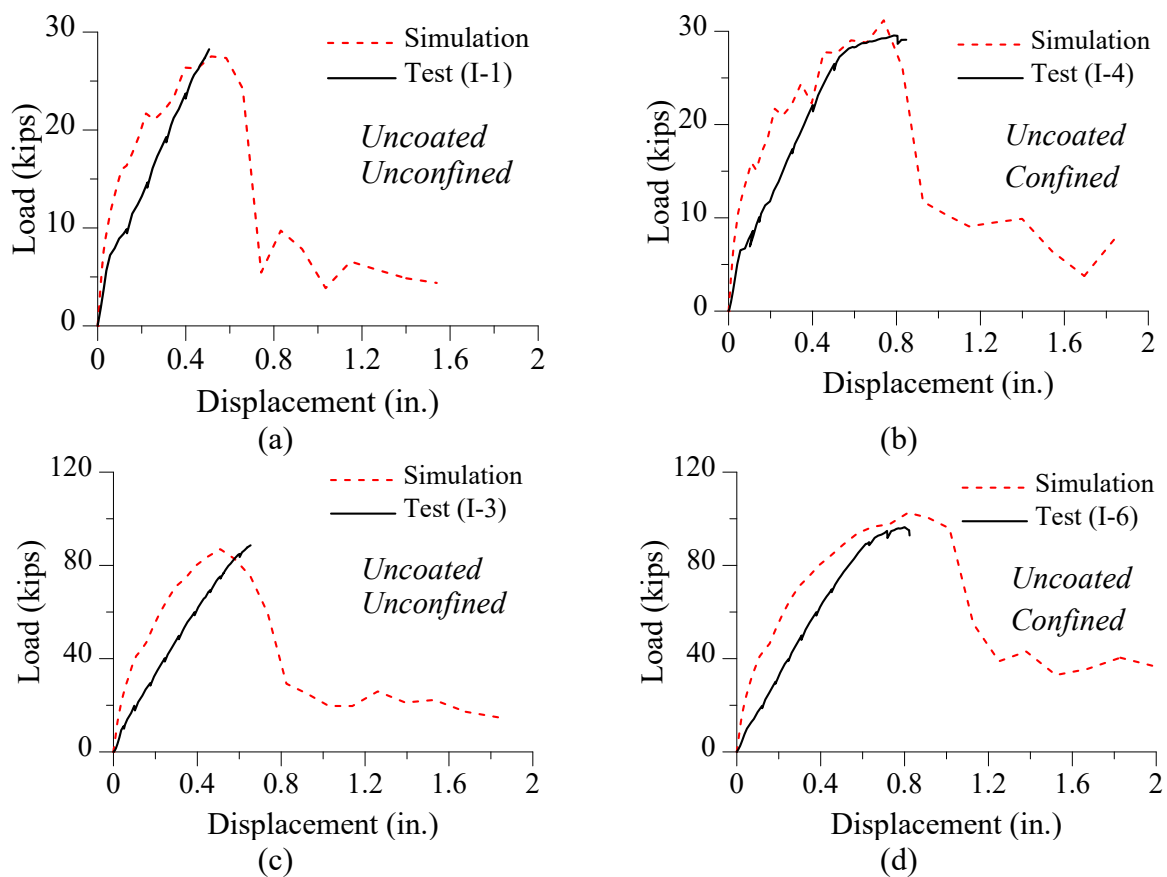
Figure 5.12 Load vs. displacement response simulated and measured in (a) Specimen I-1; (b) Specimen I-4; (c) Specimen I-3; and (d) Specimen I-6
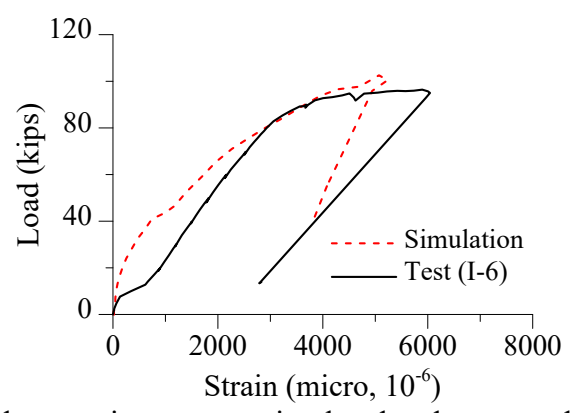

Figure 5.13 Load vs. strain response simulated and measured in Specimen I-6

(a)

(b)
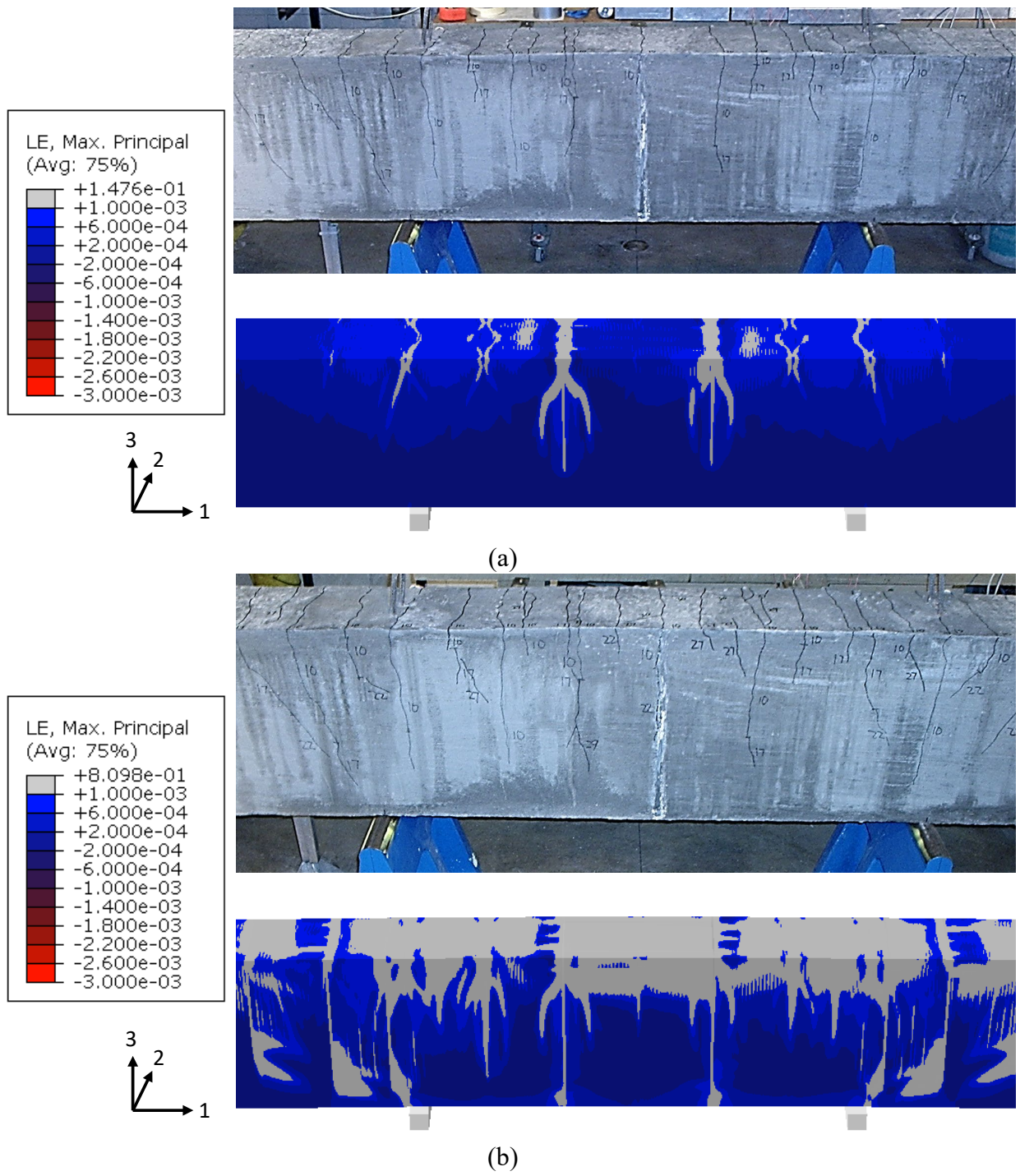
Figure 5.14 Failure simulation of (confined) Specimen I-4 (a) at 17 kip (76 kN); (b) at the peak load of 30 kip (133 kN)

(a)

(b)
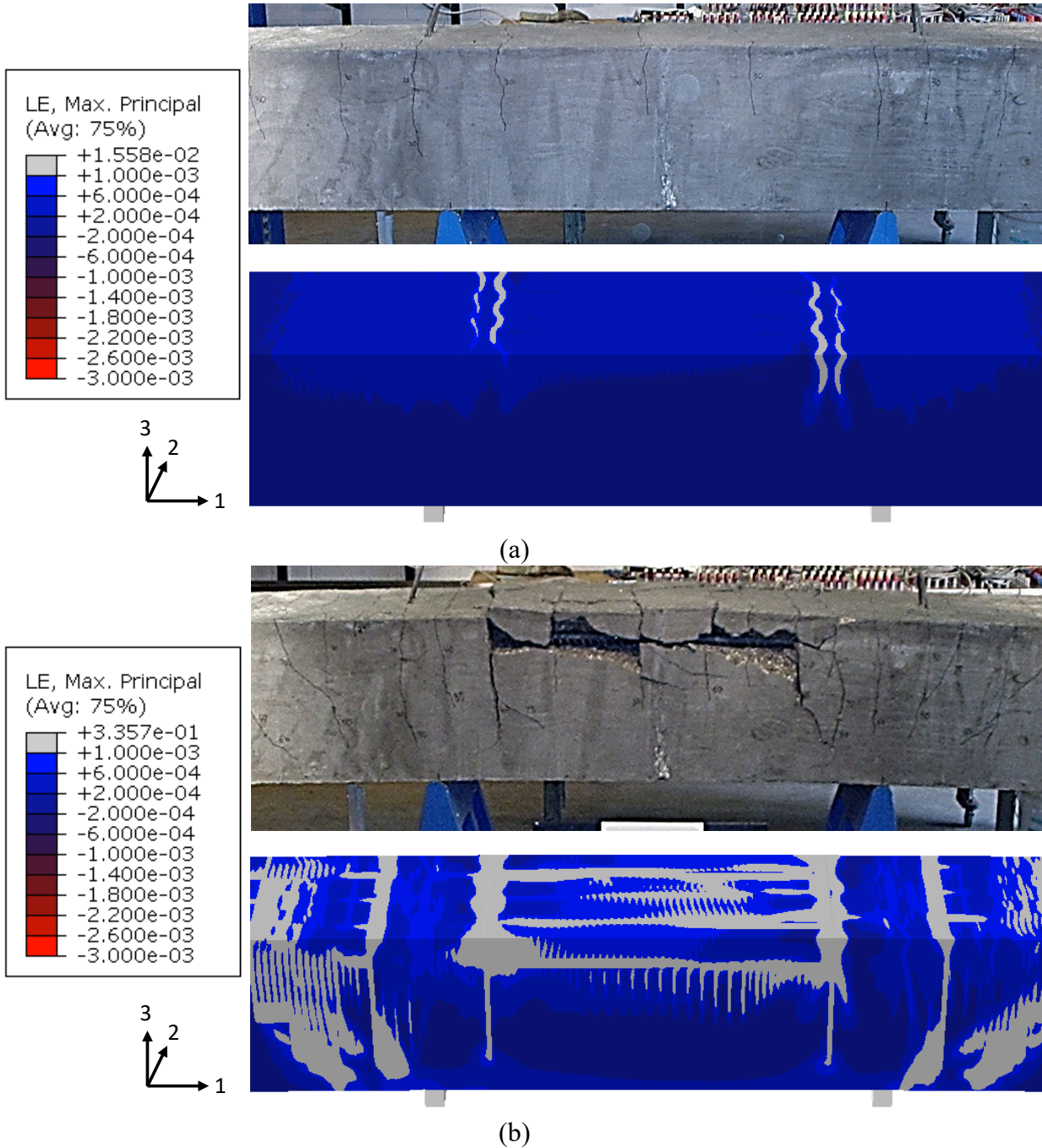
Figure 5.15 Failure simulation of (unconfined) Specimen I-3 (a) at 30 kip (133 kN); (b) at the peak load of 87 kip (387 kN)

(a)

(b)
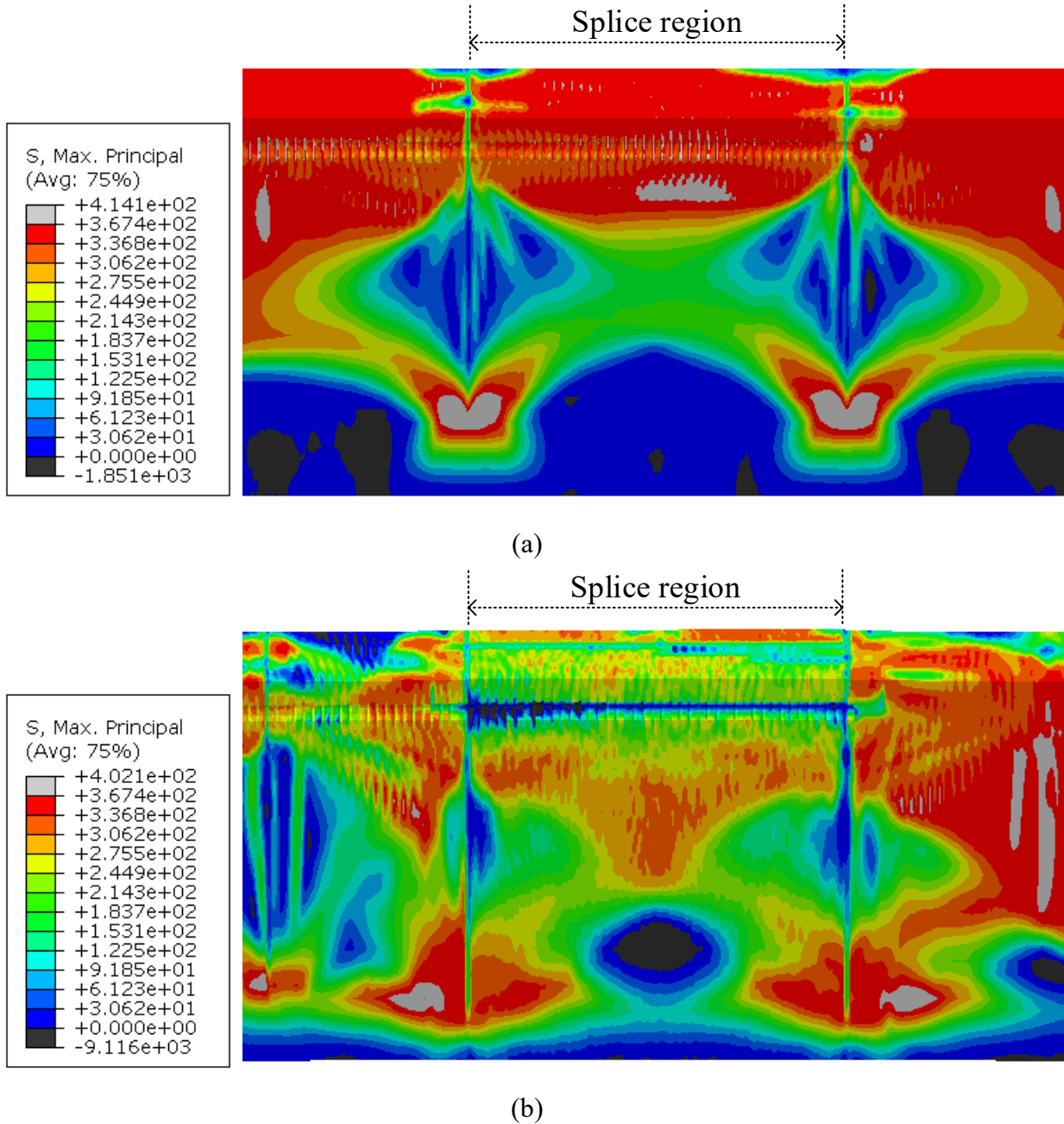
Figure 5.16 A longitudinal section view of maximum principal stress fields of (confined) Specimen I-4 (a) at 17 kip (76 kN) and (b) at the peak load of 30 kip (133 kN)

5.6.2   Epoxy-Coated Bars

The concrete beams containing the epoxy-coated spliced bars (i.e., II-11, II-15, II-12, and II-16) were simulated using the measured and calibrated parameters (Table 5.1 and Table 5.4). The experimental setup, including support conditions and loading protocol, for the specimens

reinforced with typical uncoated bars, were retained on these beams. Specimen dimensions and bar geometries were also the same, as presented in Table 5.1 and Table 5.2. The only changes from the uncoated bar specimens were (1) the yield strength of bars, which was specified in the test program report (Table 5.1) and (2) the tangential friction coefficient at the interface. It is expected that the epoxy coating would render the bar surface smooth enough for the bar to freely slip without inducing significant friction on the interface. Thus, the friction coefficient in the tangential direction on the concrete surface in contact with the bar is expected to be negligible compared to bars with no surface coating and was assumed to be as 0.

Figure 5.17 compares the load versus displacement curves measured for the coated bar specimens with the results of the FE analysis. As was done for uncoated bars case, P_{FEA}/P_{Test} and D_{FEA}/D_{Test} were evaluated and their results are listed in Table 5.6. The models provide a reasonable simulation of responses for unconfined specimens (II-11 and II-12), on average, with simulated strength=107.2% of measured and simulated displacement on the onset of strength loss=79.2% of measured. Simulated strength and displacement are on average, 86.3 and 77.4% of measured for the confined specimens (Specimens II-15 and II-16), respectively. It should also be noted that the coated specimens displayed big differences in load capacities depending on whether they were confined or not. The uncoated cases only showed a small increase in load capacities when they were confined, as shown in Figure 5.12.

In Specimen II-12, some discrepancies in displacements at the peak load are observed between the measured and simulated response. These discrepancies may be due to slight differences in measurement locations. The peak loads in the epoxy-coated and confined specimens, such as Specimens II-15 and II-16, were not well reproduced by the developed FE models. One possibility would be to have an exact representation of the measured rib geometry. Notice that ribs on a bar were modeled as going around the bar circumference and the R_r of 0.1 has been used for all the considered analyses for simplicity. Another FE model having the R_r of 0.091, measured for #9 bar in Specimen II-15, was created to examine its effects on peak load. The simulation result of that model was compared with its counterpart having the R_r of 0.1 in Figure 5.18. It is shown that the model with the measured R_r produced better estimation of peak load. However, the R_r index in representing bar configuration does not describe bar configuration details (e.g., rib angle, rib surface area along the bar axis). In other words, rib configuration can differ even with a fixed R_r, as confirmed in Table 5.5. It is, thus, difficult to conclude that a more complete representation

of the measured R_r is the reason for such differences, given the assumptions/approximations of rib configuration made throughout this study. Nevertheless, it is clear that rib geometries, at least in part, has influence on bond strength, which was also demonstrated for different geometry with a fixed R_r in Figure 5.9. Other possibility would be the inaccurate force transfer at the concrete-steel interface, generated by the general contact model (surface-to-surface contact formulation). This is of concern and to be investigated in a future study.
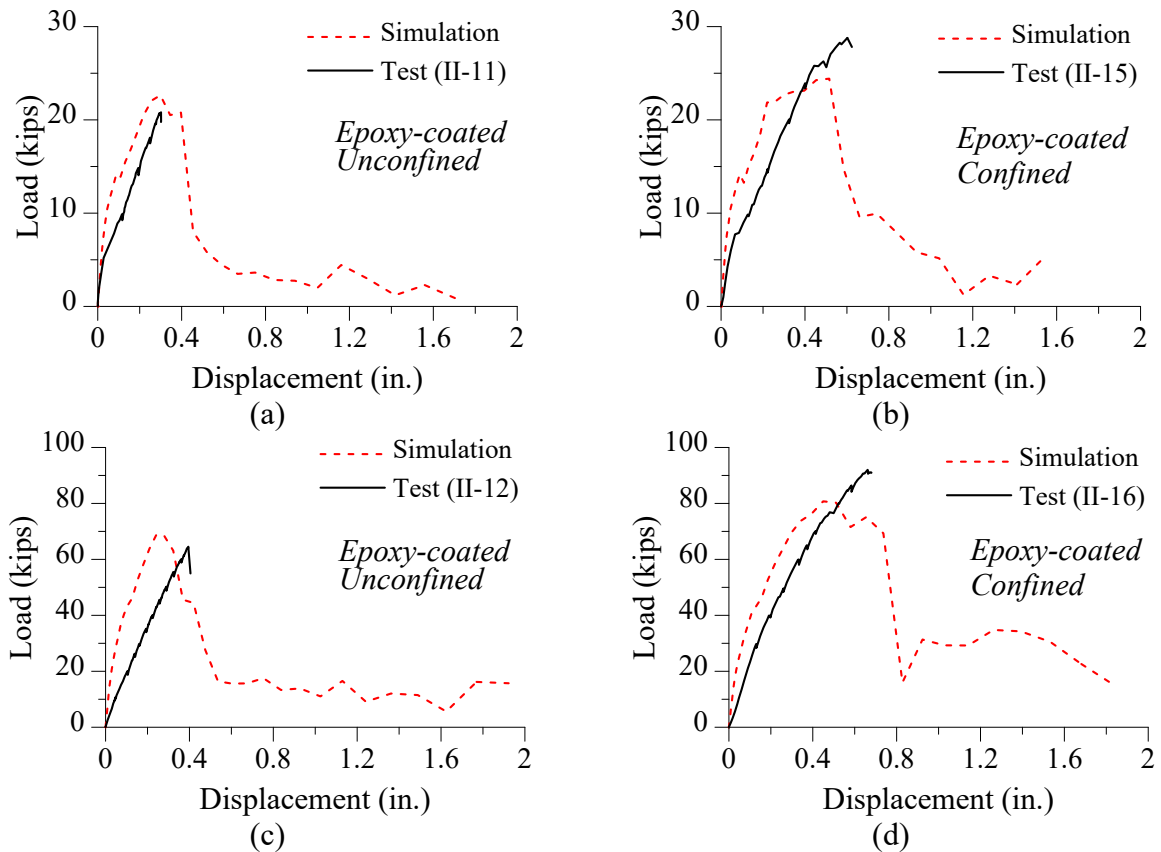

Figure 5.17 Load vs. displacement response simulated and measured in (a) Specimen II-11; (b) Specimen II-15; (c) Specimen II-12; and (d) Specimen II-16
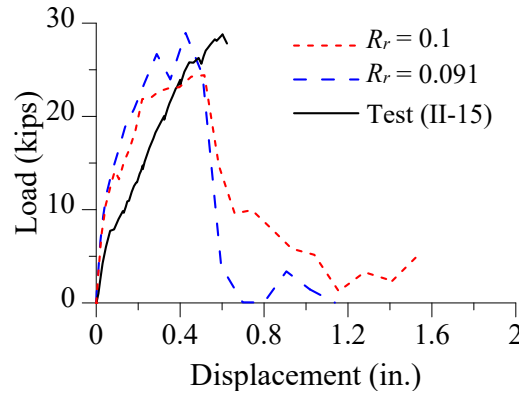
Figure 5.18 Load vs. displacement response of Specimen II-15 for different R_r
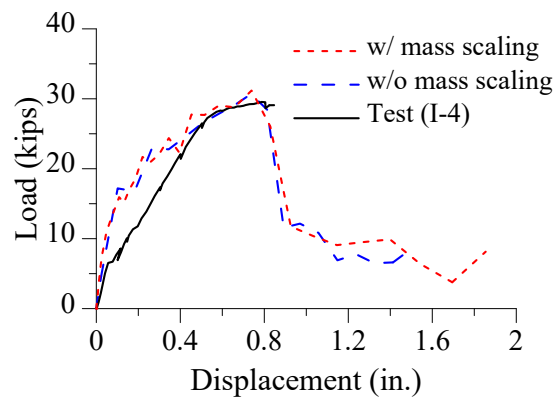
Figure 5.19 Impact of mass scaling on load vs. displacement response of Specimen I-4

5.6.3 Discussion of Computational Demand for Proposed FE Modeling Approach

The proposed modeling approach demands substantial computational power because of the high resolution of mesh elements. Mass scaling provides a solution to speed up the simulation process without sacrificing solution accuracy. With the mass scaling value of 10^{-5}, for instance, the simulation of Specimen I-4 took about 11 h to complete using a Dell PowerEdge R815 server that has 4 x 16 cores with AMD Opteron 62780 processors (2.4 GHz, 8C, Turbo CORE, 8M L2/16M L3) and 512 GB of memory, whereas the same analysis took about a week to be done without mass scaling. As shown in Figure 5.19, the used mass scaling value causes only a minor change in load-displacement simulation while significantly reducing the computation time. As computing technology advances rapidly, it is expected that the time required to complete this type of analysis will be reduced further in the future.

5.6.4   Observations and Conclusions about Proposed FE Modeling Approach

The approach showed its capability of reproducing the bond behavior of spliced deformed bars in high-strength concrete beam structure. The simulations of epoxy-coated bar specimens also showed reasonable agreement with the observed data. The approach distinguished between the unconfined and confined splice bond behavior. Concrete tensile crack patterns were particularly well simulated with this concept. As verified in the case of epoxy-coated bars, the approach is expected to be effective for the simulation of bond composed of new and improved concrete/bar materials, or bars with different surface configuration and toughness.

5.7   Conclusions

This study developed a physics-based rib-scale finite element (FE) model for the numerical simulation of bond-zone behavior of deformed bars in tension splices in high strength RC beams. The numerical FE simulations were conducted using the ABAQUS FE software. In the models, bar ribs were explicitly modeled to account for the bearing of ribs against the adjacent concrete. The general contact model, particularly with the surface-to-surface contact approach formulated, was introduced at the concrete-bar interface for bond effect. In defining the contact model, hard contact, characterizing the normal response at the contact surface, was used to enforce no penetration between bar ribs and the surrounding concrete. Adhesion, i.e., adhesive bonding initiated by chemical action between steel bars and concrete during the curing process, was ignored as experimental and numerical data show that adhesion represents a minimal portion of bond resistance for deformed bars (Abrams, 1913; Lagier et al., 2016; Salem & Maekawa, 2004). Response tangential to the concrete-bar surface was defined via an appropriate friction coefficient. Multiple material parameters such as concrete tensile strength and tangential friction coefficient reported in the literature were calibrated to provide a better prediction of bond behavior in RC beams. The beam splice tests performed by Ramirez & Russell (2008) were chosen to calibrate and validate the models.

The proposed modeling approach captures the difference in the bond behavior of uncoated and epoxy-coated steel bars as well as the impact of transverse reinforcement that acts to confine the splice region. The results of this study support several conclusions and observation about FE analysis of RC bond regions. First, comparison of simulated and measured response histories

shows that the ACI equation defining concrete rupture strength, $7.5\sqrt{f_c}$ psi with f_c in psi (ACI Committee 318, 2014), overestimates concrete tensile capacity for high-strength concrete in modeling bond strength of tension splices, and that defining concrete tensile strength to be $3.0\sqrt{f_c}$ psi with f_c in psi results in a more accurate prediction of strength. The use of the $f_t=3.0\sqrt{f_c}$ psi can be justified by the wide variation in measured concrete tensile strength (fib Bulletin No. 45, 2008; Raphael, 1984) as well as the overestimation of tensile softening behavior in CDP model (Lee & Fenves, 1998). Second, a tangential friction coefficient of μ=0.1 was shown to be appropriate for the uncoated deformed bar, while a value of μ=0 was used for the epoxy-coated bar. It is demonstrated that G_f and G_{fc} for the concrete material have been well defined in the literature: the empirical equation for G_f and measured G_{fc} range work well for predicting the experimental results. In the CDP model, the ψ of 31° and K_c of 0.75 provide good simulation results comparable to the test data. A series of analyses on the rib configuration indicates the importance of representing the rib configurations as they are in the actual deformed bar.

FE simulation results were compared with measured experimental data for splice test specimens. The global load versus displacement relationships, as well as crack initiation and propagation and failure mechanisms, were well reproduced. The greatest discrepancy between experimental and simulation data was found for specimens with epoxy-coated bars and well-confined splice regions. This discrepancy may be due to approximation in bar geometry. Another reason could be inaccurate force transfer at the concrete-steel interface represented with rib geometry, generated by the surface-to-surface contact formulation. The study on contact formulation has not been investigated in this study.

CHAPTER 6.   CONCLUSIONS

6.1   Introduction

Finite element analysis (FEA) provides opportunities to explore structural behavior of reinforced concrete (RC) structures beyond the limitations of experimental testing. In the past, limitations on computing power led researchers to focus effects on "bar-scale" bond stress-slip relations. Few previous studies sought to advance high-resolution (i.e., "rib-scale") simulation of the bond-zone. This study proposes to advance bond models that represent the entirety of the high-resolution finite element (FE) modeling to simulate bond-zone behavior in reinforced concrete. Furthermore, the impact of the concrete material model and material model parameters is investigated.

6.2   Summary

The ABAQUS software platform was used for FE model creation and analysis. The basic model employed a high-resolution mesh; within the bond-zone, concrete and steel deformed reinforcing bar were modeled using solid elements and surface-to-surface contact model was used to simulate load transfer between concrete and steel. The model was applied to simulate "bond" test specimens, in which steel reinforcement was designed to remain elastic or initial yielding under loading, so an isotropic hardening plasticity material model was used for the steel.

Two different concrete constitutive models, that are concrete damaged-plasticity (CDP) model available in ABAQUS and concrete damage-plasticity model (CDPM2) proposed by Grassl et al. (2013), were investigated for use. The CDP model was selected for investigation, as it is one of the most commonly used concrete models in the literature. The CDPM2 was chosen by the fact that it has shown robust nonlinear material response under multiaxial stress states, which provides advantages over the CDP model. Conclusions regarding these models are resented below.

Contact between concrete and steel was modeled using the surface-to-surface contact model, which requires definitions of the tangential, normal, and cohesive components of contact. Research showed that *hard* contact (infinite stiffness with overclosure of the surfaces), Coulomb friction with a friction coefficient of 0.1 for regular bars and 0.0 for epoxy-coated bars, and no cohesion provided the most accurate simulation of response.

For model development and validation purposes, two types of bond problems are considered: (1) pullout bond test and (2) splice test in beam structure. The FE models are developed differently for each test. The validity of the models is demonstrated by the agreement of simulated and measured responses. It is also proved that the developed models can capture different failure mechanisms for different bond conditions: pullout failure or concrete splitting failure in pullout tests and concrete splitting failure in beam splices tests. Additional findings of the study are summarized in the following sections.

6.3   Significance of Choosing Proper Concrete Material Model

Bond failure in RC structures is a complex phenomenon that exhibits a significant nonlinear response in the concrete material, typically through crushing and cracking. Thus, to accurately simulate bond behavior, the concrete material model must be able to accurately represent nonlinear concrete behavior for a range of stress states and stress histories. For this study, two concrete models were used and compared: the concrete damaged-plasticity (CDP) model and the concrete damage-plasticity model (CDPM2). The main features of these models are summarized as follows:

- The CDP model employs a yield function and non-associative plastic flow function based on the Drucker-Prager hyperbolic function and both of which are constructed to have a linear relationship between the volumetric stress and deviatoric stress. The linear expression in the plastic flow function causes the over dilatancy of the material under high volumetric stress states.

- The CDPM2 employs a yield function and non-associative flow function, and both of which are constructed to have a nonlinear relationship between the volumetric stress and deviatoric stress. Unlike the CDP model, the CDPM2's nonlinear plastic flow function is intended to represent realistic dilatancy levels under high volumetric stress states. The model utilizes the effective (undamaged) stress space to introduce a scalar-valued inelastic strain, which enables a quantitative determination of damage in tension and compression. An adaptive ductility measure is introduced for realistic softening response dependent on current volumetric stress state.

Material tests with these concrete models are performed for uniaxial, biaxial, triaxial compression and uniaxial tension loading scenarios. It is observed that both models worked well for all tests, but that CDP model showed limitations in the triaxial compression test, which is mainly due to the

poor representation of yield surface and plastic flow function. This issue was found to be critical to simulation of bond-zone response, as high triaxial compression stress fields develop in the concrete where load transfer occurs through reinforcement rib's bearing on concrete.

6.4   Finite Element Simulation of Pullout Behavior of Reinforcement-Concrete Bond

Pullout specimens comprising a single steel deformed bar embedded in a concrete cylinder with and without confinement were modeled. For each test specimen, the models employed both the CDP model and CDPM2. Overall, the CDPM2 provided the results in reasonable agreement with the measured test data, whereas the CDP model overestimated bond strength. In all the considered pullout tests, concrete elements around the bond-zone were observed to experience extremely high confinement conditions. Thus, the concrete models' capability to reproduce the nonlinear hardening/softening response when subjected to high volumetric stress states has a significant impact on the results. The proposed modeling approach with the CDPM2 was found to simulate, with acceptable accuracy, bond behavior of pullout tests, including capturing different failure modes (reinforcement pullout failure vs. concrete splitting failure) depending on the presence of the confinement.

6.5   Finite Element Simulation of Reinforcement Splice Failure in Concrete Beam

Reinforcement splice tests in concrete beams subjected to monotonically increasing load were simulated using the proposed modeling approach with the CDP model. The CDPM2 is not used since high volumetric compressive stress states are caused by rib bearing during large sliding motions of reinforcement and given that no such effect is expected in the splice tests. Test specimens constructed using uncoated and epoxy-coated reinforcing bars and with and without confinement were modeled. All test specimens failed by concrete splitting in the splice region of the beams. For the analyses, it was found that use of a concrete tensile strength of $3.0\sqrt{f_c}$ resulted in accurate simulation of specimen strength. This reduced tensile strength is consistent with the observed range of concrete tensile strength (fib Bulletin No. 45, 2008; Raphael, 1984). It was observed that the model can distinguish between the behavior of uncoated and epoxy-coated rebars as well as simulate the impact of confinement on bond strength.

6.6   Limitations, Potentials, and Future Research

Despite successful validation, some limitations were found in the proposed modeling approach. First, in pullout tests, when spiral reinforcement is modeled with truss elements and *perfect* bond between truss-element confining steel and solid-element concrete is assumed (via use of the ABAQUS *embedded element* command), simulated confining pressure is greater than expected. To resolve this issue, a more realistic constraint between concrete solid elements and rebar truss elements, which can limit the bond stress and let the rebar slip (e.g., bond stress-slip model), is required. Additionally, convergence issues were encountered when using the CDPM2 concrete model; these issues were observed mainly when the concrete elements were severely damaged due to high volumetric compressive stress states. Specifically, a general return-mapping algorithm for plasticity was used to update the stress, hardening variable (or cumulative plastic strain), and plastic multiplier within each material point, where all these variables were iteratively updated until they satisfied the prescribed criteria using an iterative Newton's method. The numerical issue occurred when the Jacobian matrix became singular due to either the infinite or zero value of the matrix component(s). To resolve this issue, further study is required to develop a stable numerical method for updating the stress.

Rib-scale modeling of bond-zone requires large computational resources. Nevertheless, the power of this modeling approach is that it predicts bond failure and damage patterns entirely on the basis of the physical and material properties of the bond area. The successful implementation of the proposed approach is expected to be effective for the development of new design specifications for bond in reinforced concrete with new and improved materials, or for bars with different surface configuration or roughness.

REFERENCES

Abrams, D. A. (1913). Tests of bond between concrete and steel. *Bulletin No. 71 University of Illinois Bulletin XI (15)*.

ACI 318 Committee. (2014). *An ACI Standard and Report: Building Code Requirements for Structural Concrete (ACI 318-14)*. 524.

Ansari, F., & Li, Q. (1998). High-Strength Concrete Subjected to Triaxial Compression. *Materials Journal*, *95*(6), 747–755. https://doi.org/10.14359/420

Attard, M. M., & Setunge, S. (1996). Stress-Strain Relationship of Confined and Unconfined Concrete. *Materials Journal*, *93*(5). https://doi.org/10.14359/9847

Azizinamini, A., Stark, M., Roller, J. J., & Ghosh, S. K. (1993). Bond Performance of Reinforcing Bars Embedded in High-Strength Concrete. *Structural Journal*, *90*(5). https://doi.org/10.14359/3951

Balmer, G. G. (1949). Shearing strength of concrete under high triaxial stress-computation of Mohr's envelope as a curve. *Structural Research Laboratory Report, United States Department of the Interior, Bureau of Reclamation*, No-SP.

Bažant, Z. P., & Becq-Giraudon, E. (2002). Statistical prediction of fracture parameters of concrete and implications for choice of testing standard. *Cement and Concrete Research*, *32*(4), 529–556. https://doi.org/10.1016/S0008-8846(01)00723-2

Berry, M. P., Lehman, D. E., & Lowes, L. N. (2008). Lumped-Plasticity Models for Performance Simulation of Bridge Columns. *ACI Structural Journal*, *105*(3), 270-279,38-39. Retrieved from Research Library; Technology Collection. (198347658)

Brown, C. J., Darwin, D., & McCabe, S. L. (1993). *Finite element fracture analysis of steel-concrete bond*. University of Kansas Center for Research, Inc.

Candappa, D. C., Sanjayan, J. G., & Setunge, S. (2001). Complete Triaxial Stress-Strain Curves of High-Strength Concrete. *Journal of Materials in Civil Engineering*, *13*(3), 209–215. https://doi.org/10.1061/(ASCE)0899-1561(2001)13:3(209)

Chen, G. M., Teng, J. G., & Chen, J. F. (2011). Finite-Element Modeling of Intermediate Crack Debonding in FRP-Plated RC Beams. *Journal of Composites for Construction*, *15*(3), 339–353. https://doi.org/10.1061/(ASCE)CC.1943-5614.0000157

Chinn, J., & Zimmerman, R. M. (1965). *BEHAVIOR OF PLAIN CONCRETE UNDER VARIOUS HIGH TRIAXIAL COMPRESSION LOADING CONDITIONS.* COLORADO UNIV AT BOULDER.

Coleman, J., & Spacone, E. (2001). Localization Issues in Force-Based Frame Elements. *Journal of Structural Engineering*, *127*(11), 1257–1265. https://doi.org/10.1061/(ASCE)0733-9445(2001)127:11(1257)

Cox, J. V., & Herrmann, L. R. (1998). Development of a plasticity bond model for steel reinforcement. *Mechanics of Cohesive-frictional Materials*, *3*(2), 155–180.

Darwin, D., & Graham, E. K. (1993). *Effect of deformation height and spacing on bond strength of reinforcing bars*. University of Kansas Center for Research, Inc.

Eligehausen, R., Popov, E. P., & Bertero, V. V. (1983). *Local bond stress-slip relationships of deformed bars under generalized excitations* (p. 169). Earthquake Engineering Research Center, University of California, Berkeley.

Erfanian, A., & Alaa, E. E. (2019). Bond Plastic Model for Steel–Concrete Damaged Interface Element. *Journal of Structural Engineering*, *145*(5), 04019018. https://doi.org/10.1061/(ASCE)ST.1943-541X.0002302

Feng, Y., Kowalsky, M. J., & Nau, J. M. (2015). Finite-Element Method to Predict Reinforcing Bar Buckling in RC Structures. *Journal of Structural Engineering*, *141*(5). https://doi.org/10.1061/(ASCE)ST.1943-541X.0001048

fib Bulletin No. 45. (2008). *Practitioners' Guide to Finite Element Modelling of Reinforced Concrete Structures*.

Genikomsou, A. S., & Polak, M. A. (2015). Finite element analysis of punching shear of concrete slabs using damaged plasticity model in ABAQUS. *Engineering Structures*, *98*, 38–48. https://doi.org/10.1016/j.engstruct.2015.04.016

Gopalaratnam, V. S., & Shah, S. P. (1985). Softening Response of Plain Concrete in Direct Tension. *Journal Proceedings*, *82*(3). https://doi.org/10.14359/10338

Goto, Y. (1971). Cracks Formed in Concrete Around Deformed Tension Bars. *Journal Proceedings*, *68*(4). https://doi.org/10.14359/11325

Grassl, P. (2008). On a damage-plasticity approach to model concrete failure. *ArXiv Preprint ArXiv:0811.2776*.

Grassl, P., & Jirásek, M. (2006). Damage-plastic model for concrete failure. *International Journal of Solids and Structures*, *43*(22), 7166–7196. https://doi.org/10.1016/j.ijsolstr.2006.06.032

Grassl, P., Xenos, D., Nyström, U., Rempling, R., & Gylltoft, K. (2013). CDPM2: A damage-plasticity approach to modelling the failure of concrete. *International Journal of Solids and Structures*, *50*(24), 3805–3816. https://doi.org/10.1016/j.ijsolstr.2013.07.008

Hawileh, R. A., Naser, M., Zaidan, W., & Rasheed, H. A. (2009). Modeling of insulated CFRP-strengthened reinforced concrete T-beam exposed to fire. *Engineering Structures*, *31*(12), 3072–3079. https://doi.org/10.1016/j.engstruct.2009.08.008

Hoehler, M. S., & Stanton, J. F. (2006). Simple phenomenological model for reinforcing steel under arbitrary load. *Journal of Structural Engineering*, *132*(7), 1061–1069.

Huang, Y., Yang, Z., Ren, W., Liu, G., & Zhang, C. (2015). 3D meso-scale fracture modelling and validation of concrete based on in-situ X-ray Computed Tomography images using damage plasticity model. *International Journal of Solids and Structures*, *67–68*, 340–352. https://doi.org/10.1016/j.ijsolstr.2015.05.002

Hwang, S.-H., & Lignos, D. G. (2017). Earthquake-induced loss assessment of steel frame buildings with special moment frames designed in highly seismic regions. *Earthquake Engineering & Structural Dynamics*, *46*(13), 2141–2162. https://doi.org/10.1002/eqe.2898

Idun, E. K., & Darwin, D. (1999). Bond of Epoxy-Coated Reinforcement: Coefficient of Friction and Rib Face Angle. *Structural Journal*, *96*(4). https://doi.org/10.14359/698

Imran, I., & Pantazopoulou, S. J. (1996). Experimental Study of Plain Concrete under Triaxial Stress. *Materials Journal*, *93*(6). https://doi.org/10.14359/9865

Imran, Iswandi. (1996). *Applications of non-associated plasticity in modelling the mechanical response of concrete.*

Jansen, D. C., & Shah, S. P. (1997). Effect of Length on Compressive Strain Softening of Concrete. *Journal of Engineering Mechanics*, *123*(1), 25–35. https://doi.org/10.1061/(ASCE)0733-9399(1997)123:1(25)

Jason, L., Huerta, A., Pijaudier-Cabot, G., & Ghavamian, S. (2006). An elastic plastic damage formulation for concrete: Application to elementary tests and comparison with an isotropic damage model. *Computer Methods in Applied Mechanics and Engineering*, *195*(52), 7077–7092. https://doi.org/10.1016/j.cma.2005.04.017

Jirásek, M., & Zimmermann, T. (1998). Rotating Crack Model with Transition to Scalar Damage. *Journal of Engineering Mechanics*, *124*(3), 277–284. https://doi.org/10.1061/(ASCE)0733-9399(1998)124:3(277)

Ju, J. W. (1989). On energy-based coupled elastoplastic damage theories: Constitutive modeling and computational aspects. *International Journal of Solids and Structures*, *25*(7), 803–833. https://doi.org/10.1016/0020-7683(89)90015-2

Kotsovos, M. D., & Newman, J. B. (1980). Mathematical Description of Deformational Behavior of Concrete Under Generalized Stress Beyond Ultimate Strength. *Journal Proceedings*, *77*(5). https://doi.org/10.14359/7012

Kupfer, H., Hilsdorf, H. K., & Rusch, H. (1969). Behavior of Concrete Under Biaxial Stresses. *Journal Proceedings*, *66*(8). https://doi.org/10.14359/7388

Lagier, F., Massicotte, B., & Charron, J. (2016). 3D Nonlinear Finite-Element Modeling of Lap Splices in UHPFRC. *Journal of Structural Engineering*, 04016087. https://doi.org/10.1061/(ASCE)ST.1943-541X.0001549

Lan, S., & Guo, Z. (1999). Biaxial Compression Behavior of Concrete under Repeated Loading. *Journal of Materials in Civil Engineering*, *11*(2), 105–115. https://doi.org/10.1061/(ASCE)0899-1561(1999)11:2(105)

Lee, J., & Fenves, G. L. (1998). Plastic-damage model for cyclic loading of concrete structures. *Journal of Engineering Mechanics*, *124*(8), 892–900.

Li, J. (2010). *An investigation of behavior and modeling of bond for reinforced concrete*. University of Washington.

Lim, Jian C., Ozbakkaloglu, T., Gholampour, A., Bennett, T., & Sadeghi, R. (2016). Finite-Element Modeling of Actively Confined Normal-Strength and High-Strength Concrete under Uniaxial, Biaxial, and Triaxial Compression. *Journal of Structural Engineering*, *142*(11), 04016113. https://doi.org/10.1061/(ASCE)ST.1943-541X.0001589

Lim, Jian Chin, & Ozbakkaloglu, T. (2014). Comparison of Stress-Strain Relationships of FRP and Actively Confined High-Strength Concrete: Experimental Observations. *Advanced Materials Research*, *919–921*, 29–34. https://doi.org/10.4028/www.scientific.net/AMR.919-921.29

Lowes, L. N., Moehle, J. P., & Govindjee, S. (2004). Concrete-Steel Bond Model for Use in Finite Element Modeling of Reinforced Concrete Structures. *Structural Journal*, *101*(4). https://doi.org/10.14359/13336

Lubliner, J., Oliver, J., Oller, S., & Oñate, E. (1989). A plastic-damage model for concrete. *International Journal of Solids and Structures*, *25*(3), 299–326. https://doi.org/10.1016/0020-7683(89)90050-4

Lundgren, K. (2000). Pull-out tests of steel-encased specimens subjected to reversed cyclic loading. *Materials and Structures*, *33*(7), 450–456.

Lutz, L. A., & Gergely, P. (1967). Mechanics of Bond and Slip of Deformed Bars in Concrete. *Journal Proceedings*, *64*(11). https://doi.org/10.14359/7600

Marques, J. L. G., & Jirsa, J. O. (1975). A Study of Hooked Bar Anchorages in Beam-Column Joints. *Journal Proceedings*, *72*(5). https://doi.org/10.14359/11131

Martin, J., Stanton, J., Mitra, N., & Lowes, L. N. (2007). Experimental testing to determine concrete fracture energy using simple laboratory test setup. *ACI Materials Journal*, *104*(6), 575–584.

Menetrey, Ph., & Willam, K. J. (1995). Triaxial Failure Criterion for Concrete and its Generalization. *Structural Journal*, *92*(3). https://doi.org/10.14359/1132

Metelli, G., & Plizzari, G. A. (2014). Influence of the relative rib area on bond behaviour. *Magazine of Concrete Research*, *66*(6), 277–294.

Michou, A., Hilaire, A., Benboudjema, F., Nahas, G., Wyniecki, P., & Berthaud, Y. (2015). Reinforcement–concrete bond behavior: Experimentation in drying conditions and meso-scale modeling. *Engineering Structures*, *101*, 570–582. https://doi.org/10.1016/j.engstruct.2015.07.028

Mills, L. L., & Zimmerman, R. M. (1970). Compressive Strength of Plain Concrete Under Multiaxial Loading Conditions. *Journal Proceedings*, *67*(10). https://doi.org/10.14359/7310

Minor, J., & Jirsa, J. O. (1975). *Behavior of bent bar anchorages*. *72*. ACI.

Murcia-Delso, J., & Shing, P. B. (2014). Bond-Slip Model for Detailed Finite-Element Analysis of Reinforced Concrete Structures. *Journal of Structural Engineering*, *141*(4), 04014125 (10 pp.). https://doi.org/10.1061/(ASCE)ST.1943-541X.0001070

Murcia-Delso, J., & Shing, P. B. (2015). Elastoplastic Dilatant Interface Model for Cyclic Bond-Slip Behavior of Reinforcing Bars. *Journal of Engineering Mechanics*, 04015082. https://doi.org/10.1061/(ASCE)EM.1943-7889.0000994

Murcia-Delso, J., Stavridis, A., & Shing, P. B. (2013). Bond Strength and Cyclic Bond Deterioration of Large- Diameter Bars. *ACI Structural Journal*, *110*(4), 659–669. Retrieved from ProQuest Research Library; ProQuest Technology Collection. (1372765917)

Nana, W. S. A., Bui, T. T., Limam, A., & Abouri, S. (2017). Experimental and Numerical Modelling of Shear Behaviour of Full-scale RC Slabs Under Concentrated Loads. *Structures*, *10*, 96–116. https://doi.org/10.1016/j.istruc.2017.02.004

Nguyen, G. D., & Houlsby, G. T. (2008). A coupled damage–plasticity model for concrete based on thermodynamic principles: Part I: model formulation and parameter identification. *International Journal for Numerical and Analytical Methods in Geomechanics*, *32*(4), 353–389. https://doi.org/10.1002/nag.627

Nguyen, G. D., & Korsunsky, A. M. (2008). Development of an approach to constitutive modelling of concrete: Isotropic damage coupled with plasticity. *International Journal of Solids and Structures*, *45*(20), 5483–5501. https://doi.org/10.1016/j.ijsolstr.2008.05.029

Poliotti, M., & Bairán, J.-M. (2019). A new concrete plastic-damage model with an evolutive dilatancy parameter. *Engineering Structures*, *189*, 541–549. https://doi.org/10.1016/j.engstruct.2019.03.086

Ramirez, J. A., & Russell, B. W. (2008). *Transfer, development, and splice length for strand/reinforcement in high-strength concrete* (Vol. 603). Transportation Research Board.

Raphael, J. M. (1984). Tensile Strength of Concrete. *Journal Proceedings*, *81*(2). https://doi.org/10.14359/10653

Raynor, D. J., Lehman, D. E., & Stanton, J. F. (2002). Bond-slip response of reinforcing bars grouted in ducts. *Structural Journal*, *99*(5), 568–576.

Richart, F. E., Brandtzaeg, A., & Brown, R. L. (1928). *A study of the failure of concrete under combined compressive stresses*. University of Illinois at Urbana Champaign, College of Engineering ….

Salem, H., & Maekawa, K. (2004). Pre- and Postyield Finite Element Method Simulation of Bond of Ribbed Reinforcing Bars. *Journal of Structural Engineering*, *130*(4), 671–680. https://doi.org/10.1061/(ASCE)0733-9445(2004)130:4(671)

Schickert, G., & Winkler, H. (1977). *Results of test concerning strength and strain of concrete subjected to multi-axial compressive stress*.

Seok, S. (2019). seungwookseok/ABAQUS-version-CDPM2: First release of ABAQUS-CDPM2 (Version v1.0.0). https://doi.org/10.5281/zenodo.3368644

Seok, S., Haikal, G., Ramirez, J. A., & Lowes, L. N. (2018). High-resolution finite element modeling for bond in high-strength concrete beam. *Engineering Structures*, *173*, 918–932. https://doi.org/10.1016/j.engstruct.2018.06.068

Sfer, D., Carol, I., Gettu, R., & Etse, G. (2002). Study of the Behavior of Concrete under Triaxial Compression. *Journal of Engineering Mechanics*, *128*(2), 156–163. https://doi.org/10.1061/(ASCE)0733-9399(2002)128:2(156)

Simulia, D. (2014). ABAQUS 6.14 analysis user's manual. *Abaqus*, *6*.

Smith, S. S., Willam, K. J., Gerstle, K. H., & Sture, S. (1989). Concrete Over the Top, or: Is there Life After Peak? *Materials Journal*, *86*(5). https://doi.org/10.14359/2089

Sperry, J., Al-Yasso, S., Searle, N., DeRubeis, M., Darwin, D., O'Reilly, M., … Lequesne, R. (2015). *ANCHORAGE OF HIGH-STRENGTH REINFORCING BARS WITH STANDARD HOOKS*.

Tai, Y.-S., El-Tawil, S., & Chung, T.-H. (2016). Performance of deformed steel fibers embedded in ultra-high performance concrete subjected to various pullout rates. *Cement and Concrete Research*, *89*, 1–13.

Tholen, M. L., & Darwin, D. (1996). *Effects of deformation properties on the bond of reinforcing bars*. University of Kansas Center for Research, Inc.

Valentini, B., & Hofstetter, G. (2013). Review and enhancement of 3D concrete models for large-scale numerical simulations of concrete structures. *International Journal for Numerical and Analytical Methods in Geomechanics*, *37*(3), 221–246. https://doi.org/10.1002/nag.1096

Voyiadjis, G. Z., Taqieddin, Z. N., & Kattan, P. I. (2008). Anisotropic damage–plasticity model for concrete. *International Journal of Plasticity*, *24*(10), 1946–1965. https://doi.org/10.1016/j.ijplas.2008.04.002

Wille, K., & Naaman, A. E. (2013). Effect of Ultra-High-Performance Concrete on Pullout Behavior of High-Strength Brass-Coated Straight Steel Fibers. *Materials Journal*, *110*(4). https://doi.org/10.14359/51685792

Wriggers, P., & Zavarise, G. (2004). *Computational contact mechanics*.

Xie, J., Elwi, A. E., & MacGregor, J. G. (1995). Mechanical Properties of Three High-Strength Concretes Containing Silica Fume. *Materials Journal*, *92*(2). https://doi.org/10.14359/9764

Yang, K.-H., Mun, J.-H., Cho, M.-S., & Kang, T. H. (2014). Stress-Strain Model for Various Unconfined Concretes in Compression. *Structural Journal*, *111*(4). https://doi.org/10.14359/51686631

Yoo, D.-Y., & Yoon, Y.-S. (2015). Structural performance of ultra-high-performance concrete beams with different steel fibers. *Engineering Structures*, *102*, 409–423.

Yu, T., Teng, J. G., Wong, Y. L., & Dong, S. L. (2010). Finite element modeling of confined concrete-II: Plastic-damage model. *Engineering Structures*, *32*(3), 680–691. https://doi.org/10.1016/j.engstruct.2009.11.013

Zuo, J., & Darwin, D. (1998). *Bond strength of high relative rib area reinforcing bars*. University of Kansas Center for Research, Inc.

Zuo, J., & Darwin, D. (2000). Splice strength of conventional and high relative rib area bars in normal and high-strength concrete. *ACI Structural Journal*, *97*(4), 630–641.